Title
CHARGED HADRON PRODUCTION IN e+e-COLLISIONS AT PEP WITH THE TPC

Author
Hadley, N.J.

Publication Date
1983-05-01

LBL-16116

Lawrence Berkeley Laboratory
UNIVERSITY OF CALIFORNIA

Physics, Computer Science & Mathematics Division

CHARGED HADRON PRODUCTION IN e^+e^- COLLISIONS AT PEP WITH THE TPC

N.J. Hadley
(Ph.D. Thesis)

May 1983

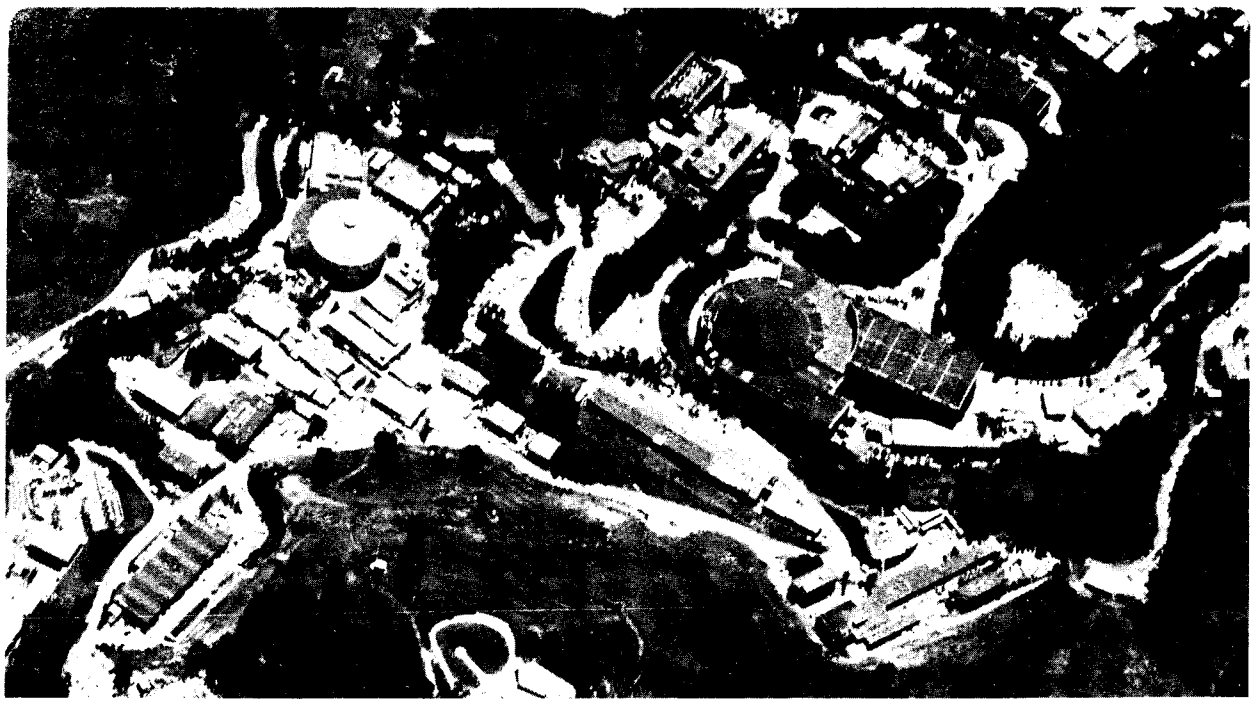

Prepared for the U.S. Department of Energy under Contract DE-AC03-76SF00098

DISCLAIMER

LBL-16116

CHARGED HADRON PRODUCTION IN e^+e^- COLLISIONS AT PEP WITH THE TPC

By

Nicholas John Hadley

(Ph.D. Thesis)

Lawrence Berkeley Laboratory
University of California
Berkeley, California 94720

May 13, 1983

This work was supported by the Director, Office of Energy Research, Office of High Energy and Nuclear Physics Division of High Energy Physics of the U.S. Department of Energy under Contract No. DE-AC03-76SF00098.

Charged Hadron Production in e^+e^- Collisions at PEP with the TPC

Nicholas John Hadley

ABSTRACT

We have studied hadron production in e^+e^- annihilation at 29 GeV center of mass energy. We have measured the particle fractions and particle separated differential cross sections using the PEP-4 (Time Projection Chamber) detector. The particles were identified by measuring their ionization energy loss (dE/dx). The pion fraction decreases from above 90% at 400 MeV/c to 55% at 6 GeV/c. Our results for kaon production require that a large number of kaons are produced by strange quarks pulled from the vacuum.

We have also measured R, the ratio of the total hadronic cross section to the mu pair cross section. Our value for R is 3.7 with an uncertainty of 10%. This value is in agreement with the results of other experiments and with the predictions of the quark-parton model.

Acknowledgements

The PEP-4 Time Projection Chamber was the result of hard work by more than 100 people. It is a pleasure to acknowledge all the effort from so many in designing, building, and operating the detector. Thanks are also due to the personnel from SLAC and LBL who built and operated the PEP accelerator.

I would like to thank my advisor, David Nygren, for providing the ideas and inspiration that led to the Time Projection Chamber.

Much of the work described in this dissertation was done in collaboration with Werner Hofmann, who generously shared both his knowledge of physics and his clear thinking. His effort and advice saved much time and improved this dissertation considerably. I would also like to thank Gerry Lynch for instructing me in the art of data analysis and sharing with me his skill in understanding the detector through the data.

I am glad to acknowledge the efforts, advice, and long hours shared with Richard Kofler, Bernard Gabioud, Marjorie Shapiro, Forest Rouse, Bill Gary, and Jon Bakken in working on the TPC electronics and on the data from the experiment.

My knowledge of experimental hardware comes from working with Ray Fuzesy and Peter Robrish. Peter's determination saw the design and construction of the TPC endcap wire chambers (sectors) through many crises. Ray's insight and ideas made the sectors possible, and

his organizational skills ensured that they were built. It was a pleasure to work with him and learn from him.

I would like to thank David Nygren, Lynn Stevenson, Gilbert Shapiro, and Ian Carmichael for reading this dissertation and commenting on it. Lynn Stevenson also served as my faculty contact, providing advice and encouragement, while preserving me from many bureaucratic difficulties.

I am grateful to Bob Koda for his analysis of the Bhabha events used for the luminosity determination in chapter 5. Finally, I would like to thank Ed Whipple for setting up procedures so that the type setting system used in producing this dissertation would run smoothly.

Contents

Chapter 1

Introduction

The study of hadron production by e^+e^- annihilation during the past decade has provided much experimental evidence for the validity of the quark-parton model. The recent observation of three-jet events [Barber 79, Bartel 79, Berger 79, Brandelik 79] has confirmed an important prediction of the quantum chromodynamic (QCD) theory of strong interactions, and provided evidence for the existence of additional partons, gluons, which are massless vector bosons that mediate the strong force. The partons, the quarks and gluons, are not observed directly, however. Experimentally, what is detected are the particles that are produced from the primary partons. In this dissertation we will describe the charged composition of the final state in e^+e^- annihilation at a center of mass energy of 29 GeV and use the measurements to study the process by which the quarks and gluons are transformed into hadrons.

We will begin with a discussion of the phenomenology of hadron production in e^+e^- annihilation, concentrating on those results which have led to the current theoretical models of e^+e^- interactions. This will be followed by a description of the PEP accelerator and the PEP-4 (Time Projection Chamber or TPC) detector, emphasizing the particle identification capabilities of the TPC. Next, measurements of the total hadronic cross section, the total charged multiplicity, and event topology will be presented. The results are in agreement with

theoretical predictions from the quark-parton model and QCD and provide a general framework for understanding e^+e^- annihilations into hadrons.

We will then discuss the charged hadron composition of the events. Data on the relative fractions of pions, kaons, and protons will be presented, along with the differential cross sections for the different particle types. These data will be compared with theoretical predictions based on the quark-parton model and QCD. The fraction of kaons will be shown to be too large to be accounted for by either direct strange quark production or by decays of bottom and charm quarks. The relative probability of producing strange or up quarks from the vacuum will be determined within the context of the LUND model [Andersson 78] .

Chapter 2

Hadron Production Phenomenology

In order to provide the appropriate background for a discussion of our measurements of the total hadronic cross section and the charged hadron composition of the events, we will briefly review the experimental results on hadron production in e^+e^- annihilation over the last decade, starting from the discovery of the J/ψ meson in 1974 [Aubert 74, Augustin 74]. We will discuss the dramatic successes of the quark-parton model in describing the J/ψ families of resonances and in predicting R, the ratio of the total hadronic cross section to the mu pair cross section. We will review the observation of two-jet events in which hadrons are produced in two back-to-back cones and the later observation at higher energies of three-jet events, as predicted by the quantrum chromodynamic (QCD) theory of the strong interaction. We will then discuss models of hadronization, the process by which quarks dress themselves into the observed hadrons.

There are two main advantages in producing hadrons in e^+e^- annihilations at colliding beam accelerators. First, in colliding beam machines, the energy available for producing particles increases linearly with the electron and positron energies. In fixed target machines, however, the energy available for producing particles increases only as the square root of the energy of the incident particle. Second, the initial state in e^+e^- annihilations is relatively simple. We consider here only those reactions that take place through one photon (or Z^0) exchange (see Fig. 2.1). For such events, the initial state amplitude, either for $e^+e^- \rightarrow \gamma^*$ or $e^+e^- \rightarrow Z^0$, can be calculated

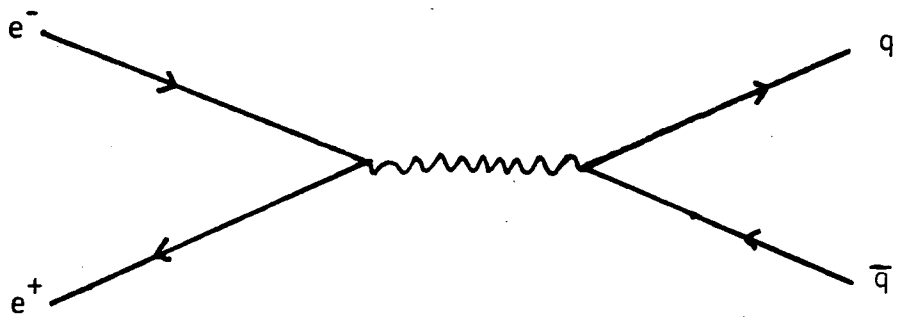

Figure 2.1. $e^+e^- \to q\bar{q}$ by one photon (or Z^0) exchange

to sufficient accuracy using quantum electrodynamics (QED) and the standard Weinberg-Salam model [Weinberg 67, Salam 68] or many other models of the weak interaction. In the energy range we will consider weak interaction effects, which are due to the coupling of the electron and positron to the Z^0, are small (<10%) and may be largely neglected. (The interference between the weak and electromagnetic amplitudes is observable, however, in such effects as the forward-backward asymmetry in $e^+e^- \rightarrow \mu^+\mu^-$. The results of measurements of these asymmetries are in good agreement with calculations based on the Weinberg-Salam theory. For a review of weak-electromagnetic interference effects in e^+e^- experiments, see Boehm 82.)

High energy hadron production in e^+e^- annihilation is usually described in terms of the quark-parton model in which the electron and positron annihilate into a single virtual photon which then produces a quark-antiquark pair. In the standard model, quarks are point particles having charges $+\frac{2}{3}$ and $-\frac{1}{3}$ and baryon number $\frac{1}{3}$. The only observed particles are mesons , which are quark-antiquark ($q\bar{q}$) bound states, and baryons , which are 3 quark (qqq) bound states.

The properties of the J/ψ family of resonances at 3 GeV and the Υ family of resonances at 10 GeV provide striking confirmation of the quark model with the states assumed to be composed of a charm-anticharm quark-antiquark pair ($c\bar{c}$) and a bottom-antibottom quark-antiquark pair ($b\bar{b}$) respectively. Using a simple non-relativistic potential model, the electronic widths and level spacings, as well as the spins and parities of many states, can be calculated quite accurately with relatively few input assumptions.(For a review of quarkonium models, see, for example, Appelquist 78). Charmed mesons, those composed of one charm quark and one light quark, were discovered in 1976 [Goldhaber 76]. Their decay modes and lifetimes are consistent with those required by standard weak interaction theory. Recently, evidence has been found for a state composed of one bottom quark and one light quark [Behrends 82].

There are now five known quarks. They have been named up, down, strange, charm, and bottom. The up and down quarks are light and make up the most common and longest lived

hadrons, protons, neutrons, and pions. The five quarks are sufficient to account for all known hadrons. Each quark also possesses an additional quantum number known as color. Color is necessary to make the theoretical and experimental values of the π^0 lifetime agree and to satisfy Pauli statistics in the Δ^{++} state which is composed of three up quarks, all in s states.

Color is also necessary to account for the value of R, the ratio of the hadronic cross section to the mu pair cross section in e^+e^- annihilation.

The calculation of the cross section for the process $e^+e^- \rightarrow q\bar{q}$ is the same as that for $e^+e^- \rightarrow \mu^+\mu^-$ except that the quark charge replaces the muon charge in all formulas. Thus,

$$R = \frac{\sigma(e^+e^- \rightarrow \text{hadrons})}{\sigma(e^+e^- \rightarrow \mu^+\mu^-)} = \sum_{i=1}^{N} e_{q_i}^2 \times (\text{number of colors}). \qquad (2.1)$$

The sum in equation 2.1 is over all quarks that can be produced given the available energy. A compilation of values for R from different experiments as a function of center of mass energy (E_{cm}) is given in figure 2.2. (In e^+e^- annihilation, $E_{cm} = \sqrt{s}$). The spikes in the value of R occur at the vector mesons, ρ, ϕ, ω, J/ψ,... , due to the resonant formation of quark-antiquark states. The step in the value of R above the J/ψ meson is due to the contribution of the charm quark. We note that R is well described by a constant above 12 GeV, as expected from the theory since no new quarks contribute. Assuming three colors and the standard quark charges, equation 2.1 predicts R = $\frac{11}{3}$ in good agreement with the data.

In the quark-parton model hadron production at high energies in e^+e^- annihilation proceeds through the creation of a rapidly moving quark-antiquark pair, each of which then fragments into hadrons. It then seems natural to predict the existence of jets, to predict that hadrons will be produced in two back-to-back cones with each hadron having only limited transverse momentum with respect to the jet axis, which should be closely aligned with the direction of the original quark or antiquark. Such two-jet events were first observed at SPEAR at 7 GeV [Hanson 75]. At higher energies like those at PEP, about 30 GeV, such events dominate

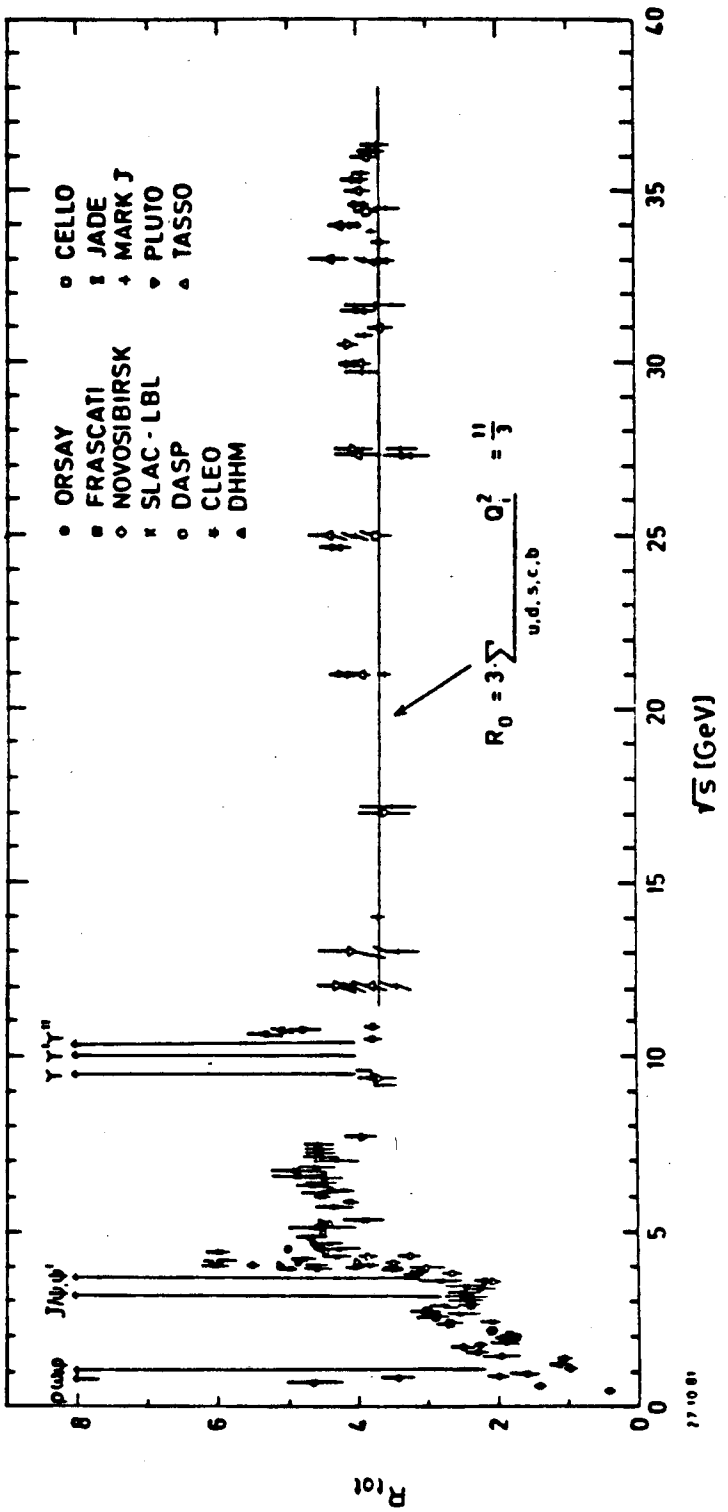

Figure 2.2. R as a Function of $\sqrt{s}$ from Felst 81

the hadronic events and are a striking feature of the data (see Fig. 2.3). Studies of the orientation of the jet axes show a $1+\cos^2\theta$ angular distribution, confirming that quarks are spin $\frac{1}{2}$ particles.

However, some events display a three-jet structure, and the jet cones, on the average, are not as collimated as a simple extrapolation from lower energies would have predicted. Three-jet events were first observed by all 4 detectors at PETRA in 1979 [Barber 79, Bartel 80, Berger 79, Brandelik 79].

They were predicted [Polyakov 75, Ellis 76] by theorists using quantum chromodynamics (QCD), a theory of the strong force . In QCD, the interaction between quarks is mediated by gluons, much as the interaction among electrically charged particles is mediated by photons in QED. The gluons couple to the color charge of the quarks and are massless vector particles of odd parity forming a color octet. Unlike in QED where the photon is electrically neutral, gluons are colored. They are described by two color indices and interact among themselves via three gluon and four gluon vertices . Furthermore, in QCD the coupling constant, α_s, which is analogous to α in QED, varies logarithmically with energy.

$$\alpha_s = \frac{12\pi}{33 - 2f\ln(q^2/\Lambda^2)}, \tag{2.2}$$

where f is the number of quark flavors, q^2 the energy transfer, and Λ a scale parameter.

From the formula, we see that as the energy transfer increases, α_s decreases. Thus, at very high energies or short distances, quarks act as nearly free objects. At low energies or short distances, α_s is large and the quark-quark force is strong. It is hoped that this strong force will eventually be shown to lead to quark confinement, since no free quarks have been observed. In the energy region that we are concerned with, q^2 of order 1000 GeV^2, α_s is small ($O(\frac{1}{5})$), but still much larger than $\alpha \simeq \frac{1}{137}$.

The emission of a hard gluon by a quark in the process $e^+e^- \rightarrow$ hadrons, which is equivalent to photon emission in radiative corrections in QED, will lead to a broadening of one

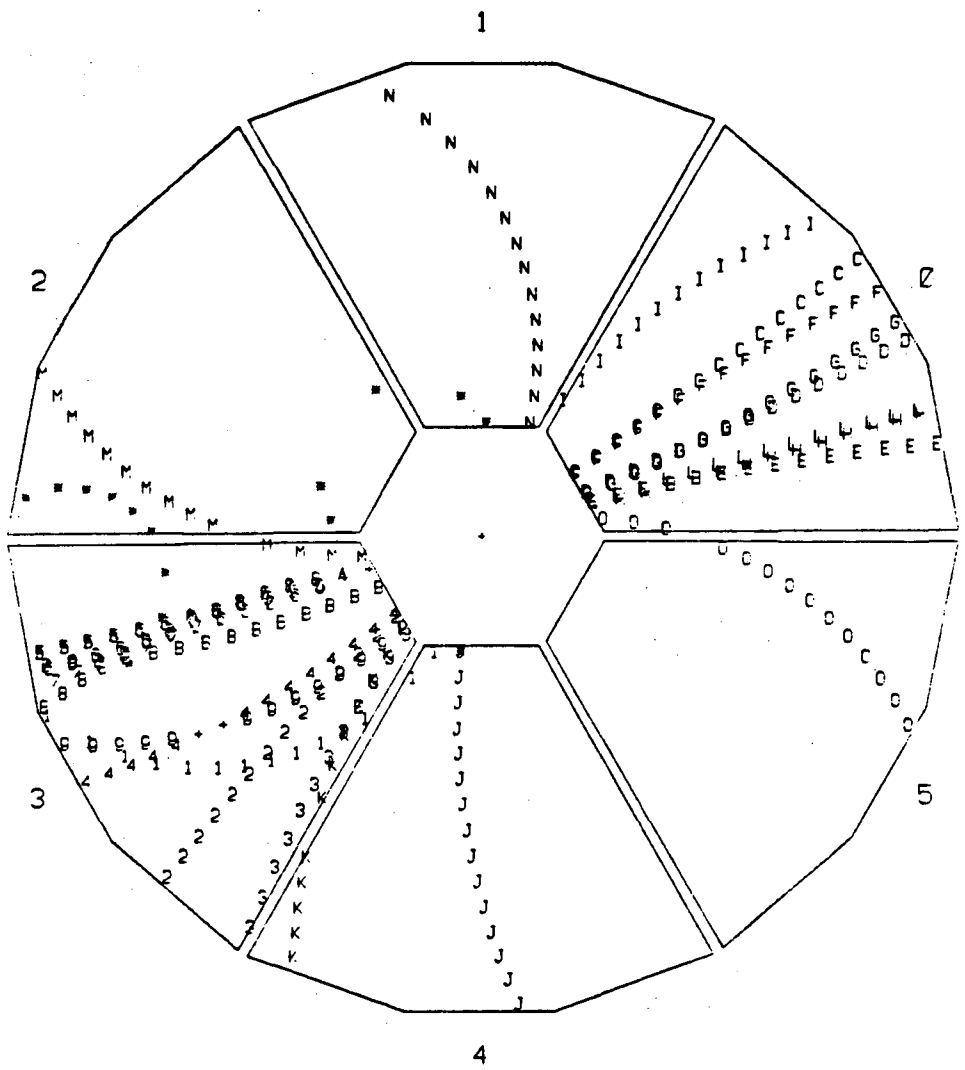

Figure 2.9. A Typical 2 Jet Event as seen in this Experiment

of the quark jets, or, in the extreme case, the observation of three-jet events. Detailed studies of the angular distribution of three-jet events strongly favor vector gluons and rule out scalar gluons.(For a review of the gluon spin determination, see Wolf 81.)

We view the reaction $e^+e^- \rightarrow$ hadrons as taking place in two steps with different time scales. First, the initial e^+e^- pair annihilate into a $q\bar{q}$ or $q\bar{q}g$. Second, the quarks and gluons transform themselves into hadrons, which are the only experimentally observed objects. This second stage is called hadronization and is characterized in the Feynmann-Field model [Field 78] by a step by step process in which the leading quark transforms into a hadron by combining with an antiquark from a quark-antiquark pair pulled from the vacuum. The leftover quark then transforms in the same manner and so on until all of the available energy has been taken up, and all of the primary hadrons have been produced (see Fig. 2.4). The unstable primary hadrons then decay until only those particles sufficiently long lived to be observed in the detector remain.

In more recent models of the hadronization process [Andersson 79, Casher 79, 80], a color force field, sometimes called a string, is created between the rapidly separating quark and antiquark. After the energy per unit length in the field exceeds a given value (usually taken to be $\approx$ 1 GeV/fermi), an additional quark-antiquark pair is produced and pulled apart by the field. The process repeats and more quark-antiquark pairs are produced. The quarks and antiquarks then combine to form the observed hadrons, with the slowest hadrons being formed first. This is opposite to the Feynmann-Field model in which, on the average, the first particle formed is the fastest.

If the probability for a quark (or antiquark) to transform into a hadron is a function only of the fraction of the quark momentum carried by the hadron, then the inclusive cross section,

$$\frac{s}{\beta}\frac{d\sigma}{dx}(e^+e^- \rightarrow \text{hadron}(x)), \qquad \text{where} \quad x = \frac{E_{hadron}}{E_{beam}}, \tag{2.3}$$

will be independent of s or the beam energy, for $E_{hadron} \gg M_{hadron}$. This scaling effect has been observed over a range of energies from 5 GeV to 35 GeV (For a review of scaling in e^+e^-

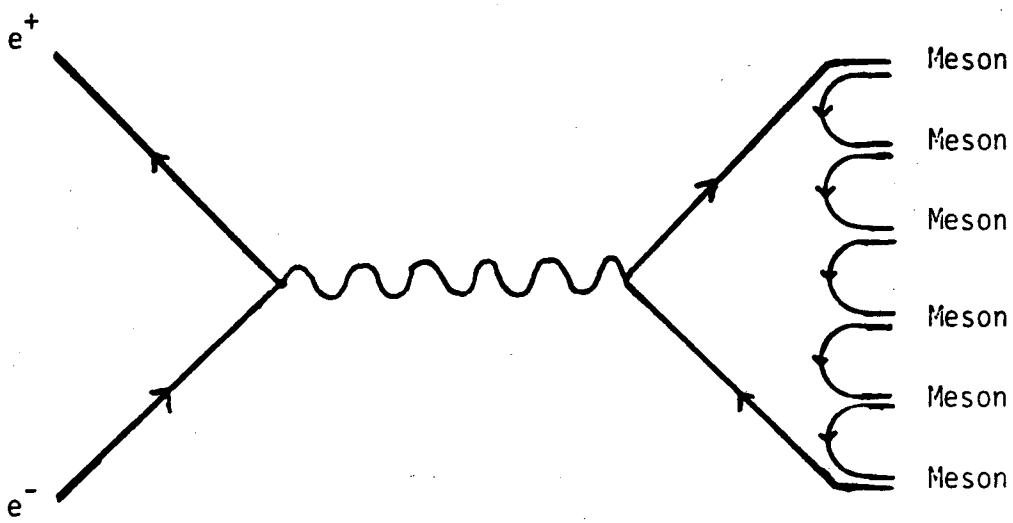

Figure 2.4. $e^+e^- \rightarrow$ hadrons

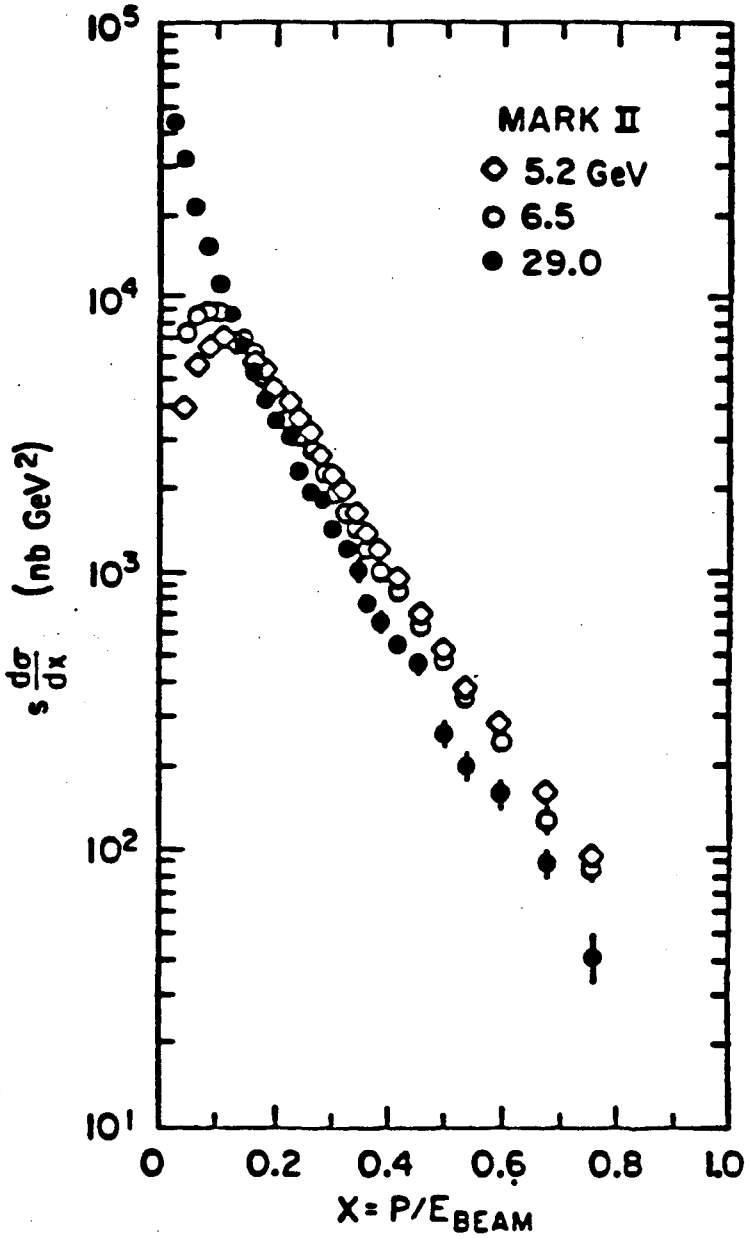

Figure 2.5. $sd\sigma/dx$ at 5.2, 6.6, and 29 GeV. From Patrick 82

interactions, see Wiik 80.) Recently, measurements of sufficient accuracy have been made to observe scale breaking at large x between data taken at 5 GeV and data taken at 29 GeV [Patrick 82, Brandelik 82a] (See Fig. 2.5). At high x, the high energy cross section is lower than the low energy cross section. This effect is expected within the framework of QCD where the emission of gluons by the quarks lowers the effective quark momentum and, therefore, the number of particles at high x. At high energies, despite the decreased α_s, more gluons are emitted, because there is more available energy, and scale breaking occurs.

The step by step picture for hadronization predicts that the properties (e.g. charge, rapidity, strangeness) of neighboring particles should be strongly correlated. For example, we would expect neighboring particles to be oppositely charged, where neighboring particles share a $q\bar{q}$ pair and should be close in rapidity. The effects of decays and fluctuations in the production process smear out such correlations, but they should still be observed on average. Short range charge correlations, in which particles close in rapidity have opposite charges when averaged over many events, have been observed [Brandelik 81], although separating the relative sizes of the contributions to the correlation from the hadronization process itself and from decays is difficult.

One of the parameters controlling inclusive particle production in this picture is the frequency with which a $q\bar{q}$ pair of a particular type is pulled from the vacuum relative to the other types. Because of the larger energy fluctuation required to create a heavy $q\bar{q}$ pair, we would expect the production of heavy $q\bar{q}$ pairs to be suppressed relative to that of light $q\bar{q}$ pairs. We note that the relevant energy scale is set by the $\approx$ 1 GeV/fermi of energy per unit length for producing quark-antiquark pairs in the color field between the original quark and antiquark [Andersson 80]. This is much smaller than the energy available for the production of the original quark-antiquark, which is essentially the full center of mass energy. Since the charm and bottom quarks are quite massive, we would expect their production to be quite small relative to that of the up, down and strange quarks. Theoretical estimates of the suppression of charm quark production from the

vacuum relative to up quark production range from 10^{-11} to 10^{-2} [Andersson 80, Furmanski 79]. Since the strange quark is slightly heavier than the up and down quarks, its production rate should be somewhat suppressed. Theoretical estimates for suppression of strange quark production from the vacuum relative to up or down quark production range from 1/2 to 1/3 [Field 78, Andersson 80]. By measuring the kaon production cross section, the probability of producing strange $q\bar{q}$ pairs from the vacuum relative to that of up and down $q\bar{q}$ pairs can be studied. We will discuss this in interpreting our results on charged kaon production.

The scheme for hadronization via the production of $q\bar{q}$ pairs from the vacuum does not include the possibility of baryon production. A number of extensions of the model have been proposed which include baryon production [Andersson 81, Hofmann 81, Meyer 81, Ranft 80, Ilgenfritz 78, Casher 79, 80]. The simplest of these is that diquark-antidiquark ($qq\bar{q}\bar{q}$) pairs are pulled out of the vacuum as well as quark-antiquark pairs (see Fig. 2.6). By measuring the baryon cross sections, the amount of diquark production or similar quantities in different models, can be determined. We note that diquarks cannot be point particles, since, if they were, they would contribute to a large increase in the value of $R = \sigma(e^+e^- \rightarrow \text{hadrons})/\sigma(e^+e^- \rightarrow \mu^+\mu^-)$ which has not been observed. A conceptually different approach relies on quark alignment in the color field [Casher 79, 80]. We present a simplified summary of the model here. Let $q_a\bar{q}_a$ be an initial quark pair, where a is the color index. Assume that the $q\bar{q}$ pair pulled from the vacuum as q_a and $\bar{q}_a$ move apart has color index b. Then, if $a = b$, $\bar{q}_b$ will be attracted by q_a and q_b will be attracted by $\bar{q}_a$, and mesons will be produced (See Fig. 2.7b). If $a \neq b$, q_a will attract q_b and $\bar{q}_a$ will attract $\bar{q}_b$ (See Fig. 2.7c). As the quarks continue to separate, a new pair, $q_c\bar{q}_c$, will be created. If $a \neq b \neq c$, then q_c will be attracted by q_aq_b, and $\bar{q}_c$ will be attracted by $\bar{q}_a\bar{q}_b$. In this case, baryons will tend to be formed.

These recursive schemes for hadron generation naturally lend themselves to event simulation by Monte Carlo techniques. A number of such Monte Carlo event generators exist, and two in

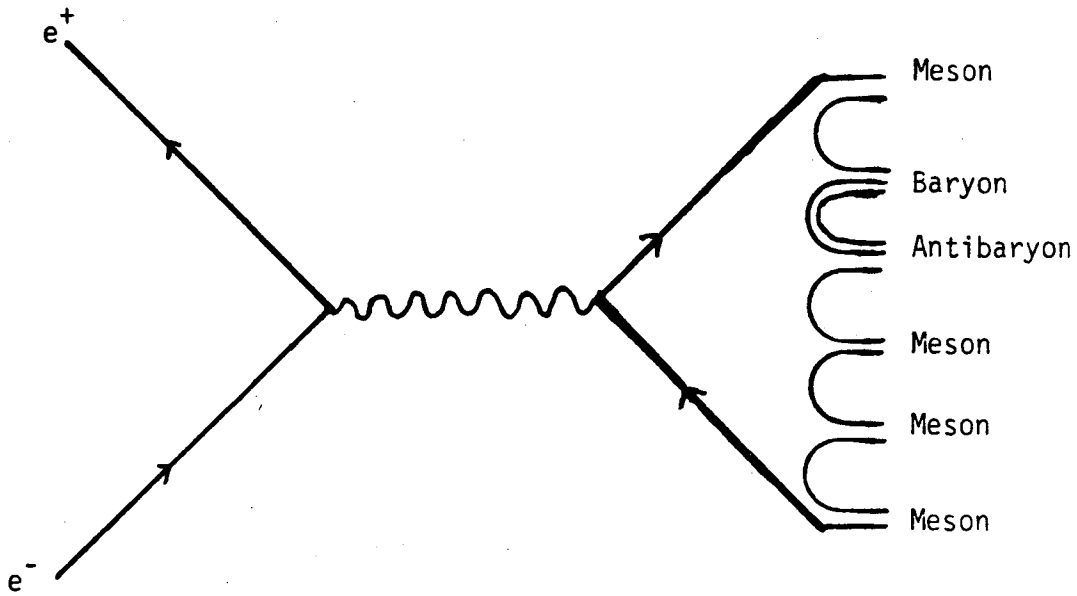

Figure 2.6. Baryon Production via Diquark Antidiquark Pairs

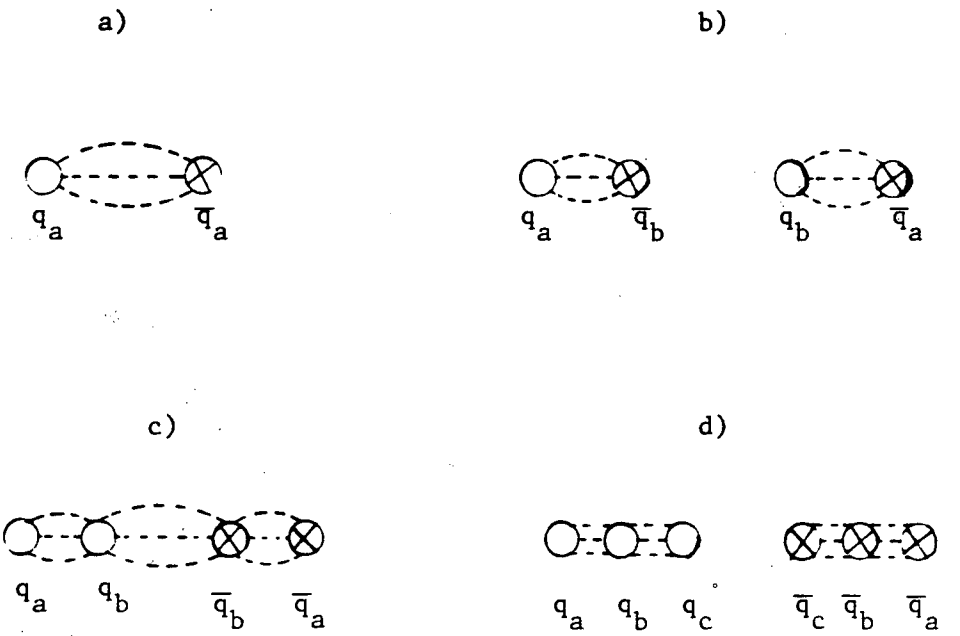

Figure 2.7. Meson (b) and Baryon (c,d) Production in the Model of Casher 79 —Figure from Wolf 82

particular, the Hoyer (or Ali) Monte Carlo [Hoyer 79, Ali 80], and the LUND Monte Carlo [Sjostrand 82], are widely used by most e^+e^- experiments. These models differ in their handling of gluon jets and in their quark and gluon fragmentation functions, D(z). The fragmentation functions give the probability for a hadron of momentum fraction $z = P_{hadron}/P_{quark}$ to be produced by a given quark or gluon. The Monte Carlos contain a large number of parameters including the average transverse momentum with respect to the quark axis, the probability of producing $s\bar{s}$ pairs from the vacuum, the probability of producing vector relative to scalar, and many, many others, and have been quite successful in duplicating the data.

In this thesis, we will study inclusive particle production and will interpret our results in terms of hadronization models, using our results to determine some of the model parameters. Quantitative measurements of the various Monte Carlo model parameters will, of course, be extremely model dependent. Interpreted qualitatively, however, the results will characterize the hadronization process in general.

Chapter 3

PEP and the PEP-4 Detector

The data to be discussed in this dissertation were taken with the PEP-4 (Time Projection Chamber or TPC) detector operating at the PEP e^+e^- storage ring at SLAC, the Stanford Linear Accelerator Center.

3.1 PEP

The PEP e^+e^- storage ring was completed in early 1980 (see Fig. 3.1). The ring is 2.2 km in circumference. Besides the TPC, there are five other detectors at PEP: Mark II, MAC, DELCO, HRS, and PEP-9, the 2-γ detector. The maximum design center of mass energy of the PEP ring is 36 GeV. To date, PEP has operated only at 29 GeV. The energy spread of the beams is given by $\frac{\sigma_E}{E} \approx 10^{-3}$, leading to an energy spread of about 200 MeV at 29 GeV. The storage ring is filled with three bunches of 14.5 GeV electrons and positrons from the linear accelerator. The beams collide every 2.45 μs at each interaction region. During May and June 1982 when the data used in this dissertation were taken, typical injection times were 30 minutes to one hour. Typical beam lifetimes between fills were two to three hours. The best luminosity that was obtained was $1.3 \times 10^{31} cm^{-2} s^{-1}$. In a good day of data taking, the TPC detector received about 200 to 300 nb^{-1}, resulting in 80 to 120 hadronic events.

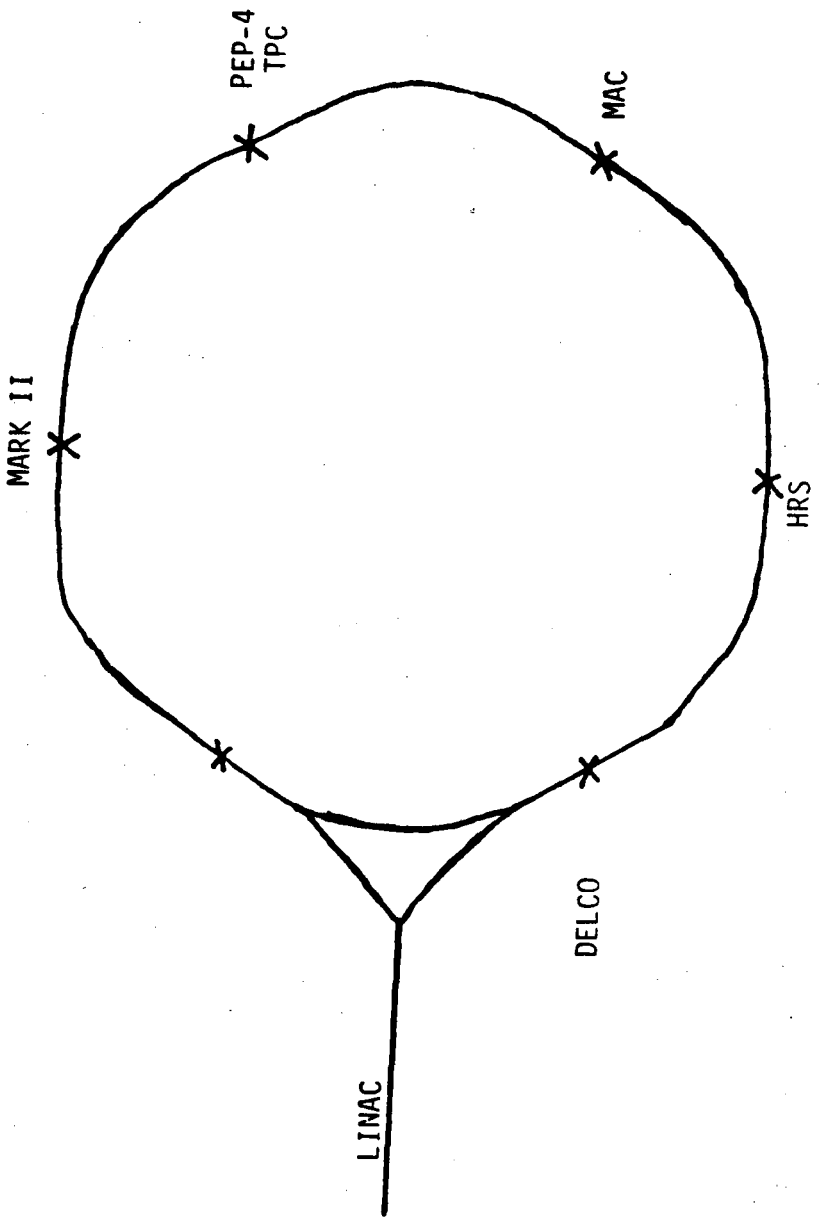

Figure 3.1. PEP e^+e^- Storage Ring

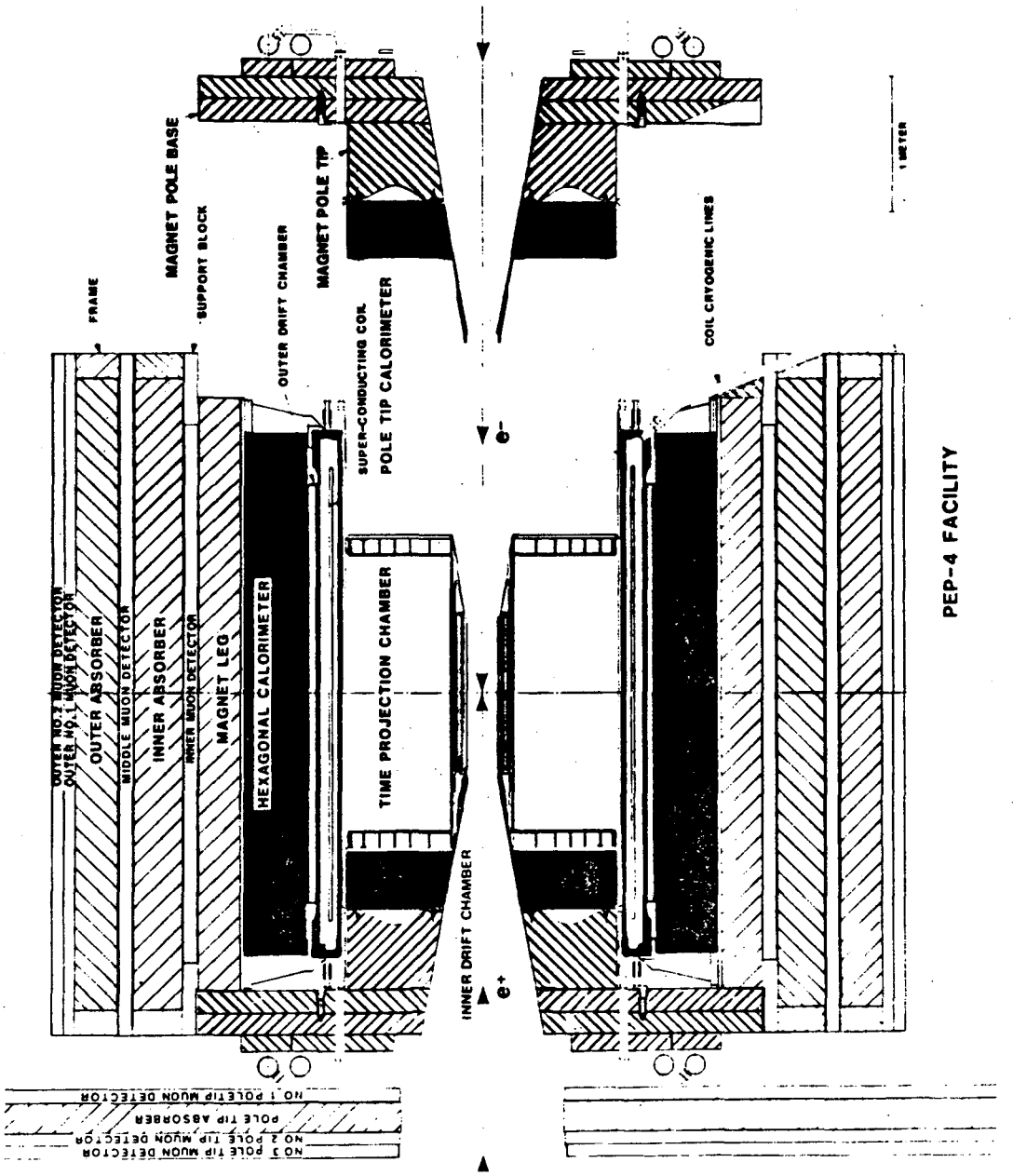

Figure 3.2. The PEP-4 (Time Projection Chamber) Detector — Side view

3.2 PEP-4 Detector

The PEP-4 facility is a large colliding beam detector (see Fig. 3.2). It was first assembled in the fall of 1981, tested with cosmic rays, and then installed in the PEP beam line in January 1982. After further checkout, data taking was started in April 1982. The data used in this dissertation were taken in a 6 week run during May and June 1982, just prior to the PEP summer shutdown.

Starting from the beam line (see Fig. 3.2), the PEP-4 facility consists of the following elements: an inner pressure wall, the inner drift chamber, the Time Projection Chamber itself, the outer pressure wall, the magnet coil, the outer drift chamber, the hexagonal calorimeter, and alternating layers of muon chambers and iron. Poletip calorimeters and endcap muon chambers detect particles that remain close to the beamline.

We will now describe each of the main detector systems in more detail. We will discuss the TPC last and at considerable length, since it was the detector primarily used in the analysis.

The standard PEP-4 coordinate system is shown in figure 3.3. The origin is the nominal beam interaction point. The z axis lies along the beam line. The y axis is vertical, and the x axis points to the center of the ring. θ and ϕ are the standard polar angles. $r = \sqrt{x^2 + y^2}$, is the radial distance from the beam line.

The beam pipe is water cooled, 2 mm thick, and located 8.5 cm in radius (r) from the beam line. The inner pressure wall is 6.35 mm thick and located at r = 10.9 cm. The TPC and inner drift chamber can operate at pressures from 1 to 10 atmospheres. The gas mixture normally used is 80% argon 20% methane.

The inner drift chamber has 4 layers of sense wires. It is inside the high pressure volume and occupies the region from 13.2 cm to 19.4 cm in radius. In cosmic ray tests, the resolution of the IDC was 150 microns. Unfortunately, prior to the May June 1982 data taking, the IDC

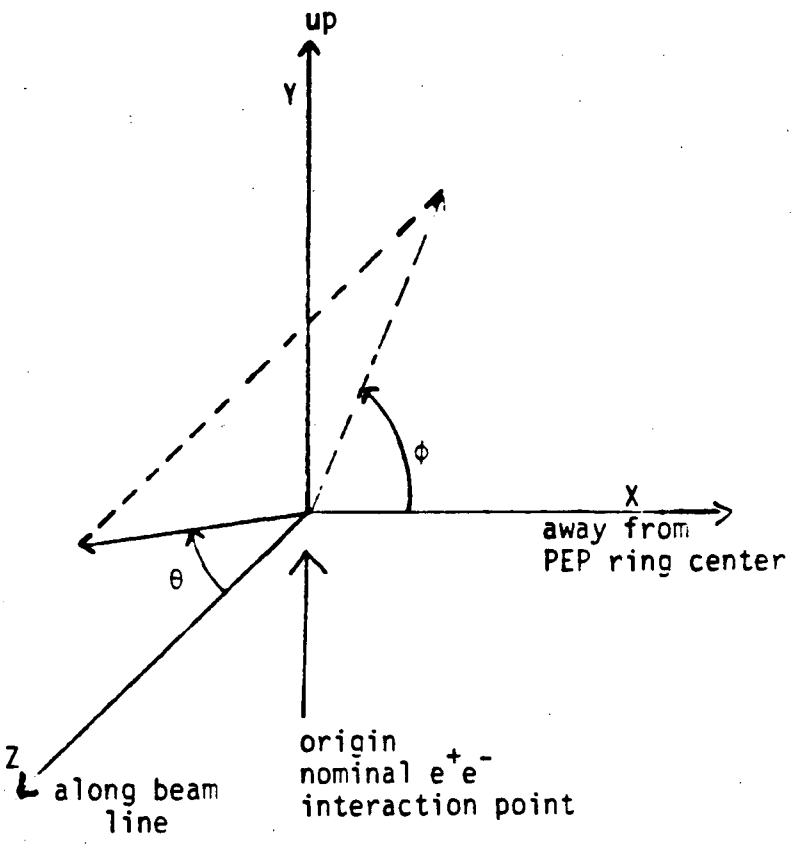

Figure 3.3. PEP-4 Coordinate System

failed due to the high background radiation in the PEP environment. It was not, therefore, used in any of this analysis. The TPC is located outside the IDC and inside the magnet coil. It will be discussed later.

The aluminum magnet coil is located about 107 cm from the beam line. It provides a 4 kG solenoidal magnetic field.

The outer drift chamber (ODC) is outside the magnet. There are six ODC modules. They are designed to overlap so that there are no azimuthal gaps between them. Each module has three layers of sense wires. They operate at one atmosphere in 80% argon 20% methane gas, and have a resolution of about 200 microns. The fast information available from the outer drift chamber was an important part of the PEP-4 trigger. The data from the ODC was not otherwise used in this analysis. Both the outer and inner drift chambers are described in more detail in Aihara 83a.

The hexagonal calorimeter modules each have 40 layers of sense wire planes alternating with planes of $\approx$ 3.2 mm thick lead laminates and cover about 55% of the 4π solid angle. Each module is 10 radiation lengths thick. The chambers are operated at 1 atmosphere in the geiger discharge mode. Each track is seen in three 60° stereo views, providing excellent track reconstruction capability. A preliminary measurement of the energy resolution for Bhabha electrons in the Spring 1982 data gave $\frac{\sigma_E}{E} = 17\%$. During the Spring of 1982, only two of the six hexagonal calorimeter modules were installed. The hexagonal calorimeters are described in more detail in Aihara 83b.

The two proportional wire poletip calorimeters (PTC) are each 13.7 radiation lengths thick with 51 layers of sense wire planes and aluminum-clad lead. The poletip calorimeters are inside the pressure volume, leading to improved energy resolution, and have three 60° stereo views. For Bhabha electrons, the energy resolution has been measured to be 6.5% and the angular resolution, 1.3 milliradians. Bhabha events in the poletip calorimeter are used as a luminosity

monitor. The PTC is described in more detail in Marx 82.

The PEP-4 muon chambers cover approximately 90 % of the total solid angle. They are made of 3284 extruded aluminum drift chamber cells, each a triangle $\approx$ 8 cm on each side. The chamber single cell efficiency, as measured at PEP, is greater than 99.6% . Tracks reaching the outer layers of the barrel muon chambers must cross at least 90 cm of iron. Tracks reaching the outer layers of the endcap muon chambers must cross at least 50 cm of iron. The muon chambers are described in more detail in Aihara 83c.

3.3 Time Projection Chamber

The Time Projection Chamber, itself, is a large drift chamber, two meters long and two meters in diameter (see Fig. 3.4). The chamber gas is usually 80% argon and 20% methane at 8.5 atmospheres. The TPC drift volume is divided in half by the high voltage membrane, which is normally operated at 75 KV. The two detection endplanes are held at ground potential. A series of equipotential rings between the endcaps and the high voltage membrane provides a uniform electric field in the direction parallel to the beam pipe. A track passing through the TPC ionizes the gas along its path. The ionization electrons drift under the influence of the electric field to the endcaps where they are detected.

Each endcap is composed of six identical multiwire proportional chambers (sectors). (See Fig. 3.5). Each sector has 183 sense wires and 15 rows of segmented cathode pads. The nearly equally spaced pad rows are each centered under a sense wire. The pads are 7.5 mm $\times$ 7.5 mm square. The electron avalanches on the wires above the pad row induce signals on two or three of the pads below where the avalanche occurs (see Fig. 3.6). The exact position of the avalanche along the pad row is then determined from the center of gravity of the pad signals. The original position of the track segment in z, the drift direction, is determined by the time it takes the ionization to drift to the sector. The original time of the track arrival is known either

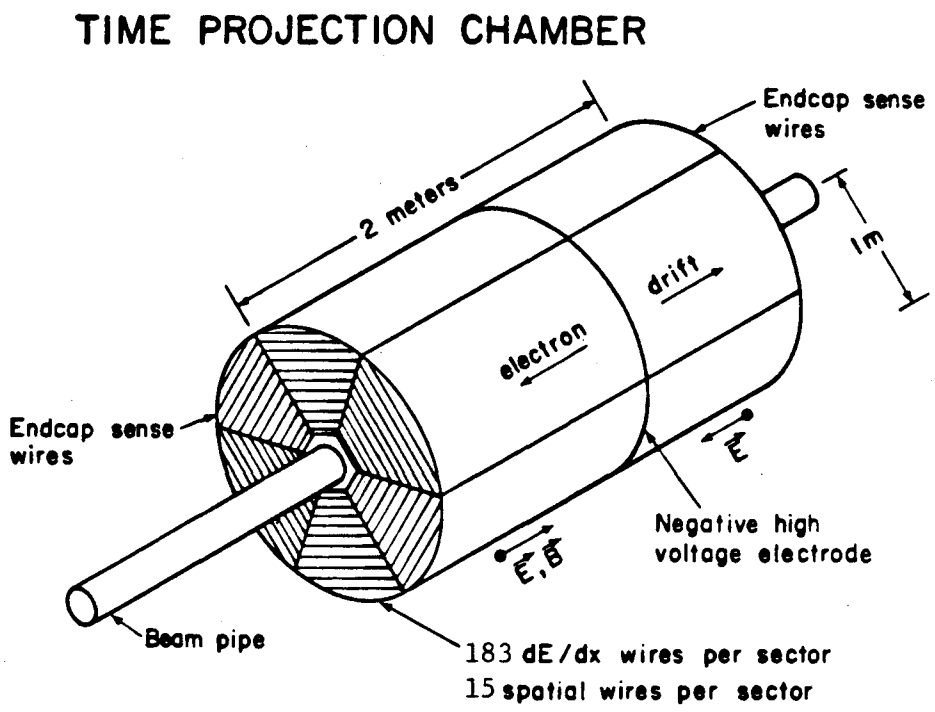

Figure 3.4. Time Projection Chamber

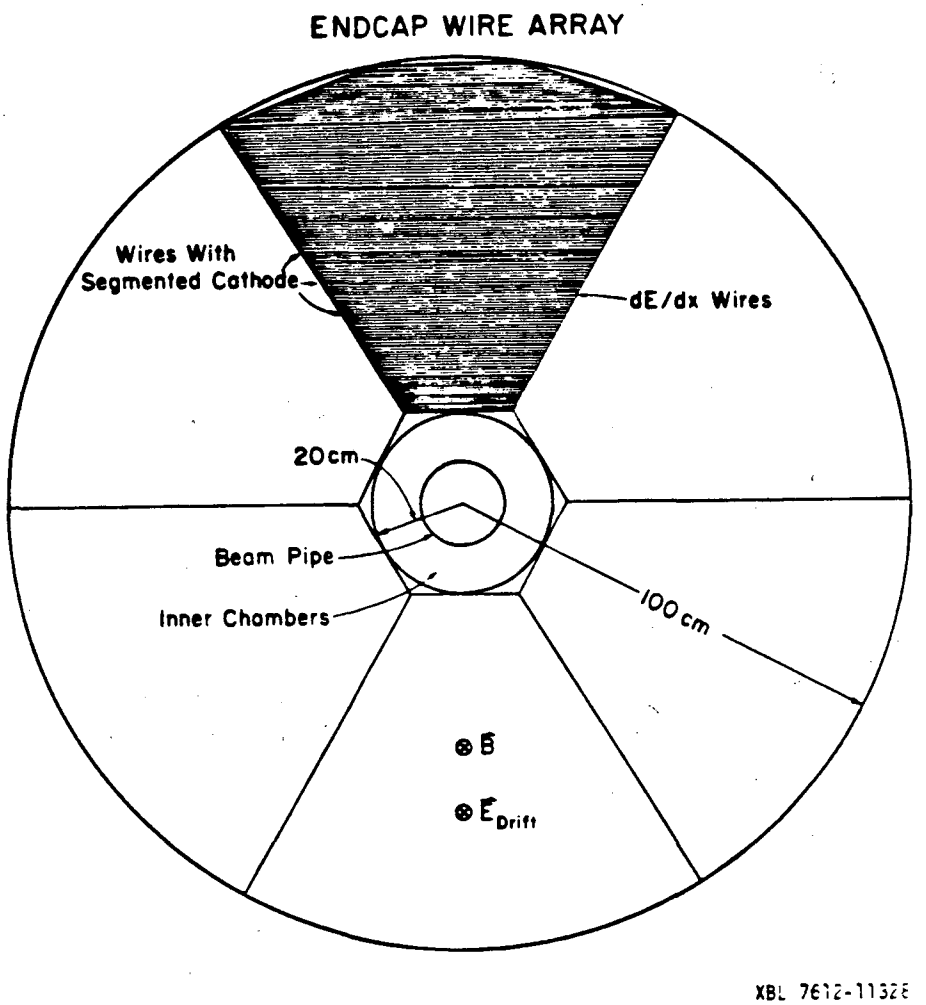

Figure 3.5. TPC Sectors — End View

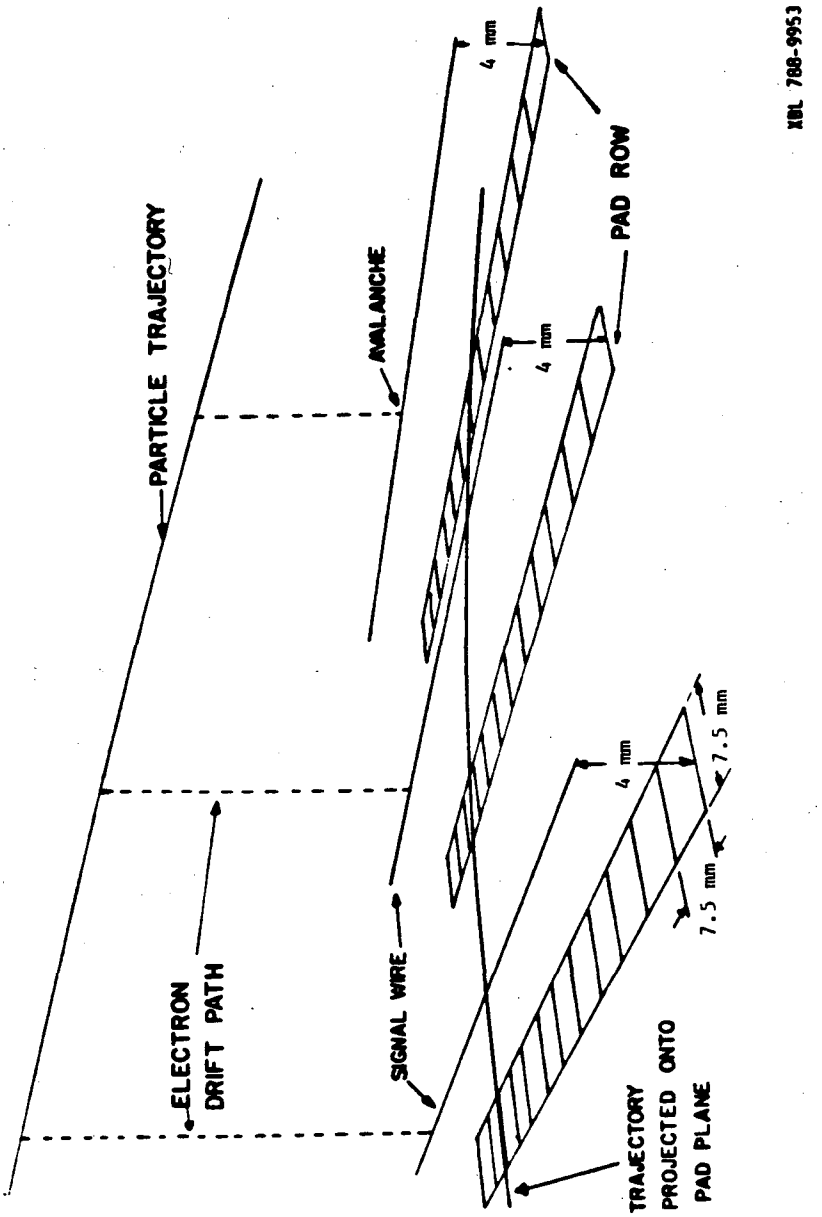

Figure 3.6

Simplified Representation of a Track Passing Through the TPC. Note that only the sense wire directly over a pad row is shown, although the signals from the five nearest sense wires contribute to the pad signals.

from the beam crossing time or from one of the fast timing detectors, the IDC or ODC. The information from each pad hit is three dimensional, thereby simplifying pattern recognition.

The track's helical trajectory in the 4 kG magnetic field and its momentum are determined from the pad hits. The associated sense wire signals provide a measurement of the track's ionization. Since particles deposit energy by ionization in a gas according to their velocity, it is then possible to determine the particle type. This is a central strength of the TPC concept, the simultaneous measurement of particle momentum and mass with one detector.

3.3.1 TPC Electronics

Each of the 13824 TPC pads and 2196 sense wires is connected to an individual electronics channel. Each channel consists of a preamplifier, a shaping amplifier, a charged coupled device (CCD) and a digitizer. Each channel must provide pulse height information that is accurate to 1% and timing information that is accurate to $\approx$ 20 ns.

Signals are first amplified and shaped by the preamplifiers and shaping amplifiers and then go into the CCD's which act as analog shift registers. As the data streams in, each signal is sampled every 100 ns by the CCD's. The individual measurements are called buckets. The CCD clock is slowed down for readout, and one bucket is digitized every 50 μs. The digitized information is first sent to the online computer and then to magnetic tape.

Under standard TPC operating conditions, the electrons drift through the TPC gas at $\approx$ 5 cm/μs. An entire event, therefore, takes a maximum of 20 μs to drift through the TPC. This corresponds to 200 buckets. Given the large number of channels and the large number of buckets per channel, the information in a given bucket is only read out if it is above a preset threshold. These thresholds are often called lower limit RAM's. Even if there is no input signal, the CCD output is nonzero when digitized. This offset or pedestal varies from channel to channel

and has to be determined when the electronics are calibrated. A typical input signal from a pad or wire has 5 to 7 CCD buckets above threshold. The signal pulse height and time of arrival are determined by fitting a parabola to the highest three buckets. This group of 5 to 7 buckets from a single input signal is called a cluster.

The response of the CCD's is nonlinear and has to be calibrated carefully to obtain the desired 1% accuracy. From repeated calibrations made during the May–June 1982 data taking, the system stability, and, in particular, the pedestal variations were at the 1% level when compared with the signal expected from a minimum ionizing track [Aihara 83d]. The TPC pad electronics were calibrated by pulsing the grid wires over the pad rows. The TPC sense wire electronics were calibrated by pulsing capacitors connected to the input of the wire preamplifiers. For a detailed description of the TPC electronics, see Aihara 83d.

3.3.2 TPC Pad Response

Each sector has 1152 pads giving a total of 13824 for the whole TPC. The signal seen on a given pad is a result of the avalanches on the five sense wires closest to the pad. See Fig. 3.6 for a simplified view of the pad and wire response to a track passing though the TPC. In the figure only the sense wire directly over a pad row is shown, although signals from the five nearest wires contribute.

The pad response, H_p, to a signal on the sense wires above the pad row is very well represented by a gaussian shape [Aihara 83e].

$$H_P = \left(\sum_{i=-2}^{2} w_i H_i \right) e^{-\eta^2/2\sigma^2} \tag{3.1}$$

H_p is the pad pulse height.

η is the distance along the pad row from the pad center to the signal on the wire.

σ is the width of the pad response.

H_i is the pulse height on wire i.

w_i is the weight for wire i.

Typically, the five wires nearest the pad row contribute to the pad pulse height. If wire 0 is the wire directly over the pad row, wires ± 1 its neighbors, and wires ± 2 the next neighbors, then $w_0 = 0.239$, $w_1 = w_{-1} = 0.117$, and $w_2 = w_{-2} = 0.0135$.

Since σ is about one half of the pad size, typically only two or three pads are above threshold for a given hit. On average, 55% of the hits have two pads above threshold, 40% three pads, and 5% one pad [Aihara 83e] . For the three pad case, σ and η, the position, can be directly determined from the measured pulse heights. If, however, only two pads are above threshold, then σ must be calculated from other information before η can be determined. Since the desired accuracy in the determination of η is of order 100 microns, σ must be determined that accurately as well.

σ may be described as the sum of three different terms [Aihara 83e].

$$\sigma^2 = \sigma_0^2 + \sigma_1^2 + \sigma_2^2 \tag{3.2}$$

σ_0 is the pad width due to a point charge at the sense wire.

σ_1 is the contribution due to diffusion.

$$\sigma_1^2 = (1 + \tan^2 \alpha)\sigma_D^2 \frac{L}{L_{Max}} \tag{3.3}$$

α is the angle between the track and the direction normal to the sense wires (see Fig. 3.7). L is the drift distance and L_{Max} the maximum drift distance. For the TPC, $L_{Max} = 1$ meter. σ_D is the transverse diffusion distance for a single electron that has drifted L_{Max}. The $\tan^2 \alpha$ factor allows for the contribution from diffusion in the direction normal to the wires for angled tracks.

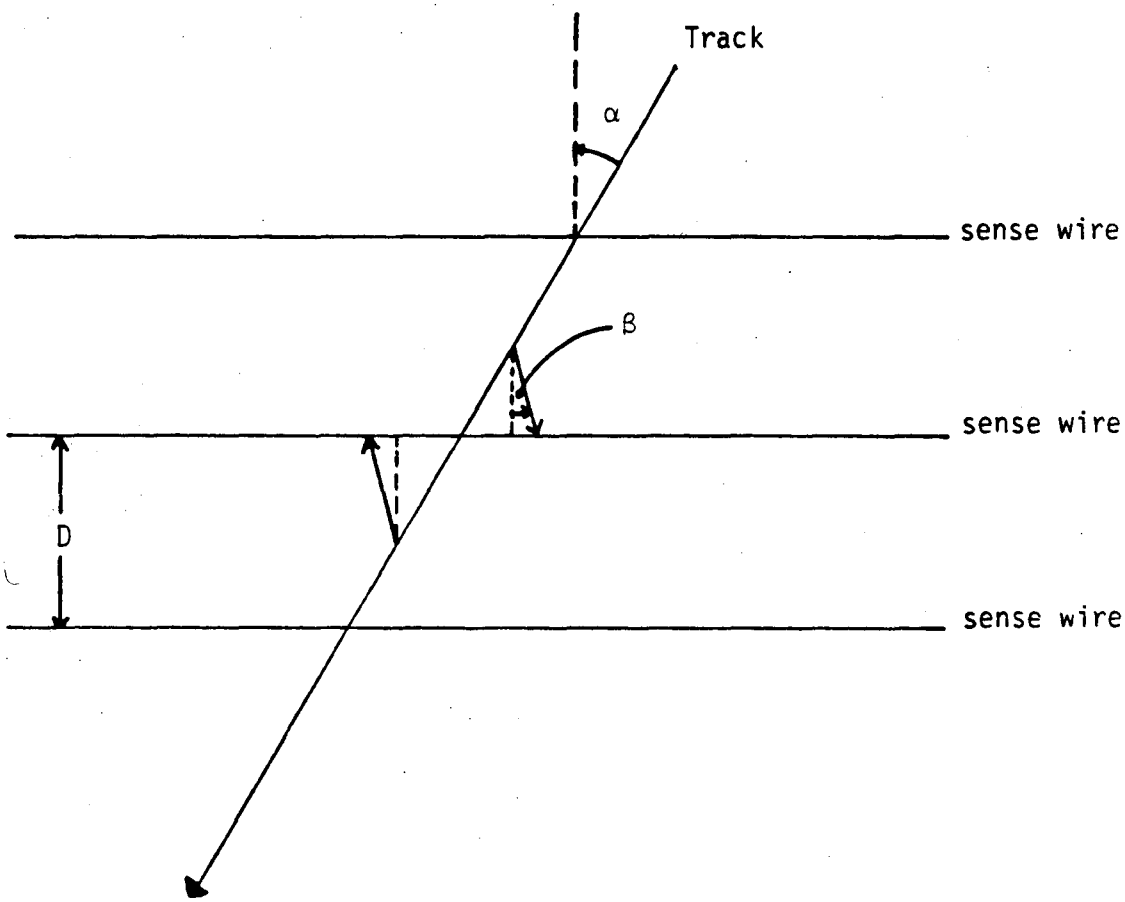

Figure 3.7. Track Angles for Determining the Pad Response

σ_2 includes the contributions for angled tracks due to geometry and $E \times B$ effects in the region near the wire [Hargrove 82].

$$\sigma_2^2 = (\frac{1}{12}(\tan\alpha - \tan\beta)^2 + S_2 \tan^2\alpha)D^2 \tag{3.4}$$

D is the distance between sense wires. D = 4 mm.

S_2 is equal to $\sum_{i=-\infty}^{\infty} i^2 w_i$, where the sum of the wire weights, w_i, is normalized to 1. The term $D^2 S_2 \tan^2\alpha$ accounts for the broadening of the pad signal width due to the contribution of different wires to the signal. Good agreement with the data can be obtained by considering only the five wires closest to the pad row.

The force on the moving electrons due to the magnetic field, B, which is perpendicular to the plane of the paper in Fig. 3.7 causes the electrons to drift at an angle β with respect to the direction normal to the sense wires (see Fig. 3.7). The $\tan\beta$ factor takes into account the correction to the width due to this small change in the electron drift direction. The $\frac{1}{12}D^2(\tan\alpha - \tan\beta)^2$ term accounts for the ionization's not being collected from a point, but from a line.

By measuring σ^2 from the three-pad data as a function of L, the drift distance, and α, the track crossing angle, the parameters, σ_D, σ_0, β, and $\sigma_a \equiv D^2(\frac{1}{12} + S_2)$ can be determined.

At 8.5 atmospheres and 4 kG magnetic field, the standard TPC operating conditions, σ_D was measured to be: [Aihara 83e]

$$\sigma_D = 1.40 \pm .01 mm. \tag{3.5}$$

σ_D was also measured at different pressures, P, and values of the magnetic field, B, during cosmic ray tests (see Table 3.1) . The errors given in the table are statistical only. The systematic errors are estimated to be $\approx$ 15%. We expect [Townsend 48] for diffusion transverse to a magnetic field that:

$$\sigma_D(B) = \frac{\sigma_D(B=0)}{\sqrt{1+\omega^2\tau^2}} \qquad and \qquad \sigma_D(B=0) \;\alpha\; P^{-1/2} \tag{3.6}$$

$\omega \equiv \frac{eB}{mc}$ is the cyclotron frequency.

τ is the mean collision time.

The suppression of diffusion due to the magnetic field is negligible at 8.5 atmospheres, but does contribute at lower pressure. $\sigma_D(B = 0)$ is well described as varying as $P^{-1/2}$ as expected. The quoted values for $\omega\tau$ were calculated from the measured values of σ_D using the formula given above.

P [atm]	B [kG]	σ_D [mm]	$\sigma_D\sqrt{P}$ [mm atm$^{1/2}$]	$\omega\tau$
8.64	0	$1.33 \pm .09$	$3.91 \pm .38$	-
4.02	0	$1.92 \pm .07$	$3.85 \pm .12$	-
1.50	0	$3.13 \pm .08$	$3.83 \pm .10$	-
8.64	4	$1.32 \pm .05$	-	$.1 \pm .6$
8.50	4	$1.20 \pm .01$	-	-
4.02	4	$1.59 \pm .04$	-	$0.68 \pm .14$
1.50	4	$1.84 \pm .06$	-	$1.38 \pm .11$

Table 3.1. Diffusion *vs.* P and B

The values of $\omega\tau$ are in good agreement with those calculated from kinetic theory [Townsend 48]:

$$\omega\tau = 1.09\left(\frac{V_d}{c}\right)\left(\frac{B}{E}\right) \text{ in c.g.s. units.} \tag{3.7}$$

Here V_d is the drift velocity and E, the electric field. See table 3.2 .

P [atm]	B [kG]	E [kV/m]	V_d [cm/μs]	$\omega\tau_{Meas}$	$\omega\tau_{Calc}$
8.64	4	75	$4.76 \pm .08$	$.1 \pm .6$	.27
4.02	4	35	$4.51 \pm .09$	$.68 \pm .14$	.56
1.50	4	13.2	$4.06 \pm .08$	$1.38 \pm .11$	1.33

Table 3.2. $\omega\tau$

σ_a and β were determined by fitting σ^2 to a second order polynomial as a function of $\tan\alpha$. From the fit,

$$\sigma_a = 3.65 \pm .02mm \qquad \beta = 4.2^o \pm .3^o. \tag{3.8}$$

σ_0 can be determined from either the fit of σ^2 *vs.* L or the fit of σ^2 *vs.* $\tan\alpha^2$. σ_0 was found to be [Aihara 83e]:

$$\sigma_0 = 3.59 \pm .01mm. \tag{3.9}$$

Measurements of σ_0 at different pressures and values of the magnetic field yield the same result within errors [Galtieri 82], confirming the assumption that σ_0 is a function only of the pad and wire geometry. σ_0 is very sensitive to changes in the electronics calibration, however. Different calibrations have led to changes in σ_0 of as much as $0.1mm$.

3.3.3 Spatial Resolution

Once the change in the pad response width, σ, as a function of drift distance and track angle, α, has been determined accurately, the spatial resolution for good two-pad hits and three-pad hits is the same [Madaras 83].

The spatial resolution perpendicular to the drift direction, σ_{xy}, can be expressed as (neglecting the $\tan\beta$ term) [Aihara 83e]:

$$\sigma_{xy}^2 = \sigma_A^2 + \frac{\sigma_1^2}{N} + \sigma_C^2 e^{\gamma L} \cos\alpha \tan^2\alpha \tag{3.10}$$

α, L, σ_1 are as defined before. N is the effective number of drift electrons resulting in the pad hit, and γ is the electron capture rate per unit distance.

The first term, σ_A^2, is the intrinsic resolution.

The second term, $\frac{\sigma_1^2}{N}$, is the diffusion contribution to the resolution. The effective number of electrons, N, is given by $N = N_0 e^{-\gamma L} \sec\alpha$. N_0 is the original number of electrons. $e^{-\gamma L}$ accounts for the reduction in the number of drift electrons due to electron capture by the gas, and $\sec\alpha$ takes into account the increase in N due to the increase in track length. Thus,

$$\frac{\sigma_1^2}{N} = \sigma_B^2 \frac{L}{L_{Max}} e^{\gamma L} \sec\alpha. \tag{3.11}$$

where σ_B is a constant.

The third term, $\sigma_C^2 e^{\gamma L} \cos\alpha \tan^2\alpha$, is due to ionization fluctuations with each sense wire cell.

The spatial resolution, σ_{xy}, was measured by fitting a gaussian to the residuals of pad rows left out of the track fit in the cosmic ray data. By fitting the variation of σ_{xy} *vs.* L to a straight line, σ_B was measured to be [Aihara 83e]:

$$\sigma_B = 105 \pm 6\mu. \tag{3.12}$$

By fitting σ_{xy} as a function of α, σ_C was measured to be [Aihara 83e]:

$$\sigma_C = 249 \pm 7\mu. \tag{3.13}$$

From both the fits to σ_{xy} as a function of L and α, σ_A was measured to be [Aihara 83e]:

$$\sigma_A = 160 \pm 2\mu. \tag{3.14}$$

The spatial resolution in the bending plane, σ_{xy}, therefore, varies from about 160 microns to about 250 microns for tracks at large angles ($\alpha_{Max} = \pm 30^{o}$ due to sector geometry) and long drift distances (1 meter) for the standard TPC operating conditions: $B = 4kG$, $P = 8.5atm.$, 80% argon 20% methane.

As described previously, a pad hit has typically 5 to 7 CCD buckets (each 100 ns apart) above threshold. The pad pulse height and time position are determined by fitting a parabola to the highest three buckets. The time information is then converted to a position in z, the drift and beam axis direction, using a previously determined value for the drift velocity, V_d. The drift velocity is determined by measuring the difference in the vertex positions in z determined using tracks in the two TPC endcaps separately. For the standard TPC operating conditions, $V_d \approx 5cm/\mu s$.

The z position resolution, σ_z was determined similarly to σ_{xy}, by leaving a pad row out of the track fit in z for cosmic rays and fitting a gaussian to the residuals. For the standard TPC operating conditions, σ_z was measured to be [Aihara 83e]:

$$\sigma_z = 340 \pm 5\mu. \tag{3.15}$$

3.3.4 Distortions and Momentum Resolution

Although both the position resolution in the bending plane, σ_{xy}, and in the drift direction, σ_z, are equal to or better than the design values, the TPC momentum resolution is not as good as expected. The reason for this is that the electric field near the field defining cages at the outer and inner radii of the TPC is not uniform, causing the tracks to appear distorted. Furthermore, this field non-uniformity varies with time and changes rapidly over short distances. The electric field near the intermediate radii in the TPC is uniform, however. The pad rows near

the inner and outer radii cannot then be used to measure a track's momentum; this shortens the effective track length, and reduces the momentum resolution.

The field distortions have two sources. One is the distortion due to the buildup of positive ions near the inner radius of the detector caused by the background radiation from the beam. This distortion increases as the beam current increases. The other distortion, which exists even when the beams are off, is caused by unknown problems with the design of the electric field grading system (the field cages).

Besides reducing the effective track length, the field non-uniformities distort tracks to such an extent that the vertex cannot be used in the fit without biasing the track momentum. This bias can be observed, for example, in cosmic rays. When the tracks seen in two sectors from a single cosmic ray are not constrained to have a common point, the momenta of the cosmic ray as measured in the two sectors are equal. On the average, the bias in the curvature is less than .01 $(\mathrm{GeV/c})^{-1}$. However, when the tracks seen in two sectors from a single cosmic ray are constrained to have a common point, the momentum as measured in one sector is systematically larger (or smaller) than the momentum as measured in the other. See Fig. 3.8 for a typical cosmic ray as seen in the TPC.

Without the vertex in the fit, using 10 pad rows, the momentum resolution as determined from cosmic rays measured in two sectors is [Aihara 83e]:

$$\frac{\delta p}{p} = (6.4 \pm 0.3)\%\ \mathrm{p}(GeV/c). \tag{3.16}$$

The multiple scattering contribution to the momentum error is about 4% at 1 GeV/c.

Work on finding a model to use to correct the distortions and increase the effective track length and allow the vertex to be used in the fit is in progress. Unfortunately, such a model has not yet been found. In the analysis done in the remainder of this dissertation, the momenta used will be those obtained without the vertex constraint.

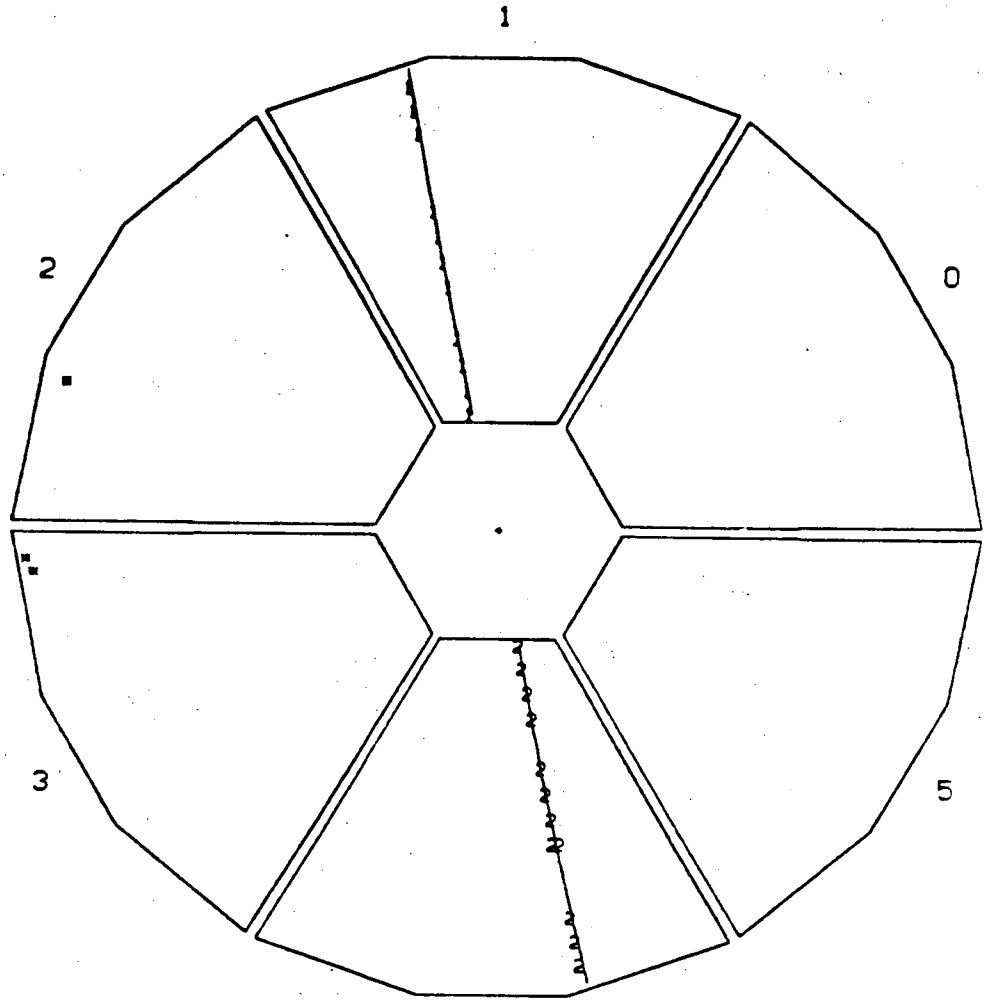

Figure 3.8. TPC Pad Data for a Cosmic Ray

3.3.5 Pattern Recognition

At present, all TPC pattern recognition, or track finding, is done with the pad data only. The advantage of using the pad data, instead of the wire data, is that the pads provide three dimensional information with much less track overlap and confusion than the wires. There is also considerably less pad data than wire data, making pad pattern recognition faster. Conversely, the advantage of using the wire information for pattern recognition is that the density of points on a track is very high. The maximum number of pad hits on a track is 15, the maximum number of wires 183. (An ideal pattern recognition program would use both the pad and the wire data. The faster track finding program using pads only might be used to find interesting events, which, after all, are quite rare. A slower, but nearly completely efficient track finding program, even for tracks crossing only two pad rows, using both pad and wire data could then be employed.)

Three different track finding algorithms are commonly used. Which algorithms are chosen for a particular event depends on the type of data (beam or cosmic ray) and the number of pad hits. The three algorithms are called the histogram algorithm, the two point algorithm, and the three point algorithm. The histogram algorithm and the two point algorithm can only find tracks coming from the origin. The three point algorithm can find tracks anywhere.

In the three point algorithm, triplets of pad points are tested to see if they form an orbit. In the two point algorithm, one of the points chosen is the origin. The orbit of a track passing through the TPC is a helix. A set of three 3 dimensional points is sufficient to overdetermine a helix. Bad orbits can, therefore, be rejected immediately. If the orbit is good, the remaining points are then checked to see if they lie on the same curve. A track is kept if the number of good points on it exceeds the desired value, which can vary from 4 to 7 depending on the track topology. Triplets of points are chosen by selecting 3 (or 2) pad rows and testing all combinations of points in those (special) pad rows to see if they form orbits. If they do, points from other rows are checked. After all combinations using these 3 (or 2) pad rows have been tried, points from

another triplet (or pair) of pad rows are tried. To save time, not all triplets (or pairs) of pad rows are tested. Trying all sets of points from all sets of rows finds very few additional tracks, if the pad row triplets (pairs) from which the points *are* checked, are chosen correctly.

The three (and two) point algorithms are efficient and very fast if the total number of pad hits is small. This is true for events with few tracks or noise hits. If the number of pad hits does not exceed a certain value, these are the algorithms that are used. As the number of pad hits increases, however, the time required to test the three (or two) point combinations increases as a high power (≈ 10) of the number of points.

The histogram algorithm is used for large events. It works by placing pad hits into histogram bins which are designed to associate points from one track only. The points in the bin are then fit to an orbit; points which fit badly are dropped,and, if enough points remain, the orbit is called a track. Points are first divided into sectors and then histogrammed in $\sin\lambda$ where λ is the dip angle. $\sin\lambda = z/\sqrt{x^2+y^2+z^2}$. The "sagittas" in the xy plane of the points in each $\sin\lambda$ bin are then histogrammed. The sagitta is defined by selecting one point in each histogram bin as the privileged point, then fitting each other point, the privileged point, and the origin to a circle. The sagitta is that of the circle and the chord from the origin to the privileged point (see Fig. 3.9). The largest sagitta bin is chosen as the orbit road; an orbit fit is made, and bad points are rejected. At the end of the procedure, tracks and track segments from the different histograms are merged if they fit to an orbit, and duplicate tracks are rejected.

In certain cases two algorithms, for example the histogram and the two point algorithm, will be used to find tracks. Here again, after all tracks have been found, duplicate tracks are merged.

A final track cleanup is performed in all cases to eliminate poorly fitting tracks and junk tracks. The points freed up by this procedure are then tested to see if they fit on other tracks that have been previously found.

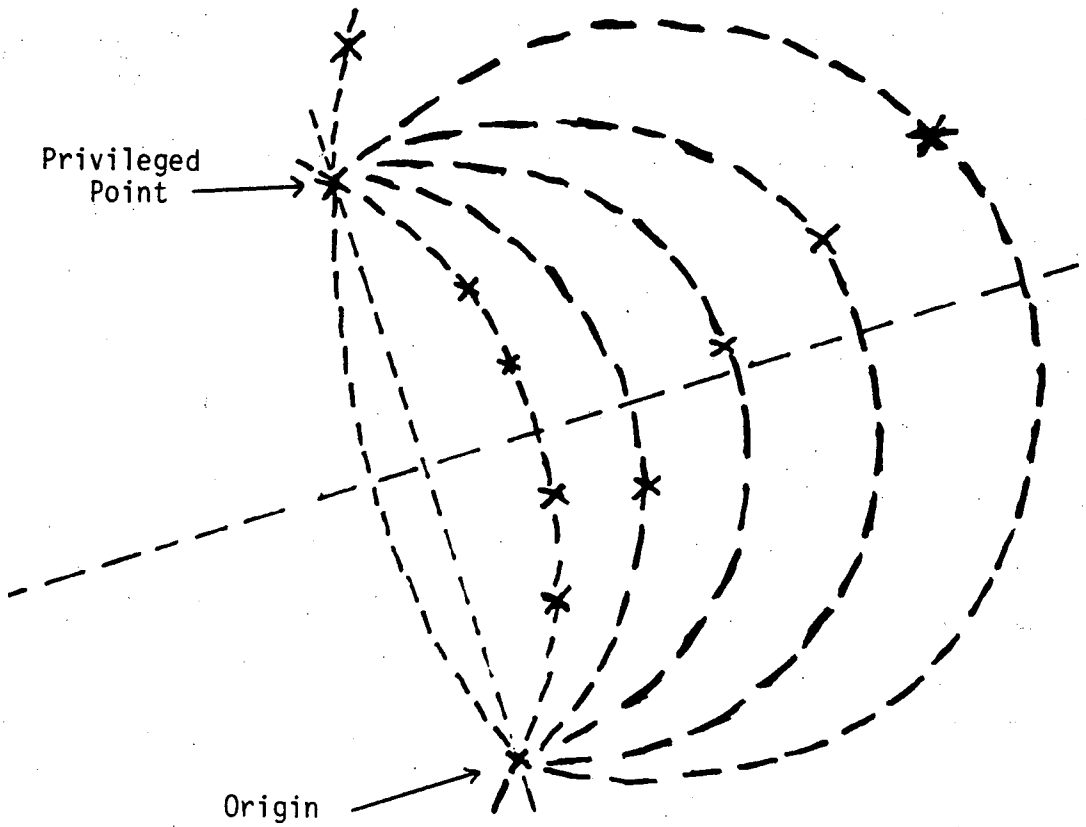

Figure 3.9. Histogram Algorithm

As determined from hand scanning, the pattern recognition efficiency for tracks crossing 3 or more pad rows in hadronic events is $(95 \pm 5)\%$.

3.3.6 TPC Wire Response

Once the tracks have been found using the pad data, the appropriate sense wires, which will be used to determine the particle's energy loss per unit length, (dE/dx), are associated with them. In order to separate the various particle species, the required accuracy for measuring dE/dx is of order 1%. Not only must the wire pulse heights be measured to 1%, but also the wire gain variations must be corrected with an accuracy of 1%, both wire to wire and along any given wire. By gain variations we mean the variations in the measured output of a channel to a given input signal. Gain variations have two sources: variations in the amplification of the electronics and variations in the gas amplification at the sense wire due to changes in the gas density or sector geometry. The resulting requirements on sector construction accuracy are extreme. A 20 micron change in the distance from the sense wire to the cathode ground plane results in a 1% change in the wire amplification [Hilke 78].

The pulse heights and z positions of the wire data clusters are determined in the same way as described previously for the pad data. A sense wire cluster is on a track if it is within ± 1 cm in z, the drift direction, of the track trajectory as determined by the fit to the pad data. If there is more than one track within ± 1 cm of the wire cluster, the cluster is labelled ambiguous. Clusters are not used in the dE/dx determination, if there is another cluster or track on the same wire within ± 3 cm in z. This ensures that each pulse height measurement will not be shifted by signal overlap in the electronics. It also reduces the interference from delta rays and eliminates ambiguous clusters. Clusters are also not used in the dE/dx analysis if the signal from a neighboring wire on the track saturates the electronics, since, in this case, an accurate cross talk correction cannot be made.

Three types of calibration are used to correct the measured pulse heights from the sense wires: an electronics calibration, a wire gain map, and an endplane source calibration.

Before each of the TPC sectors was installed at PEP, it was tested extensively in a test pressure vessel at the normal TPC pressure, gas mixture, and wire voltages. As part of that testing, a map was made of the gain variation along each wire for each sector. These maps have been shown to change very little with time, as long as the sectors are not altered mechanically [Lynch 82]. The gain variations along each wire are small, of order 3% or 4% rms. Nevertheless, they are corrected using the wire gain maps and the cluster position along each wire obtained from the track orbit.

The electronics calibration is performed with the sectors in place by pulsing a capacitor connected to the input of the sense wire preamps. The electronics calibration is used to correct nonlinearities and to measure the pedestal and saturation point of each of the 2196 sense wire channels. The channel gains and pedestals are stable at about the 1% level as shown by periodic recalibrations during data taking [Aihara 83d].

The absolute gain of each sense wire can be calibrated at PEP using any one of three remotely actuated Fe^{55} endplane sources. The sources can be turned on for calibration and off for beam data taking. The sources shine at three different points along the wires, one near the center, the others near opposite edges. The data from the three sources is used not only to measure the absolute gain of each wire, but also to determine whether a change in the variation of the gain along the wire has occurred. Such a change could occur, for example, if the temperature distribution along the wires was different in the TPC than in the test pressure vessel. This would result in the gain being systematically different on one side of the sector than the other, and lead to misidentified particles. A 0.3°C change in gas temperature at the wire results in a 1% change in the gain. The sectors are water cooled to keep the temperatures uniform. However, since heat is generated nonuniformly by the preamps on the back of the sectors, as all the sense

wire preamps are on one side, such temperature variations are possible.

In practice, the endplane source data are used to correct (up to quadratic terms) for the gain variations along wires averaged over groups of 16. The endplane source maps were extremely stable. Relative gain variations after correcting for pressure, temperature, and sector voltage changes were less than 0.3% from Jan. to June 1982 [Aihara 83f].

The wire data are corrected for changes in the gas density according to the formula:

$$PH_{dc} = PH \times \left(\frac{\rho_m}{\rho_s}\right)^{+11}. \tag{3.17}$$

ρ_m is the TPC gas density as determined from the measured values of pressure and temperature.

ρ_s is the TPC gas density at the standard operating conditions of 8.5 atm. and 23°C .

PH is the uncorrected pulse height. PH_{dc} is the pulse height after the density correction.

The coefficient, $+11$, was determined by fitting the measured changes in gas density and wire pulse height using the form given in the above formula [Hadley 82].

The wire data was corrected for changes in the sector voltages according to the formula:

$$PH_{vc} = PH \times \left(\frac{V_{sm}}{V_{s0}}\right)^{A}\left(\frac{V_{fm}}{V_{f0}}\right)^{B}. \tag{3.18}$$

V_{sm} is the measured sense wire voltage.

V_{fm} is the measured field wire voltage.

V_{s0} is the nominal sense wire voltage.

V_{f0} is the nominal field wire voltage.

PH is the wire pulse height before correction.

PH_{vc} is the wire pulse height after the correction.

The coefficients A and B were determined in tests made at the standard TPC operating conditions without magnetic field in the sector test pressure vessel. The values found were: $A = -17.8$ and $B = 1.98$. The sector voltages did not vary appreciably. This correction was typically less than 1%.

The wire data are also corrected for the effects of electron capture due to electronegative impurities in the TPC gas. For the data we will discuss, about 25% of the electrons were lost to electron capture in drifting one meter. The correction was of the form:

$$N_0 = N_m e^{\gamma L}. \tag{3.19}$$

N_0 is the original number of electrons, N_m, the measured number of electrons (signal height), L, the drift distance, and γ, the electron capture coefficient. The amount of electron capture was determined by measuring the difference in the wire pulse heights for two halves of the same track, as a function of the difference in the distances the two halves drifted to the endcap. For the spring 1982 data, the electron capture coefficient, γ, was determined frequently during the running and was found to be approximately constant with time and equal to $0.32m^{-1}$.

The wire data are also corrected for the effect of input pulse shape on the electronics output. Large dip angle tracks have slower signal risetime than tracks that are parallel to the sense wire plane. The electronics shaping is such that slower risetimes (>50 ns) give lower pulse outputs. The form of this correction is:

$$PH_{rc} = PH \times (1 + .028 \tan^2 \lambda). \tag{3.20}$$

λ is the dip angle as defined before, and the coefficient, .028, was determined theoretically from the electronics circuitry.

Because of the large electrostatic distortions at the inner radius of the TPC, the signals on the innermost 5 wires in each sector were often missing from the track information, despite

the greater than 99% efficiency observed elsewhere in the sectors. The information from these wires was judged to be unreliable and was not used in the analysis.

Chapter 4

Particle Identification by dE/dx

Particle identification by energy loss measurement is possible because particles deposit energy in the form of ionization in a gas according to their velocity, while bending in a magnetic field according to their momentum. By measuring the particle's momentum and its ionization energy loss, and thus its velocity, we can determine the particle's mass or identity.

Curves of ionization energy loss per unit length, average dE/dx, as a function of momentum are given in figure 4.1 for the five longest lived charged particles: pions, kaons, muons, electrons, and protons. The values of dE/dx at first fall as $1/\beta^2$ with increasing momentum, since as the particle's velocity increases, it spends less time in the electric field of atoms with which it is colliding and transfers less energy to them. dE/dx then rises as the momentum increases due to the relativistic increase in the particle's transverse electric field. This velocity or momentum region is known as the relativistic rise region. Finally, the value of dE/dx reaches a plateau at the highest momenta, due to polarization of the medium which the particle is traversing, canceling the effects of further relativistic increases in the particle's transverse electric field. Since electrons are very light, their velocities are sufficiently high that their dE/dx has already reached the plateau value and shows little rise over the range of momenta in Fig. 4.1 .

As can be seen from figure 4.1, in the relativistic rise region the dE/dx values of the different particle types are separated by about 10%. In order to have good particle separation

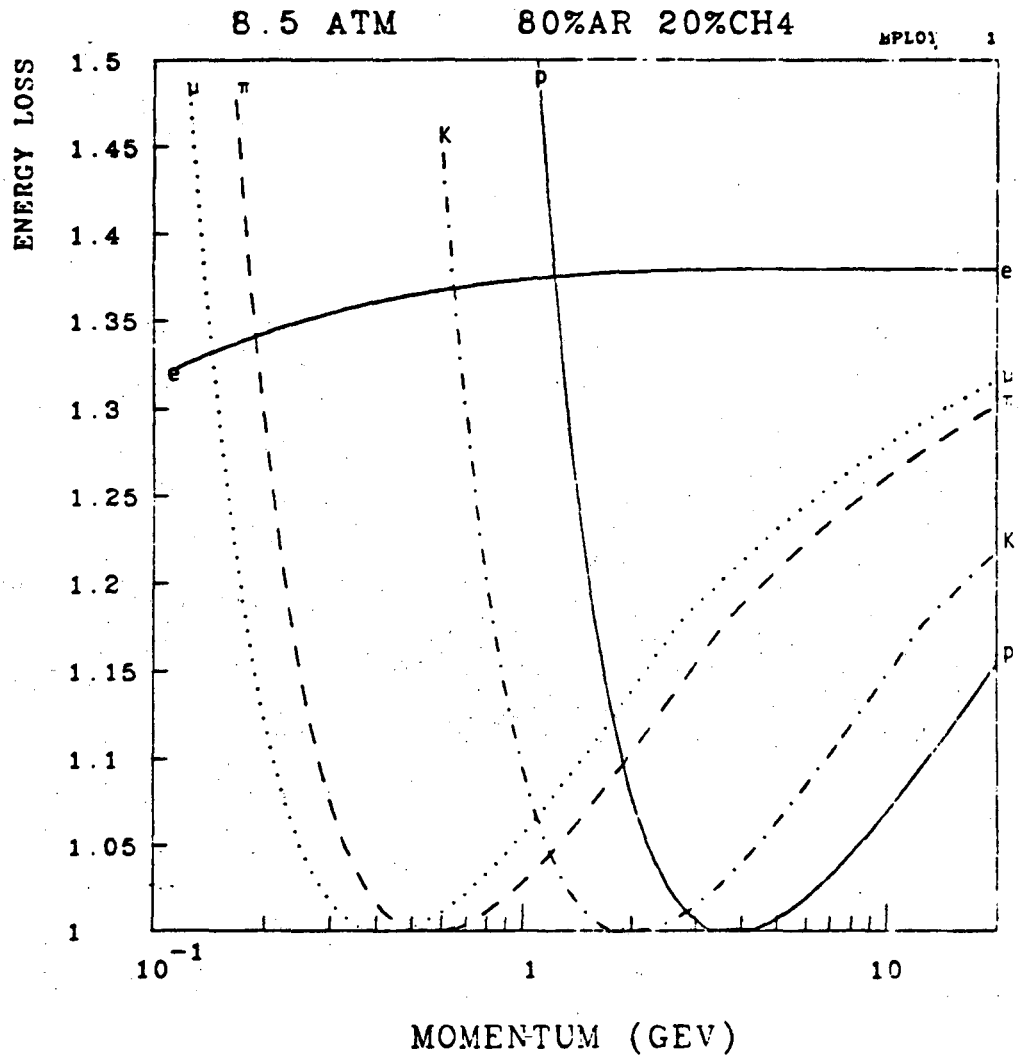

Figure 4.1

dE/dx *vs.* Momentum: π, K, p, e, μ.

The curves have been normalized to the minimum value of dE/dx.

in this region, it is necessary to measure dE/dx with an accuracy of about 2% or 3%. This, of course, is why all the effort was made to measure and understand the response of the TPC sector sense wires at the 1% level.

So far, we have loosely discussed energy loss, ionization energy loss and wire pulse height without distinguishing them. A charged particle's energy loss in the gas is converted to wire pulse height as follows. The particle passes through the gas leaving behind a trail of positive ions and electrons. The number of ionization electrons is proportional, with some fluctuation, to the amount of energy loss. Typically, a minimum ionizing particle loses about 6 KeV of energy every 4 mm, which is the sense wire spacing, in the standard TPC gas leading to about 200 ionization electrons. These electrons then drift in the electric field to the endplane sectors. During the drift, they diffuse and some of them are lost to electron capture by impurities. When they arrive in the vicinity of the sense wires, the electrons are accelerated by the strong electric field near the wires, and each electron then produces about 1000 additional ionizations at the sense wire. The fluctuations in the number of electrons produced in this step are called avalanche fluctuations. The raw signal at each sense wire is then amplified by the TPC electronics. The height of the output signal is the sense wire pulse height, which is then corrected as described in the previous chapter.

A histogram of the corrected wire pulse heights divided by the path length between the wires for many minimum ionizing muons is given in figure 4.2. The pulse height distribution is broad (FWHM$\approx$55%) with a long high energy Landau tail caused by hard collisions. Because of this long tail, the mean of the distribution, which is strongly affected by the few events in the tail, is not a useful quantity. Instead, we will characterize the energy loss per unit length of the particle, dE/dx, by the mean of the lowest 65% of the wire pulse heights, the 65% truncated mean. By measuring the pulse height often, we can determine the dE/dx for the particle to the desired accuracy despite the large width of the distribution. This large width is the result of both

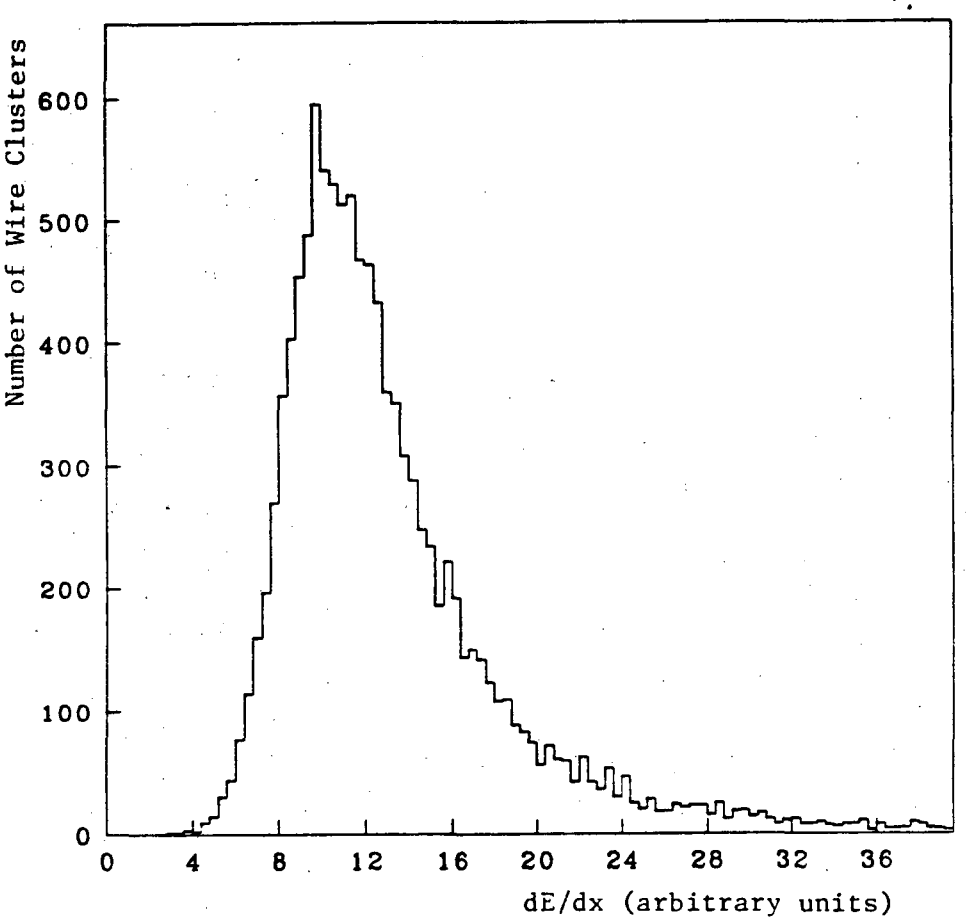

Figure 4.2. Landau Distribution — Minimum Ionizing Muons

the fluctuations in the initial energy loss and ionization process, the dominant contribution, and the avalanche fluctuations. Typical wire thresholds are at about 2 in the units of figure 4.2. As can be seen from the figure, low pulse height contamination and threshold bias are not a problem for the truncated mean measurement.

4.1 dE/dx Resolution

We have determined the TPC dE/dx resolution in two different ways. The first involves comparing the dE/dx from a track with dE/dx information from the same track, for example, measuring the difference in dE/dx from a single cosmic ray as measured in two sectors. The second involves measuring dE/dx from different tracks selected to have the same theoretical value of dE/dx, for example, Bhabha electrons. We would expect comparing a track with itself to yield better values for the resolution, since when we make the comparison many systematic effects will cancel. Examples of such systematic effects are gain variations due to changes in temperature or pressure and gain variations due to changes in dip angle.

Figure 4.3 shows a histogram of the difference in dE/dx as measured by two sectors for single cosmic rays. More precisely, the histogrammed quantity is:

$$\frac{\frac{dE}{dx}(A) - \frac{dE}{dx}(B)}{\frac{1}{2}\left(\frac{dE}{dx}(A) + \frac{dE}{dx}(B)\right)}. \tag{4.1}$$

$dE/dx(A)$ is the 65% truncated mean as measured in sector A.

$dE/dx(B)$ is the 65% truncated mean as measured in sector B.

The events were selected by requiring that only one track be found in each of two sectors, that more than 120 wires be found on the track in each sector, that the measured momenta be greater than 1.2 GeV, and that the tracks be approximately colinear. Figure 4.3 shows a typical distribution in that the non-gaussian tails are small. The TPC resolution is given by the standard

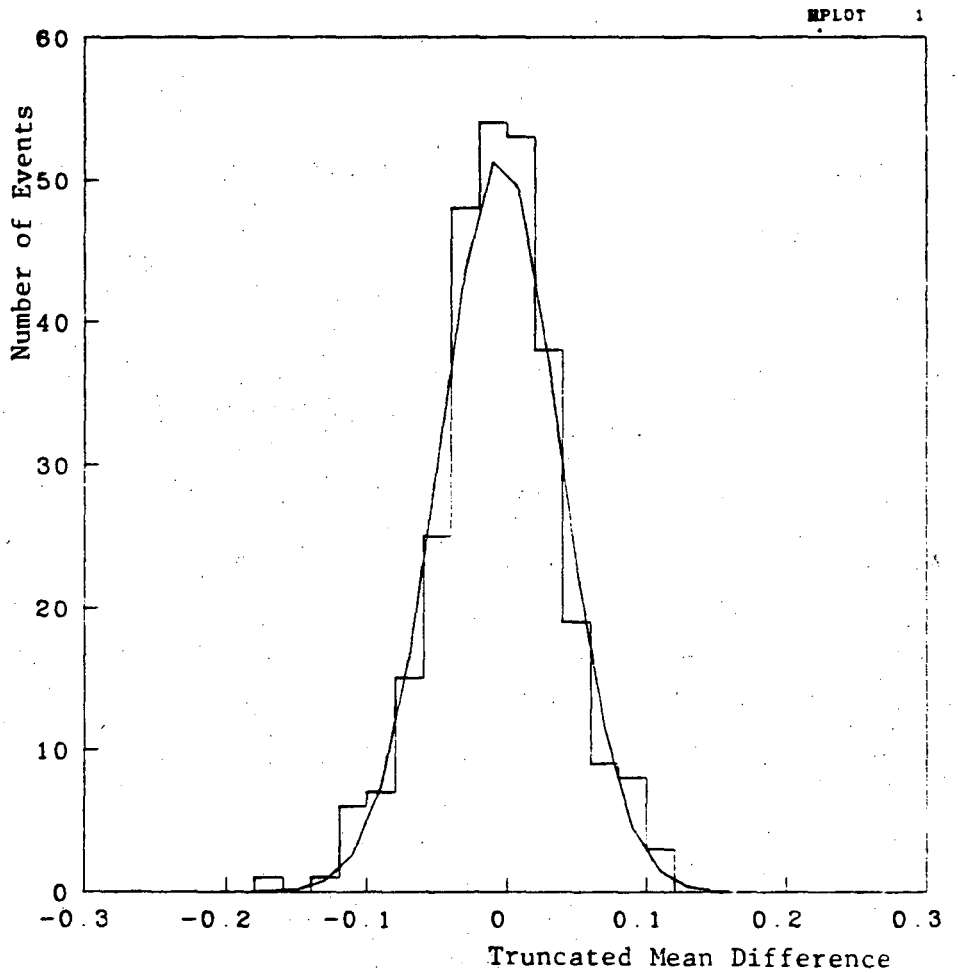

Figure 4.9. dE/dx Difference — Cosmic Rays

deviation of the distribution defined in equation 4.1 divided by $\sqrt{2}$. Averaged over many runs, the dE/dx resolution as measured in this manner at 8.5 atm. was:

$$\sigma = (3.0 \pm 0.1)\%. \tag{4.2}$$

The quoted error contains an estimate of both the systematic and statistical errors. The possible sources of systematic errors will be discussed in the sections on the measurement of the relativistic rise. The value for the dE/dx resolution obtained by comparing dE/dx from two halves of a track as measured in a single sector was the same as the above result when corrected for the difference in the number of wires used in the measurement.

Figure 4.4 shows a scatter plot of dE/dx *vs.* momentum for cosmic ray muon data obtained during beam data taking in May 1982. The events selected for the plot have less than three tracks. Tracks selected for the plot were required to have more than 120 good wires, where good wires are those that pass the cuts discussed in section 3.3.6 . Tracks below 1 GeV/c were required to have dE/dx less than 14 in the (arbitrary) units used in the plot in order to reject low energy electrons. We define minimum ionizing muons as those with momentum between .37 GeV and .61 GeV. The dE/dx distribution for minimum ionizing muons is shown in figure 4.5 . The TPC dE/dx resolution as obtained from the standard deviation of the gaussian fit to the distribution is:

$$\sigma = (4.2 \pm 0.2)\%. \tag{4.3}$$

Figure 4.6 shows a scatter plot of dE/dx *vs.* momentum for the multihadron events obtained during May-June 1982. The electron, pion, kaon, and proton bands are clearly visible. Once again, accepted tracks have a minimum of 120 wires. We select minimum ionizing pions as those between .45 GeV/c and .74 GeV/c. The TPC dE/dx resolution for minimum ionizing pions in multihadron events as determined by the standard deviation of the gaussian fit to dE/dx

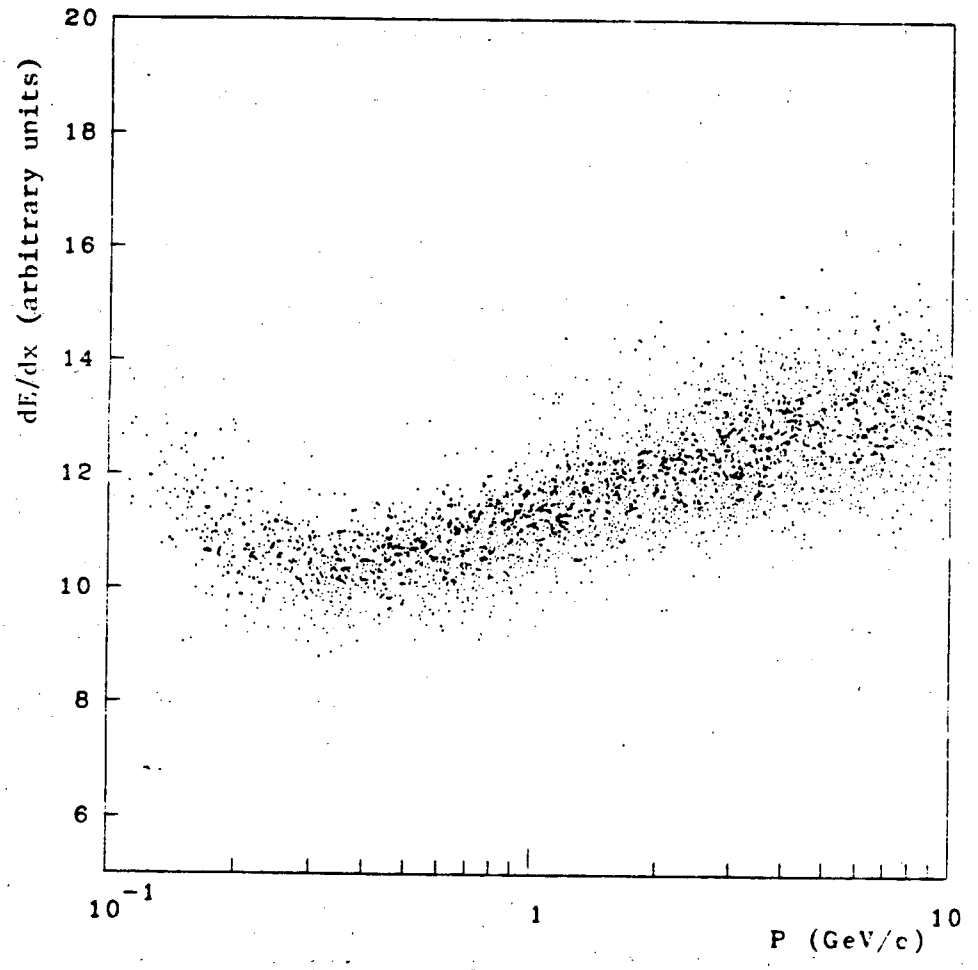

Figure 4.4. dE/dx *vs.* Momentum — Cosmic Ray Muons

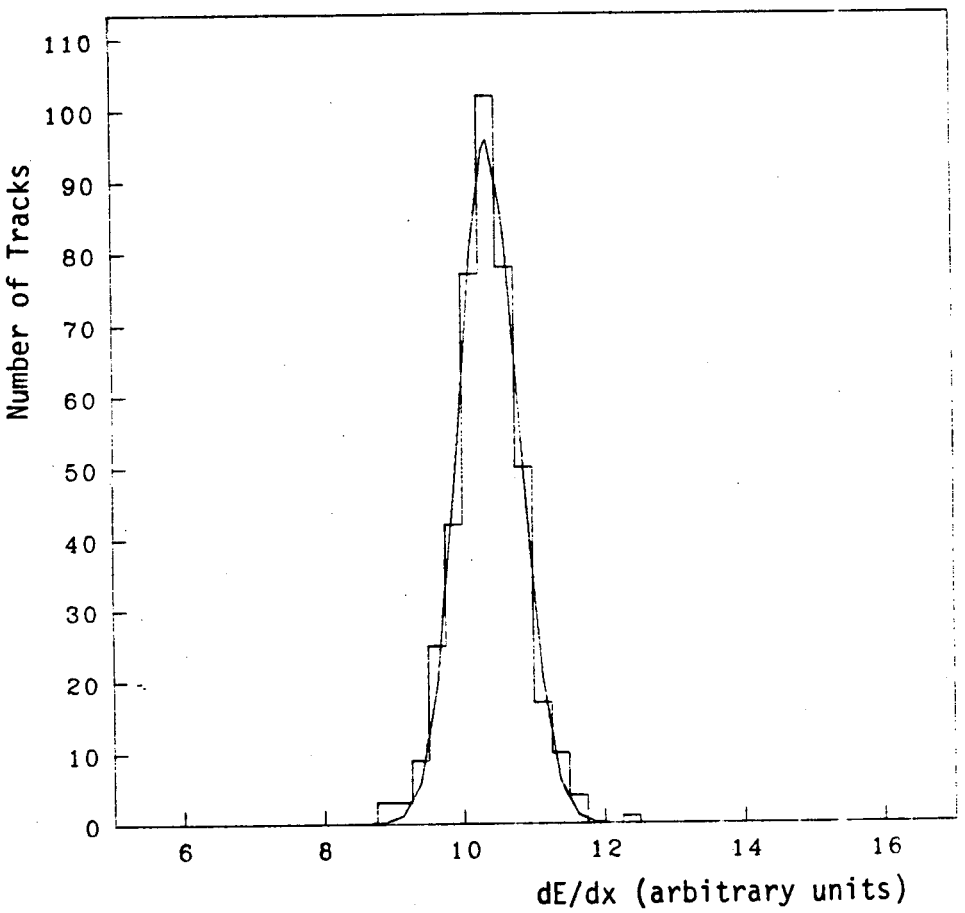

Figure 4.5. dE/dx Distribution — Minimum Ionizing Muons

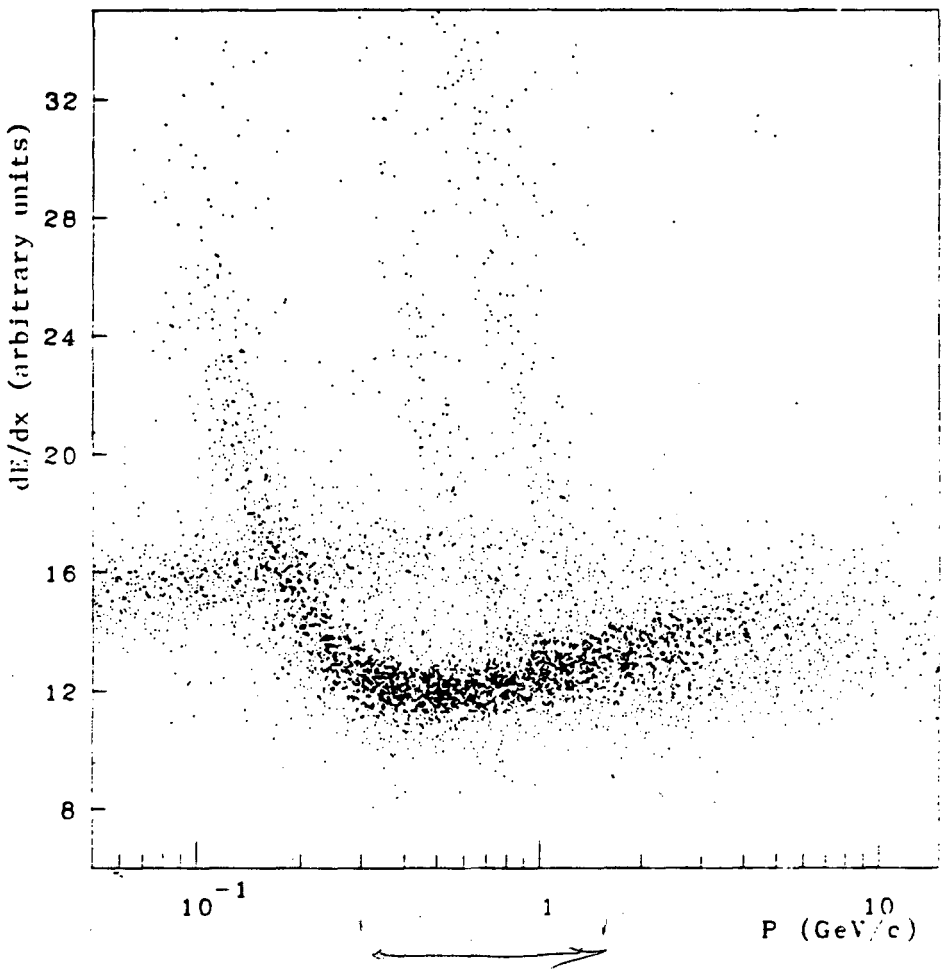

Figure 4.6. dE/dx *vs.* Momentum — Multihadron Events

distribution of the pions is:

$$\sigma = (4.1 \pm 0.1)\%. \tag{4.4}$$

Wide angle Bhabha candidate events (e^+e^-) were selected by requiring a shower with greater than 5 GeV of energy in one of the hexagonal calorimeter modules plus no more than two tracks in the TPC. Bhabha electrons were selected from those events by requiring that they come from the vertex and have momentum between 2.7 GeV/c and 20 GeV/c. The TPC dE/dx resolution for Bhabha electrons with more than 120 good wires on each track was found to be:

$$\sigma = (3.4 \pm 0.3)\%. \tag{4.5}$$

The error is larger because of the smaller number of events and larger non-gaussian tails in the distribution (see Fig. 4.7).

The measured truncated means for the multihadron data and the Bhabha data were corrected for the effect that a particle's energy loss does not vary linearly with distance, x, but varies as $x \ln x$ [Landau 44]. dE/dx then varies as $\ln x$, where x is the distance over which the track is sampled. This increase in dE/dx with distance is caused by the increased number of hard collisions from the Landau tail of the energy loss distribution that contribute as the sampling distance increases. The correction used had the form:

$$\left(\frac{dE}{dx}\right)_{corrected} = \frac{dE}{dx} - .9 \ln x. \tag{4.6}$$

with x in centimeters.

The coefficient .9 was determined from a fit to the variation of dE/dx with $\ln x$ for minimum ionizing pions from the multihadron sample. This correction improved the measured dE/dx resolution by 0.2% to 0.3%.

The values of dE/dx for both the Bhabha data and the multihadron data were also corrected for the remaining gain variations with time after all other corrections had been done.

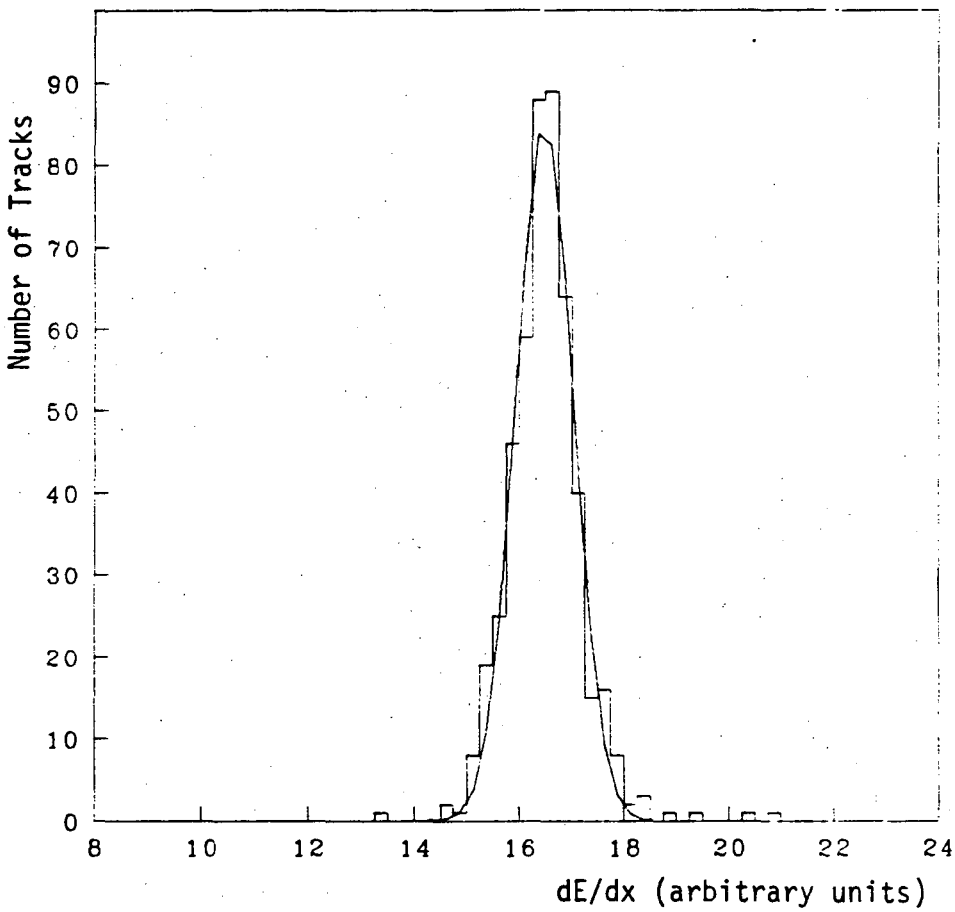

Figure 4.7. dE/dx Distribution — Bhabha Electrons

The experimental data from May-June 1982 was divided into 800 runs as the data was taken. The average gain was found for the 40 twenty run groups from the value of dE/dx for minimum ionizing pions. A correction factor was then applied to make the gain of each 20 run group the same. These correction factors were typically of order 1% or 2%. The cause of the remaining variations in sector gain after the density, voltage, and electron capture corrections had been applied is unknown. Part of the gain variations could be explained by changes in the amount of electron capture which was taken to be constant for all runs. Another possible cause is the variation in the composition of the TPC gas. During tests made with individual sectors before the apparatus was finally assembled, it was found that a 0.2% fractional change in the amount of methane in the TPC gas causes a 1% change in the wire gain. The amount of methane in the TPC gas was not measured accurately enough to determine whether such small changes in the gas composition had taken place. Other, unknown, gas impurities could also have caused the gain changes. The run by run gain corrections were not applied to the cosmic ray data because those data were analyzed on a single run basis only, where a single run lasted $\approx$ 1 hour. The measured resolutions for a number of runs were then averaged to obtain the given value. Even if we allow for an improvement in the resolution from the ln length correction, the dE/dx resolution as measured from the cosmic ray data where there is normally only one track per sector is not better than that measured in the multihadron events for pions at minimum. The cuts made to avoid pulse-height shifts caused by the effects of overlapping tracks were, therefore, effective. (The cuts are described in section 3.3.6 .)

The better resolution for Bhabha electrons is most probably due to the larger value of dE/dx for Bhabha electrons on the plateau compared with minimum ionizing particles. If the amount of noise is constant, then the resolution (noise/signal) improves if the signal becomes larger. The electronic noise and some errors in the electronic calibration are independent of signal size, leading to the observed improved resolution for Bhabha electrons.

4.2 Relativistic Rise

The total amount of relativistic rise, the difference between dE/dx on the plateau and at minimum, was determined for the standard TPC operating conditions using the Bhabha events and minimum ionizing pions from the multihadron events. Both sets of events came from the same data tapes obtained during the same time period (May-June 1982). This ensured that many systematic effects would be the same for both samples. The events were all analyzed with the same versions of the data analysis programs. The minimum ionizing pions and Bhabha electrons were selected in the way described previously. The value for the total relativistic rise defined as the ratio of dE/dx for Bhabha electrons to dE/dx for the minimum ionizing pions was:

$$\text{Total Relativistic Rise} \equiv \frac{\frac{dE}{dx}(Bhabha)}{\frac{dE}{dx}(Minimum)} = 1.38 \pm .02. \tag{4.7}$$

The error, .02, contains both the statistical error (.004) and the estimated systematic error.

One of the largest sources of possible systematic error is the electronics calibration, since the system used until the summer of 1982 to pulse the electronics and make the calibration was known to be of poor quality. The pulse shapes produced by the system were not uniform and pulse risetimes varied with amplitude. The pulse risetimes were too slow, so that these variations affected the response of the TPC electronics. In consequence, more time was probably spent calibrating the pulser system than in calibrating the TPC electronics. The pulser system was changed during the summer of 1982, and a new and much improved system installed. Since the TPC wire electronics were not changed during the summer of 1982, it was possible to determine the total relativistic rise using calibrations made with both the old (Spring 1982) and new (Fall 1982) pulser systems. The results were:

$$\text{Total Relativistic Rise (old pulser calibration)} = 1.381 \pm .004 \tag{4.8}$$

$$\text{Total Relativistic Rise (new pulser calibration)} = 1.383 \pm .009 \tag{4.9}$$

The quoted errors are statistical only. Both results agree within errors, indicating that both calibrations are reliable, even that made with the old pulser system. The remaining sources of systematic error, which are common to both pulser systems, are changes in the gas composition and errors in the electronics calibration. For example, the electronic pedestals were measured in the same way for both calibrations, although at different times.

In order to identify particles by dE/dx, it is important to measure the shape of the relativistic rise as well as the total rise. Cosmic ray muons were used to study the shape of the relativistic rise, as they provide a source of particles of known type with different momenta. As a quantity to characterize the shape of the relativistic rise, we choose to measure the equivalent difference in dE/dx of 3.5 GeV/c pions and kaons using the cosmic ray muons. The velocity of a 2.65 GeV/c muon and, therefore, its dE/dx, are the same as that of a 3.5 GeV/c pion. Similarly, the velocity of a 0.75 GeV/c muon is the same as that of a 3.5 GeV/c kaon. To characterize the difference in dE/dx for a 3.5 GeV/c pion and kaon we then measure:

$$D_{\pi K} \equiv \frac{\frac{dE}{dx}(2.65 \text{ GeV/c muon}) - \frac{dE}{dx}(0.75 \text{ GeV/c muon})}{\frac{dE}{dx}(\text{Minimum})}. \tag{4.10}$$

At the standard TPC operating conditions (8.5 atm., 80% Ar. 20% CH_4), we measure using cosmic ray data taken during the May-June 1982 data run:

$$D_{\pi K} = .146 \pm .008. \tag{4.11}$$

The quoted error is a combination of both the statistical and systematic errors. As with the total relativistic rise, the calculation of the equivalent 3.5 GeV/c π-K difference was made with calibrations from both the old (Spring 1982) and new (Fall 1982) pulser systems. The results from the calculations using the two calibrations were equal within errors. However, the quoted result, $.146 \pm .008$, disagrees with an earlier result obtained from data taken in November 1981 at 8.64 atm. of $.121 \pm .005$ [Lynch 82] .

The earlier results are from data taken at three pressures. They and the later values obtained at 8.5 atm. and 1.0 atm. are listed in table 4.1 . Theoretical calculations of the measured quantity obtained from an empirical fit to other energy loss data by A.Walenta [Walenta 81] and from a theoretical model by G.Lynch [Lynch 81] are also given in the table. (The model of G.Lynch only discusses argon. It was extended to argon methane by the author.)

P [atm]	Data Set	$(D_{\pi K})_{exp}$	$(D_{\pi K})_{calc}$ Lynch Model	$(D_{\pi K})_{calc}$ Walenta Model
8.64	Fall 81	$.123 \pm .003$	.117	.146
8.50	Spring 82	$.146 \pm .003$	.118	.146
4.02	Fall 81	$.151 \pm .005$	.139	.163
1.50	Fall 81	$.176 \pm .009$	.172	.190
1.00	Spring 82	$.184 \pm .003$	.184	.203

Table 4.1. π–K dE/dx Difference at 3.5 GeV

The errors quoted in table 4.1 are statistical only.

The difference between the measured values obtained in Fall 1981 and those from Spring 1982 is too large to be explained by the difference in the pressures at which the two measurements were made. The difference is also too large to be accounted for by the difference in the methane fraction. Using either the model of G.Lynch or Walenta's fit to other data, we calculate that a change in methane fraction from 20% to 0% would only account for 1/2 of the observed shift. Such a change can be ruled out, since it would have resulted in unstable operation of the sectors and a reduction of a factor of 4 in the drift velocity, neither of which was observed. A change in the drift velocity from 4.64 $cm/\mu s$ to 4.95 $cm/\mu s$ was observed from the Fall 1981 data to the Spring 1982 data. However, given the pressure change, such a change in drift velocity is consistent with a change in the methane fraction from 20% to 16%, which would only account for 15% of the observed shift in the amount of relativistic rise. The most likely remaining explanation is that the electronics calibration used for the Fall 1981 data was incorrect. This calibration was

made using the same unreliable pulser system as was used for the Spring 1982 calibration, but a different technique was used for measuring the response of the pulser system. Unfortunately, the wire electronics were changed between Fall 1981 and Spring 1982 making it impossible to analyze both sets of data using the same calibration. The Spring 1982 measurement is considered more accurate than the Fall 1981 measurement, since the same value for the relativistic rise was obtained using different calibrations from different pulser systems, and since it agrees with measurements of the relativistic rise made using the Fall 1982 data. Nevertheless, we have assigned a large systematic error to the measurement of the rise, since it varied widely from Fall 1981 to Spring 1982.

We note that the 8.5 atm., Spring 1982 values are in good agreement with Walenta's model which is based on a fit to the data from earlier experiments for various pressures and gas mixtures. The G.Lynch model predicts a relativistic rise smaller than that measured at 8.5 atm., but agrees with the 1 atm. measurements.

Cosmic rays were the main source of background triggers during the May-June 1982 data taking. We were, therefore, able to monitor the relativistic rise on a run by run basis during that period using the same data tapes from which the multihadron events were selected. The value of the equivalent 3.5 GeV/c $\pi - K$ difference in dE/dx was found to be constant during the running.

Figure 4.8 shows a fit to the cosmic ray data based on a model for both the most probable energy loss and the shape of the dE/dx distribution by O.Dahl [Dahl 79]. The expected value for the 65% truncated mean was calculated from the model, and the values of various parameters in the model were varied to fit the total relativistic rise and the data shown in figure 4.8. As can be seen, the fitted curve describes the data well. (The curve will be used later in the calculation of the particle ratios in the relativistic rise region.)

The results for the total relativistic rise and for $D_{\pi K}$ are in good agreement with

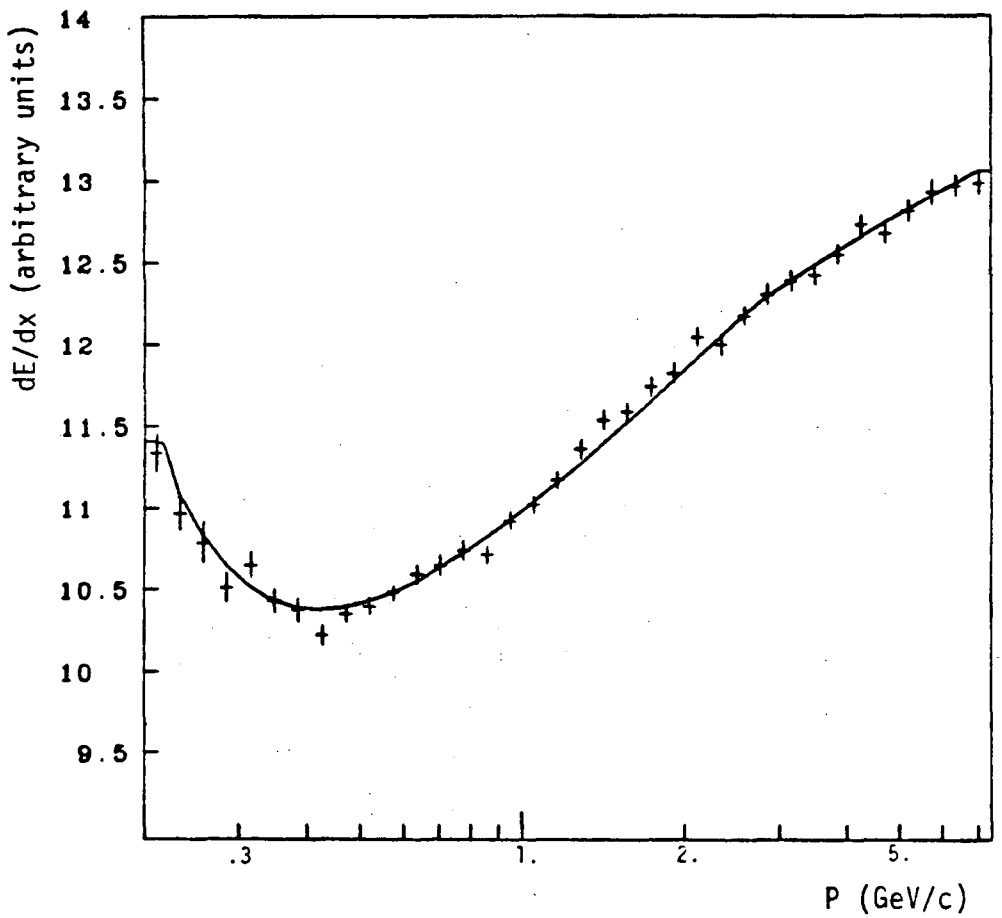

Figure 4.8. dE/dx *vs.* Momentum — Fit to Muon Data

the value for the ratio of dE/dx of 800 MeV/c pions and electrons made with the dipole TPC prototype at the Bevatron after correction for the pressure difference. The dipole TPC measurements were made at 10 atm. in 80% argon and 20% methane. The results were [Fancher 79]:

$$\frac{\frac{dE}{dx}(800 \text{ MeV/c electron})}{\frac{dE}{dx}(800 \text{ MeV/c pion})} = 1.35 \pm .02. \tag{4.12}$$

Using the fit to the May-June 1982 muon data, corrected for the pressure difference, we would predict $1.36 \pm .02$ for the same number. The pressure correction has been taken from the model of G.Lynch . Walenta's model gives the same result for the correction. The error $\pm .02$ was set equal to that for the May-June 1982 measurement of the total relativistic rise.

4.3 Standard Operating Conditions

The standard TPC operating conditions, 80% argon 20% methane, 8.5 atm., drift electric field, E, $= 75\ kV/m$, were chosen for a variety of reasons. Argon methane gas was chosen because it has a fast drift velocity and low diffusion, and provides for good particle separation and stable chamber operation. The value for the drift electric field was determined by the maximum safe operating voltage (75KV) for the TPC high voltage system at 8.5 atm. Since replacing this system would take a long time (more than 1 year) and since the TPC could not function without it, 75 KV was chosen even though the system was designed to operate at 200 KV. This restriction made the TPC drift velocity more sensitive to changes in pressure, temperature, and high voltage, since instead of operating at the maximum of the drift velocity *vs. E/density* curve, the TPC operated on the steeply rising, low *E/density* part of the curve. 8.5 atm. was the highest pressure at which the poletip calorimeter wire chambers could operate.

High pressure was chosen because it improves the spatial resolution by decreasing diffusion and because it gives slightly better particle separation in the relativistic rise region (see

table 4.2). The improved resolution with pressure compensates for the decreased relativistic rise. As a measure of the particle separation in the relativistic rise region, we define the equivalent $\pi - K$ separation at 3.5 GeV/c using cosmic ray muons to be:

$$S_{\pi K} \equiv \frac{\frac{dE}{dx}(2.65 \text{ GeV/c muon}) - \frac{dE}{dx}(0.75 \text{ GeV/c muon})}{\sigma_{minimum}}. \tag{4.13}$$

Older theories of dE/dx [Sternheimer 71] did not predict that the relativistic rise would decrease as rapidly with pressure. This led to early, unrealistic expectations for TPC performance at high pressure.

P [atm]	Data Set	$(S_{\pi K})_{exp}$	σ_{xy} [microns]
8.64	Fall 81	$3.15 \pm .19$	260
8.50	Spring 82	$3.56 \pm .11$	195
4.02	Fall 81	$3.05 \pm .13$	299
1.50	Fall 81	$2.75 \pm .19$	439

Table 4.2. π–K Separation and Spatial Resolution *vs.* P

(Note for table 4.2: Much more work was done analyzing the Spring 1982 data than the Fall 1981 data. The resolutions obtained for the spring data were, therefore, better. The values for the relativistic rise, $D_{\pi K}$, were different for the two data sets, with the Fall 1981 values being less reliable. The Fall 1981 data is still useful, however, for examining the changes in resolution with pressure.)

Chapter 5

Total Cross Section Measurement

In this chapter we will discuss a measurement of the total cross section for e^+e^- annihilation into hadrons at $\sqrt{s} = 29$ GeV. We will obtain the ratio, R, where:

$$R \equiv \frac{\sigma(e^+e^- \rightarrow \text{hadrons})}{\sigma(e^+e^- \rightarrow \mu^+\mu^-)} \tag{5.1}$$

by comparing the measured hadronic cross section with the calculated cross section for the process $e^+e^- \rightarrow \mu^+\mu^-$. We will use the value of the total cross section to normalize the differential cross sections for the different particle species that we will obtain in the next chapter. The ratio, R, is perhaps the most fundamental quantity whose value is predicted by the quark-parton model. We will also discuss measurements of the average charge multiplicities of the hadronic events as well as measurements of various quantities characterizing event topologies. The results are in agreement with the model for e^+e^- annihilation into hadrons through quarks and gluons that was presented earlier. First, however, we will describe the trigger that was used in taking the data and the hadronic event selection.

5.1 Trigger

The PEP-4 trigger has two levels: a pretrigger, which is fast enough to make a decision

between beam crossings, and a slower trigger, which looks only at those events that have satisfied the pretrigger.

The charged particle pretrigger consisted of a logical OR of two elements, one an outer drift chamber pretrigger, and the other a pretrigger based on the first 1 μs of information from the TPC wires (the TPC Fast pretrigger). The outer drift chamber pretrigger required two tracks in the drift chamber separated by more than roughly 30° in ϕ, the azimuthal angle. The TPC Fast pretrigger required that the signals from a majority of wires out of a given group of 8 (a majority signal) exceed a preset threshold within the first 1 μs after beam crossing. At least two such majority coincidences, separated by more than roughly 90° in ϕ if the tracks were in the same endcap, were required. A pretrigger could also be generated by the coincidence of one ODC track and one TPC majority unit. The outer drift chamber pretrigger covered the range in polar angle, θ, from 40° to 140°. The TPC Fast pretrigger covered the ranges in θ from 30° to 40° and from 140° to 150°. The neutral energy pretriggers consisted of a poletip calorimeter back to back pretrigger, a hexagonal calorimeter total energy petrigger, and a poletip calorimeter total energy pretrigger. The normal pretrigger rate was 0.5 to 1 KHz.

The charged particle trigger relied on the TPC wire information only. The trigger used the timing information from the wires to require that a track point towards the origin, or "ripple". A "ripple" trigger would be started by the majority signal from a group of wires near the outer radius. The next group of wires, adjacent to the first and closer to the inner radius, would then be required to have a signal coming in coincidence with or just after the first signal. If this coincidence occurred, the process would be repeated with the third set of wires, one closer to the inner radius than the second, and so on to the inner radius. If the chain was broken for more than two sets of wires, the ripple requirement was not satisfied. The timing information was sufficiently accurate that tracks coming from within about ± 25 cm from the origin in z, the drift direction, could be selected. For the charged particle trigger to be satisfied, two rippling

tracks were required. The tracks could either be in different endcaps or separated by more than about 30^o in azimuth (ϕ) if they were in the same endcap. In addition to the charged particle trigger, there were also neutral energy triggers based on the calorimeter data that corresponded to the previously described pretriggers. (For a more detailed description of the trigger, see Ronan 82.)

It was later discovered, in Fall 1982, that there was an inefficiency in the charged particle trigger between 45^o and 50^o and between 135^o and 140^o in θ, the polar angle. This inefficiency was caused by the ripple timing window being slightly out of time in the region where the pretrigger was changing from outer drift chamber to TPC Fast. The ripple timing window determines the time in which the majority signal from a group of wires must arrive for the ripple requirement to be satisfied. This inefficiency causes only a slight problem for the data we will discuss, since the multihadron events were required to have at least 5 tracks, and the probability of having four or more tracks be in the inefficient region is small. From the Monte Carlo, the trigger efficiency for the event selection criteria given in section 5.2 was $(99.3 \pm 0.4)\%$. We will also discuss a determination of the total integrated luminosity based on results from Bhabha events. Bhabha events were obtained solely from the poletip calorimeter information, and were, therefore, independent of the charged particle trigger.

5.2 Event Selection

The goal of event selection is simple: to obtain as pure a sample of the desired type of event as possible, while, at the same time, obtaining as many of them as possible. In our case, the desired events were hadronic events from e^+e^- annihilation. The principal background events were: $\tau\overline{\tau}$ events, beam gas events, two photon events, and showering cosmic ray events. Here, two photon events are events in which the electron and positron annihilate into hadrons through the production of two virtual photons.

The selection criteria were based on charged particles only. They were that:

1. Number of charged tracks be greater than or equal to 5.

A charged track was required to have momentum greater than 100 MeV/c and to come from within ± 5 cm of the origin in the xy plane, the plane perpendicular to the beam axis, and to come within ± 10 cm of the origin in z, the direction along the beam axis. This cut eliminated all low multiplicity events such as Bhabha events, muon pairs, cosmic rays, and low multiplicity tau events and two photon events. The requirement that the tracks pass close to the origin eliminates cosmic ray and beam gas events that do not occur close to the beam interaction point.

2. The sum of visible momenta $\equiv \sum|P| \geq 7.25 GeV/c$.

7.25 GeV/c equals one half of the beam energy. To deal with badly measured tracks whose measured momentum could be greater than the beam energy, the quantity P_c was used instead of P.

$$P_c \equiv \frac{1}{\sqrt{K^2 + 2\sigma_K^2}}. \tag{5.2}$$

K and σ_K are the measured curvature and curvature error. P_c is normally distributed about the true value of P.

This cut primarily excludes two photon events, where most of the energy in the events usually remains with the electron and positron, which stay close to the beam pipe and are not detected.

3. The sum of the momenta in the z direction divided by the visible momentum be less than or equal to .4 . That is:

$$\frac{\sum P_z}{\sum|P|} \leq .4 \tag{5.3}$$

with P as defined in criterion 2.

This cut is equivalent to requiring the β of the hadronic center of mass to be less than .4 . It eliminates two photon events, which tend to have tracks only in one hemisphere. It also eliminates beam gas events and beam pipe events where all the particles tend to be travelling in one direction after one of the beam particles has struck one of the residual gas molecules in the beam pipe or the wall of the pipe itself.

5.3 Detection Efficiency

The detection efficiency was determined by creating simulated (Monte Carlo) events for e^+e^- annihilation, passing them through a detailed detector simulation, fitting the generated space points, and then applying the same cuts, described in the previous section, that were used to select the data events.

The LUND generator [Andersson 78] was used to create the simulated hadronic events. This generator has been extensively used by many groups doing e^+e^-, and other, experiments. (We are grateful to the LUND group for sending us the FORTRAN programs used in their Monte Carlo.) The generator uses a string model and employs a recursive scheme for particle generation similar to that described in chapter 2. It includes three-jet, $q\bar{q}g$, events and four-jet, $q\bar{q}gg$, events. The parameters in the model have been tuned to provide a good fit to event multiplicities and to general event topologies as a function of energy.

The original LUND generator employed fragmentation functions that decrease as $z \rightarrow 1$, where the fragmentation function, $D(z)$, gives the probability for a hadron of fractional momentum, $z = P_{hadron}/P_{quark}$, to be produced by a given quark. The fragmentation functions for the charm and bottom quarks were modified, following the form used by the Mark II group [Yelton 82], to be:

$$D(z) = \frac{\text{constant}}{z(1 - \frac{1}{z} - \frac{\epsilon}{1-z})^2}. \tag{5.4}$$

ϵ_{charm} was set equal to .25 and ϵ_{bottom} equal to .04 to be consistent with measurements showing the fragmentation functions for these quarks to be peaked towards $z = 1$ [Nelson 82].

$q\bar{q}g$ events are generated in the LUND model according to the standard cross section

$$\frac{d\sigma_{q\bar{q}g}}{dx_1 dx_2} = \sigma_0 \frac{\alpha_s(Q^2)}{\pi} \frac{2}{3} \frac{x_1^2 + x_2^2}{(1-x_1)(1-x_2)} + \text{terms of order } M_q^2/W^2. \tag{5.5}$$

Here, $x_1 \equiv 2E_q/W$, $x_2 \equiv 2E_{\bar{q}}/W$, and $W \equiv \sqrt{s} \equiv$ center of mass energy.

M_q is the quark mass.

This cross section diverges as either x_1 or x_2 approaches 1. Theoretically, this divergence disappears when the vertex and propagator corrections are included. This divergence is handled in most models by using a cutoff for the values of x_1 and x_2. Physically, this is sensible since events with only very soft gluons are indistinguishable from quark antiquark two-jet events.

Once the event has been generated, the particles are tracked through the TPC detector in a simulation program that includes the effects of bremstrahlung, energy loss by dE/dx, pair production by photons in the material before the TPC, and secondary vertices from the decays of K_s^0 and Λ particles. The program does not simulate the raw TPC data. Instead, the final pad hits are produced directly. The effects of overlapping tracks and sector boundaries are included in the simulation. The pad hits are smeared with errors given by the measured TPC resolutions including the effects of diffusion and angled tracks. The number of missing pads and the number of pads with large errors due to saturation, missing wires, and other effects are set to be the same as those for real (data) events. The effects of distortions are simulated by making the inner pad rows have larger errors. The tracks themselves are not distorted. A number of wires is assigned to each track based purely on geometry, the number of wires crossed, and the presence of neighboring tracks. As with the real data, no other track within ± 3 cm is allowed if a wire is to be assigned to a track. The known missing wires in each sector are then removed from the tracks and a small number of additional wires (≈ 8) subtracted to account for the effects of

delta rays. A value for dE/dx is assigned to each track using the form for dE/dx *vs.* momentum obtained by fitting the cosmic ray muon data. The value for dE/dx is then smeared according to the measured resolution and the number of wires on the track.

Although more fine tuning needs to be done, the Monte Carlo, TPCLUND, provides a good fit to the observed TPC data. Figure 5.1 shows a histogram of the number of wires on a track for both the real data and the Monte Carlo data. In both cases, the Monte Carlo provides a good fit to the real data. Figure 5.2 shows the histogram of the number of tracks with $P \geq 100$ MeV/c and vertex miss less than 5 cm in the xy plane and 10 cm in z for both the Monte Carlo and beam data. From this data, the average charged hadron multiplicity corrected for acceptance is $12.0 \pm .3 \pm 1.0$ [Hofmann 83], which is in good agreement with other experiments (see Fig. 5.3). The first error is statistical and the second systematic.

In figure 5.4, we show the distribution of events *vs.* visible momentum $= \sum|P|$ for all events with more than 4 tracks. The large excess at low visible momentum is due to two photon events. Both the two photon and two photon Monte Carlo events simulate the data well, enabling us to estimate the two photon background as well as the number of good one photon events lost to the visible momentum cut.

5.4 Radiative Corrections

The cross section that we wish to measure is the lowest order cross section for the process $e^+e^- \rightarrow$ hadrons. The cross section and the events themselves are considerably changed by the effects of radiative corrections. The lowest order diagram and the diagrams leading to the radiative corrections of order α^3 are shown in figure 5.5. We will only consider photon emission in the initial state, since the effects of final state radiation are smaller, primarily due to mass effects [Berends 81, Jackson 75]. (They are also much harder to calculate.) In calculating the radiative corrections, we will rely primarily on the work of Berends and Kleiss [Berends 81].

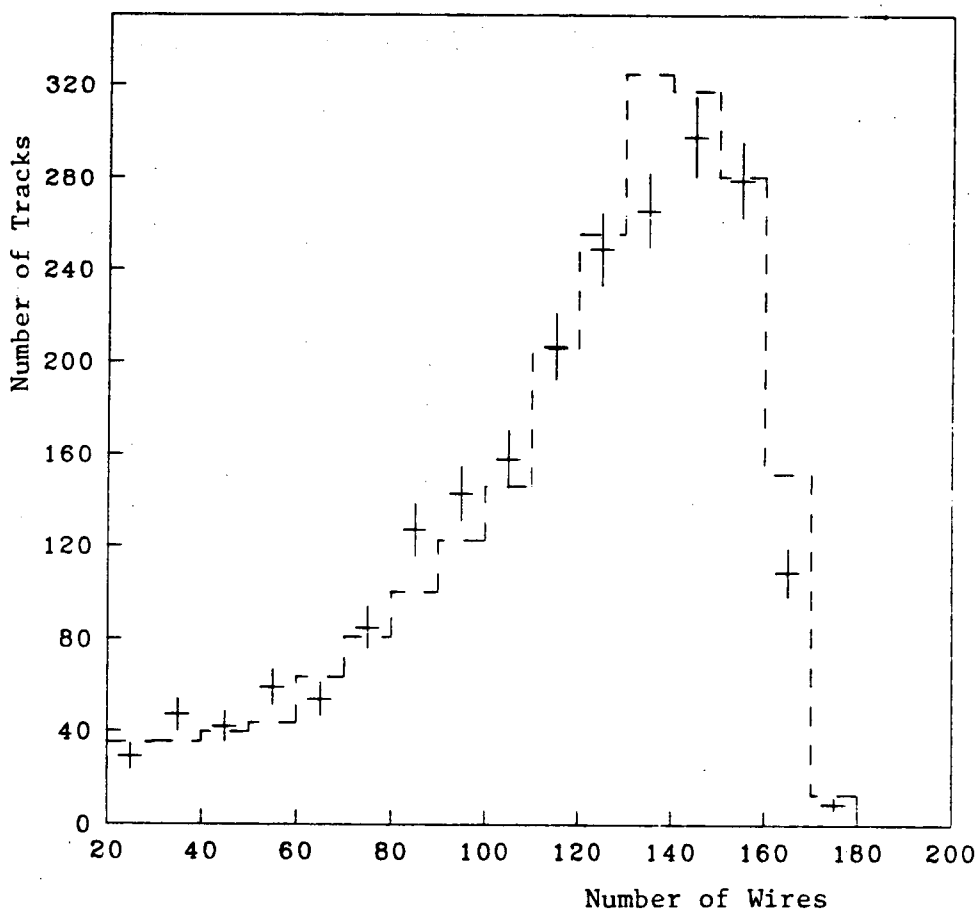

Figure 5.1

Distribution of the Number of Wires per Track.

The points are our data.

The dashed curve is the Monte Carlo prediction.

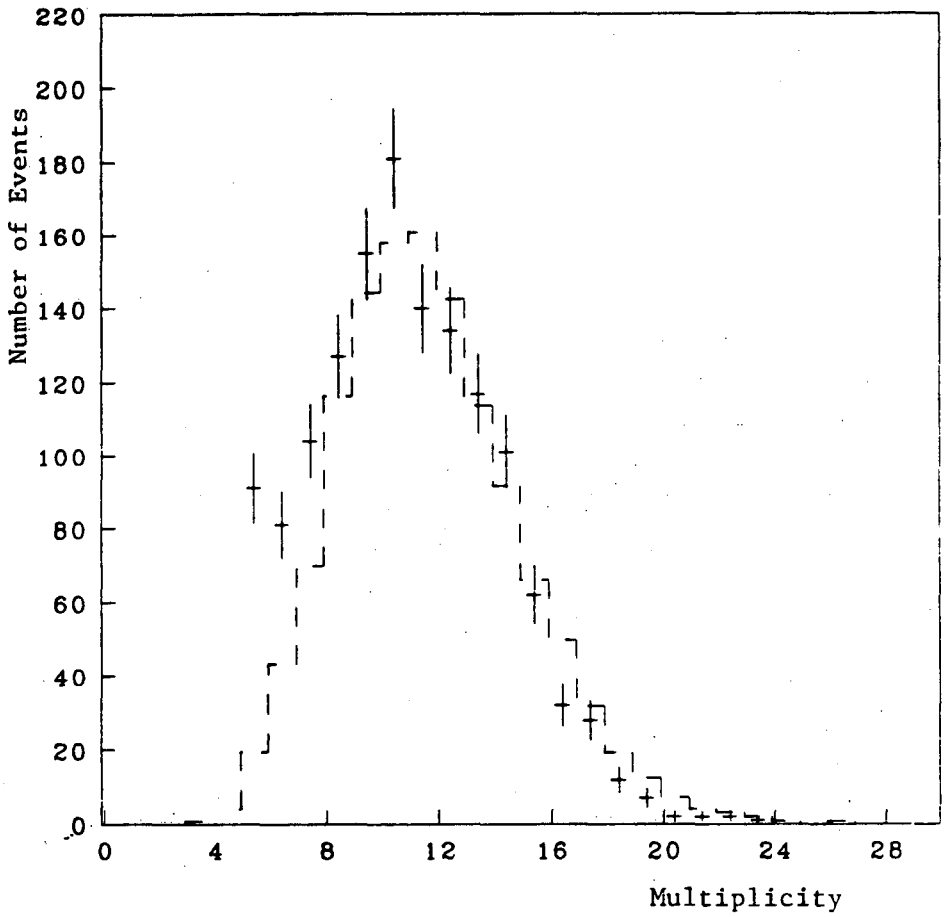

Figure 5.2

Number of Tracks per Event.

The points are our data.

The dashed curve is the Monte Carlo Prediction.

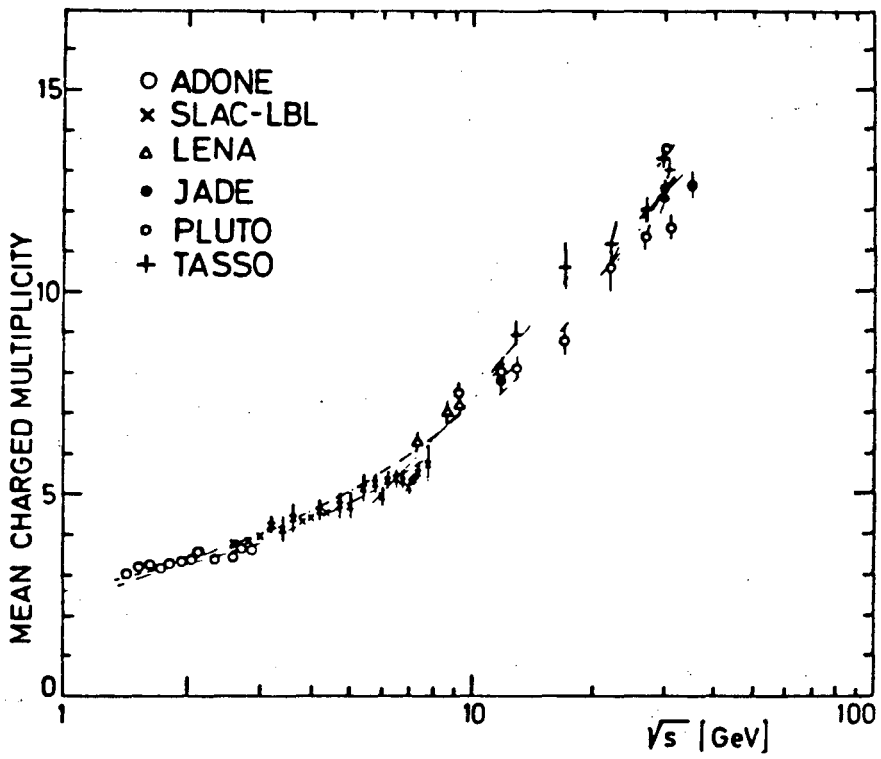

Figure 5.9. Mean Charged Multiplicity *vs.* $\sqrt{s}$- From Wolf 81

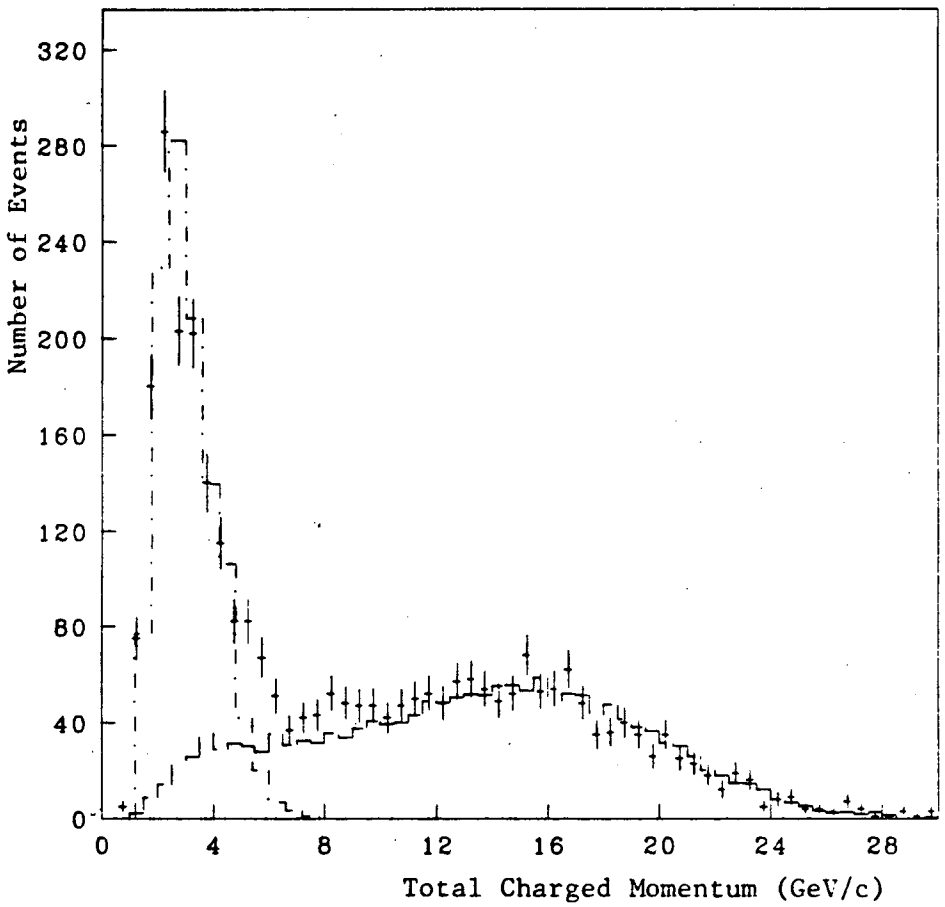

Figure 5.4

Number of Events *vs.* Visible Momentum.

The points are our data.

The dashed lines are the Monte Carlo predictions.

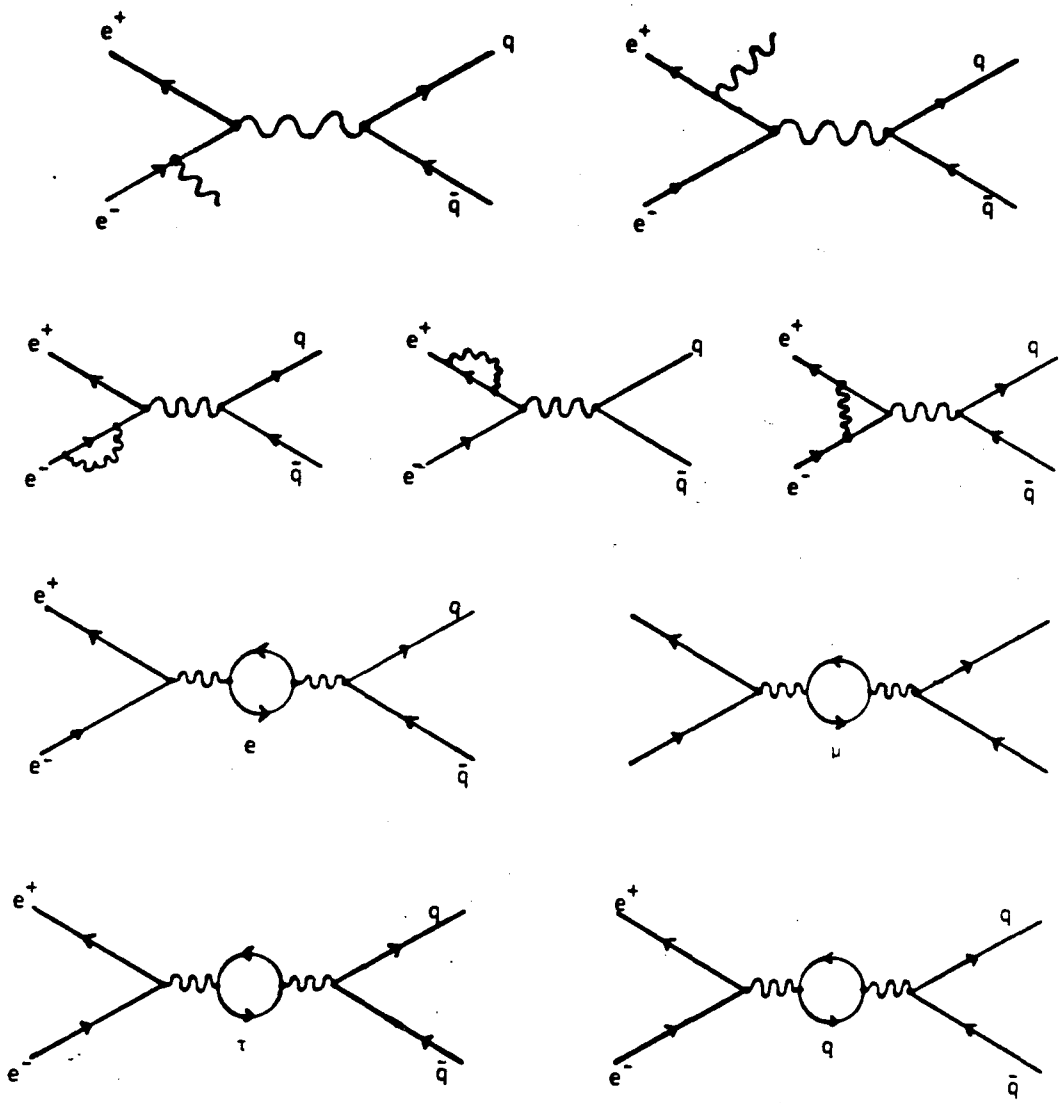

Figure 5.5. $e^+e^- \rightarrow$ hadrons to order α^3

The emission of an energetic photon by either the electron or positron in the initial state effectively lowers the $\sqrt{s}$ of the e^+e^- annihilation and, therefore, raises the apparent cross section since $\sigma \propto 1/s$. If we neglect final state radiation and assume that hadronization occurs separately from the basic production process, the cross section for $e^+e^- \rightarrow$ hadrons correct to order α^3 is given by [Berends 81]:

$$\begin{aligned}\sigma(s) &= \sigma_0\left(1+\delta_s + t\int_{k_{min}}^{k_{max}} \frac{dk}{k}\left(1-\frac{k}{E}+\frac{k^2}{2E^2}\right)\frac{\sigma_0(s')}{\sigma_0(s)}\right) \\ &= \sigma_0(1+\delta_s+\delta_{Hard}).\end{aligned} \tag{5.6}$$

where $E \equiv$ the beam energy, $s = 4E^2$, $k =$ photon energy.

$\delta_{Hard} \equiv$ corrections due to hard photons.

$\delta_s \equiv$ other corrections defined below.

$s' =$ reduced CMS energy squared $= 4E(E-k)$.

$\sigma_0 =$ lowest order (α^2) cross section.

$$t = \frac{2\alpha}{\pi}\left(\ln\frac{s}{m_e^2}-1\right). \tag{5.7}$$

δ_s is the sum of four terms, $\delta_s = \delta_A + \delta_\mu + \delta_\tau + \delta_{Had}$.

$$\delta_A = \frac{2\alpha}{\pi}\left(\ln\frac{s}{m_e^2}-1\right)\ln\frac{k_{min}}{E} \quad + \quad \frac{2\alpha}{\pi}\left[\frac{13}{12}\ln\frac{s}{m_e^2}+\frac{\pi^2}{6}-\frac{14}{9}\right]. \tag{5.8}$$

δ_A accounts for the soft bremstrahlung, electron vacuum polarization and vertex corrections.

$$\delta_{\mu,\tau} = \frac{2\alpha}{\pi}\left(\frac{1}{3}\ln\frac{s}{m_{\mu,\tau}^2}-\frac{5}{9}\right) \tag{5.9}$$

accounts for the vacuum polarization of muons or taus. At $\sqrt{s} = 29$ GeV, $\delta_\mu = 1.5\%$ and $\delta_\tau = 0.6\%$.

$$\delta_{Had} = -2 \times \mathrm{Re}\,\frac{s}{4\pi^2\alpha}\int_{4M_\pi^2}^{s}\frac{\sigma_0(s')}{s'-s}\,ds' \tag{5.10}$$

accounts for the vacuum polarization of hadrons. We are grateful to F.A.Berends and R.Kleiss for providing us with a copy of their FORTRAN program which calculates this dispersion integral.

The contributions of various resonances such as the ρ, ω, ψ family and the Υ to $\sigma_0(s')$ are included in the calculation. At $\sqrt{s} = 29$ GeV, $\delta_{Had} = 4.8\%$.

Both δ_A and the integral term diverge in the limit $k_{min} \to 0$. However, the sum of the two terms remains finite. In practice, the value of k_{min} is set sufficiently small so that photons of energy less than k_{min} would not be detected and would not change the event shape. We chose $k_{min} = 200MeV$.

The fraction of events with a hard photon is given by:

$$\frac{\delta_{Hard}}{1 + \delta_s + \delta_{Hard}}.$$

If an event has a hard photon, its energy spectrum is given by the distribution

$$\frac{1}{k}\left(1 - \frac{k}{E} + \frac{k^2}{2E^2}\right)\frac{\sigma_0(s')}{\sigma_0(s)}.$$

We assume $\sigma_0(s) =$ constant/s which is consistent with the constant value of R above 11 GeV.

The hard photon correction, δ_{Hard}, also diverges as $k_{Max} \to E$. Events that have radiated a photon with energy nearly equal to the beam energy will not pass the event selection cuts, since the photon will usually escape down the vacuum pipe, and the events will be indistinguishable from beam gas events. In figure 5.6 we show the acceptance as a function of radiated photon energy after all cuts. The product of $(1 + \delta_s + \delta_{Hard})$(detection efficiency) should be a constant for k_{max} above the value where the detection efficiency vanishes. This holds for $k_{max} \geq 12$ GeV (see table 5.1 and Fig. 5.6).

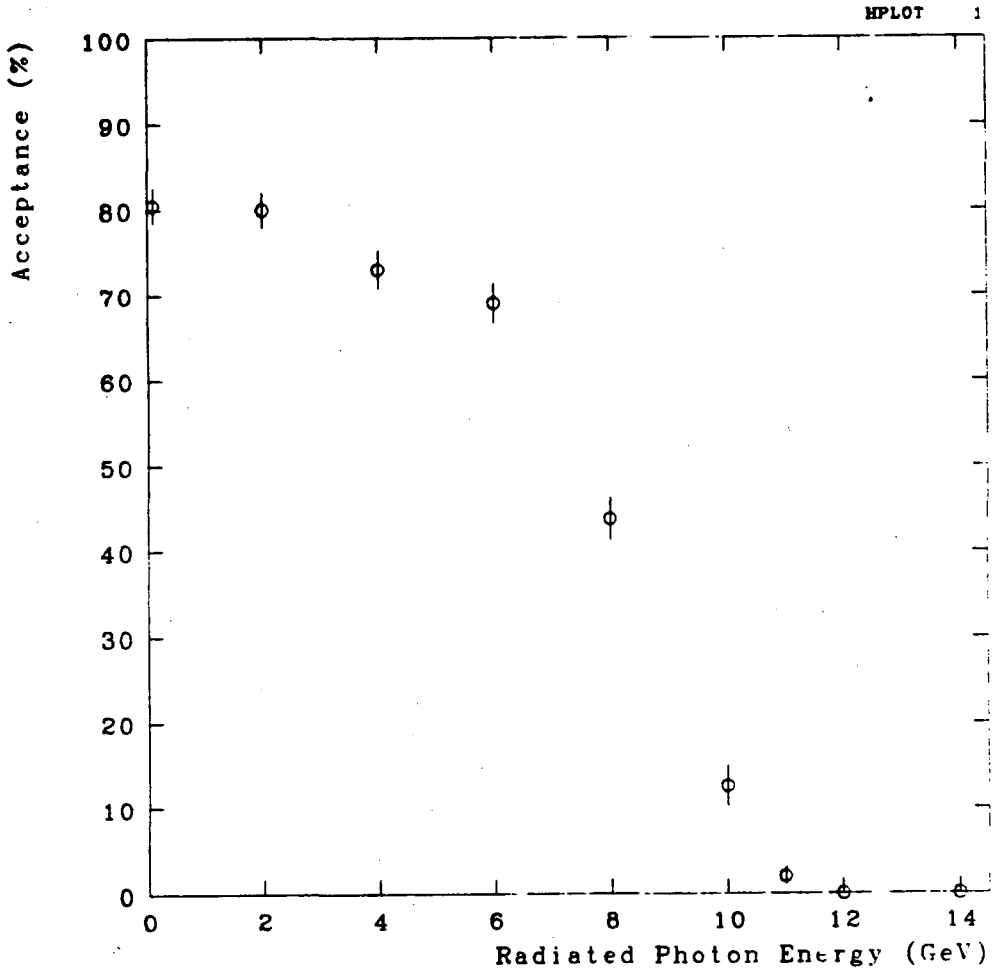

Figure 5.6. Acceptance *vs.* Radiated Photon Energy

k_{Max} [GeV]	$1+\delta_s+\delta_{Hard}$	Efficiency, ϵ [%]	$(1+\delta_s+\delta_{Hard})\epsilon$
14.0	1.293	$72.1 \pm .4$	$.932 \pm .005$
13.0	1.235	$74.8 \pm .4$	$.924 \pm .005$
12.5	1.219	$75.6 \pm .6$	$.922 \pm .007$
12.0	1.206	$76.9 \pm .3$	$.928 \pm .004$

Table 5.1. Radiative Corrections

From table 5.1 the average of the values of $(1 + \delta_s + \delta_{Hard})$(detection efficiency) is $.927 \pm .002$ where the error is only statistical. We estimate the error in the radiative corrections resulting from not including the higher order terms to be of the order of the correction squared or 5%. By varying the Monte Carlo parameters, we estimate the model dependent effects in the calculation of the acceptance to be of order 6%.

5.5 Backgrounds

The main sources of background events in the multihadron sample are $\tau\bar{\tau}$ events, two photon events, beam gas events, and junk events caused by a combination of cosmic ray tracks and noise tracks.

The contamination from the $e^+e^- \rightarrow \tau\bar{\tau}$ heavy lepton events was estimated using the Berends-Kleiss $\tau\bar{\tau}$ event generator and the same detector simulation program, TPCLUND, described previously. $\tau\bar{\tau}$ events are able to simulate multihadron events, since there are τ decays into 3 charged particles, and since the photons from π^0s can convert and create electron pairs which give additional tracks. The Berends-Kleiss $\tau\bar{\tau}$ event generator produces $\tau\bar{\tau}$ events with the correct angular distribution (mainly $1 + \cos^2\theta$) including weak-electromagnetic interference effects and radiative corrections up to order α^3. The $\tau\bar{\tau}$ contamination is given by the fraction of $e^+e^- \rightarrow \tau\bar{\tau}$ events passing the hadronic event cuts, multiplied by the ratio of the $\tau\bar{\tau}$ cross section to the multihadronic cross section.

We used 3/11, as given by lowest order QCD and the parton model, for the ratio $\sigma(\tau\overline{\tau})/\sigma(hadrons)$. The value of $(3.16 \pm .09 \pm 1.5)\%$ was obtained for the $\tau\overline{\tau}$ contamination where the first error is statistical and the second is systematic. The systematic error is due to the uncertainties in the branching ratios for $\tau\overline{\tau}$ decay into three charged particles.

The two photon background was determined using a two photon event generator and the TPCLUND detector simulation program. The two photon background is estimated to be $2.0 \pm 0.5\%$(see Fig. 5.4). The error is due to the uncertainties in the generation of the two photon events, in the generation of event multiplicities, and in the $p_\perp$ distributions.

The beam gas background is estimated to be less than 1% from examining the tails of the distribution of event vertices in z for events that pass the cuts.

The junk event background was determined by hand scanning 350 multihadron events. It consists of vertical cosmic ray plus noise track events. This background is $2.5 \pm 0.8\%$ where the error is statistical only.

5.6 Luminosity

It is extrmemely difficult to monitor the beam parameters such as bunch size and intensity necessary to calculate the luminosity. We, therefore, use Bhabha events ($e^+e^- \rightarrow e^+e^-$) as found by the poletip calorimeters to calculate the integrated luminosity received by PEP-4.

The poletip Bhabha events are required to pass the following cuts:

1. Both poletip showers greater than 5 GeV in energy.
2. Acollinearity between the showers less than 10 degrees.
3. Angle with respect to the beam direction of each hit

   within the limits 15.7^o to 32.9^o .

Since the charge of the tracks was not measured, both Bhabha events, and $e^+e^- \to \gamma\gamma$ events, were accepted. Here, $e^+e^- \to \gamma\gamma$ events are those in which the electron and positron annihilate into two real photons. The cross section for these processes was determined using the Berends-Kleiss Bhabha and $\gamma\gamma$ event generators and a Monte Carlo program simulating the poletip response. The Bhabha cross section was calculated including weak-electromagnetic interference effects and radiative corrections to order α^3. The $e^+e^- \to \gamma\gamma$ cross section was calculated to lowest order only, since it is much smaller. The Bhabha cross section for events selected as given above was calculated to be 11.63 nb. The $e^+e^- \to \gamma\gamma$ cross section was found to be 0.22 nb.

The total number of accepted events was 42360. The angular distribution of the events is described well by the Monte Carlo calculation and is given in figure 5.7. The total integrated luminosity, $\int \mathcal{L}\, dt$, is given by:

$$\frac{42360}{11.85} = 3575 \pm 17\text{nb}^{-1} \tag{5.11}$$

where the error is statistical only. If the angular cuts are varied from $15.7^\circ < \theta < 32.9^\circ$ to $19.9^\circ < \theta < 30.7^\circ$, the calculated value for the integrated luminosity varies by less than 2%, although the total number of events changes by a factor of 2. We estimate the total systematic error in the luminosity measurement to be 6% to allow for errors in the detector simulation, radiative corrections, and the trigger. This error could be reduced if there were results from wide angle Bhabhas to check this determination, but, unfortunately, only two of the six hexagonal calorimeter modules were installed when this data was taken.

5.7 Total Cross Section and R

We are now ready to calculate the total cross section. 1356 candidate multihadron events passed the selection cuts. Of these, we have estimated that 3.16% are $\tau\bar{\tau}$ events, 2% are

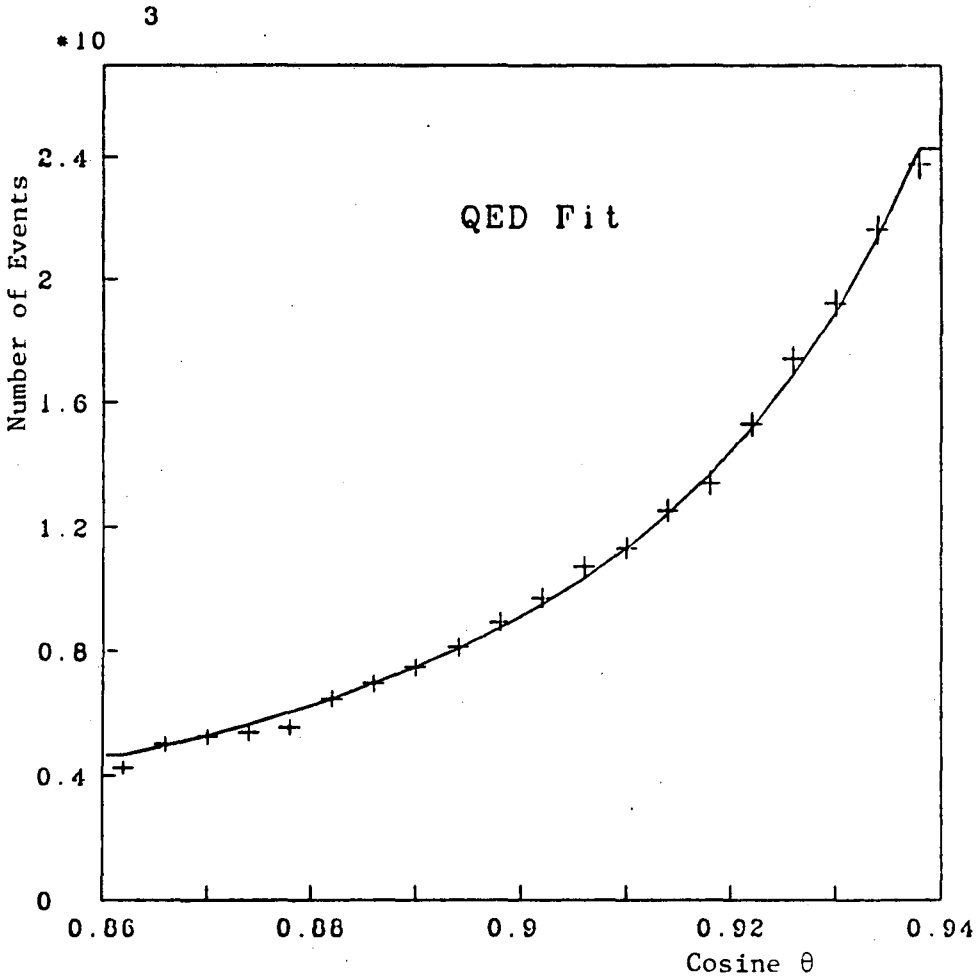

Figure 5.7. Bhabha Events - Angular Distribution

two photon events, 0.5% are beam gas events, and 2.5% are cosmic ray junk events. There are 1245 good events and a total contamination of 8.2%. The lowest order cross section, σ_0, is then given by:

$$\sigma_0 = \frac{\text{Number of Events}}{(\text{Efficiency})(1+\delta_s+\delta_{Hard})\times\int \mathcal{L}\,dt} = \frac{1245}{0.927\times .993\times 3575} = .38 \pm .01 \pm .04\text{nb}. \tag{5.12}$$

where the first error is statistical and the second is systematic. The efficiency is the product of the event selection efficiency and the trigger efficiency. The systematic error includes the given systematic errors added in quadrature. The sources of the systematic errors are summarized in table 5.2.

With $\sigma_0(e^+e^- \to \mu^+\mu^-) = 4\pi\alpha^2/3s = .103$ nb. at $\sqrt{s} = 29$ GeV, we obtain:

$$R = \frac{\sigma_0(e^+e^- \to \text{hadrons})}{\sigma_0(e^+e^- \to \mu^+\mu^-)} = 3.7 \pm 0.1 \pm 0.4. \tag{5.13}$$

This value for R is in agreement within errors with other measurements made by other experiments near $\sqrt{s} = 29$ GeV, although it is lower than most of the other measurements (see Fig. 2.2). The lowest order theoretical value for R is given by:

$$R = \sum 3e_{q_i}^2 = \frac{11}{3} = 3.66\,. \tag{5.14}$$

The corrections due to first and second order QCD effects and weak-electromagnetic interference effects have been calculated [Appelquist 75, Celmaster 79, Chetyrkin 79, Dine 79, Jersak 81]. The effect of these corrections is to raise the theoretical prediction for the value of R to be $\approx$ 3.9, where we assume $\sin^2\theta_W$ to be of order .2 or .25 and α_s of order .1 to .2 in agreement with current measurements. (θ_W is the Weinberg angle.) The errors on our value for R are too large to distinguish between the lowest order and corrected theoretical values and, therefore, to determine α_s or θ_W within significant limits. The sources of our large errors are low statistics and the absence of calorimeters in the central detection region. The low statistics make it difficult to vary

widely the cuts made in selecting the events to check for systematic biases. (We did vary the event selection cuts to require more charged tracks and more total detected momentum. Measurements with tighter event cuts require a larger correction from the Monte Carlo for acceptance, but have fewer background events in the sample. The value for the total cross section changed by less than 4%.) Without the hexagonal calorimeters, the forward Bhabhas from the poletip calorimeter cannot be checked against the wide angle Bhabhas to improve the luminosity determination. Furthermore, wide angle total energy triggers cannot be used to determine the efficiency of the charged particle triggers, and the energy flow information from the calorimeters cannot be used to improve and check the event selection.

Source	Error
$\tau\bar{\tau}$ Event Subtraction	1.5%
Beam Gas Event Subtraction	0.5%
Two Photon Event Subtraction	0.5%
Cosmic Ray Event Subtraction	0.8%
Event Acceptance	6%
Higher Order Radiative Corrections	5%
Trigger Efficiency	0.4%
Luminosity	6%

Table 5.2. Sources of Systematic Error in R

5.8 Event Topology

We expect the tracks in $e^+e^- \rightarrow$ hadrons events to be emitted in two (or occasionally three) back to back cones. Two standard measures of the event shape are sphericity (S) and thrust (T). Sphericity is defined by:

$$S = \frac{3}{2} \times \min \frac{\sum P_\perp^2}{\sum P^2} \qquad 0 \leq S \leq 1 \tag{5.15}$$

where $P_\perp$ is the perpendicular momentum with respect to the axis chosen so that $\sum P_\perp$ is a minimum. Thrust is defined by:

$$T = \max \frac{\sum |P_{\parallel}|}{\sum |P|} \qquad \frac{1}{2} \leq T \leq 1 \tag{5.16}$$

where $P_{\parallel}$ is the momentum parallel to the axis chosen so that $\sum |P_{\parallel}|$ is a maximum. For spherical events, $S \rightarrow 1$, while for events in which the particles are confined to back to back narrow cones, $s \rightarrow 0$. Thrust behaves oppositely. Thrust approaches 1/2 for spherical events, and 1 for back-to-back jet events.

Including acceptance corrections, the PEP-4 values for thrust and sphericity averaged over the hadronic event sample are [Hofmann 83]:

$$\langle S \rangle = .122 \pm .004 \pm .006 \tag{5.17}$$

$$\langle 1 - T \rangle = .092 \pm .002 \pm .002 \tag{5.18}$$

where for both equations the first error is statistical and the second, systematic. The acceptance corrections were made using the TPCLUND event generator and detector simulation described previously. Both of these results are in good agreement with the results of other experiments made at the same energy (see Fig. 5.8 and fig. 5.9). As can be seen from figures 5.7 and 5.8, both the average value for S and the average value of $1 - T$ decrease with increasing $\sqrt{s}$. As energies have increased from 7 GeV where jets were first seen, jets have been becoming narrower, although the rate of narrowing has decreased at the highest energies as gluon emission has become more important.

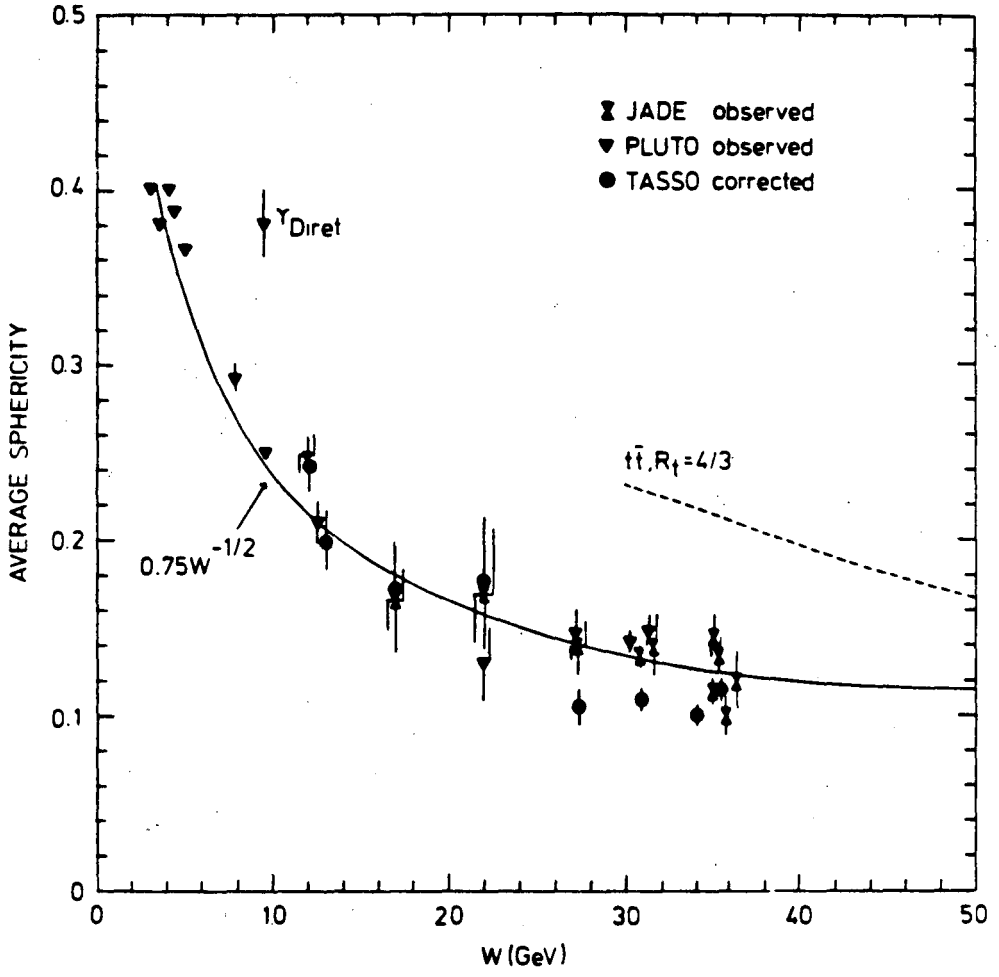

Figure 5.8. Average Sphericity *vs.* $\sqrt{s}$—From Wolf 81

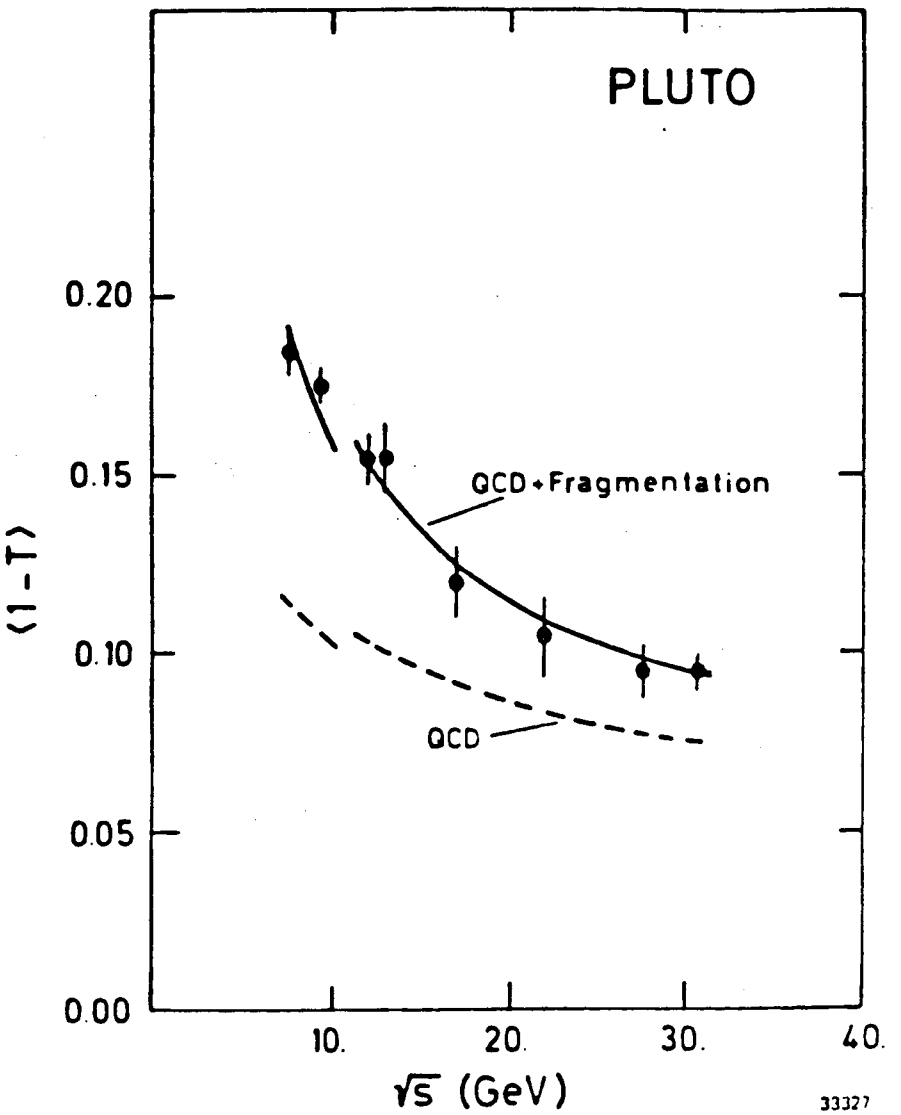

Figure 5.9. Average of (1 — *Thrust*) *vs.* $\sqrt{s}$—From Berger 81

Chapter 6

Inclusive Particle Production

In this chapter, we will discuss the production of charged hadrons ($\pi^{\pm}$, $K^{\pm}$, $P^{\pm}$) in multihadron events. We will begin with the measurement of the fractions of $\pi^{\pm}$, $K^{\pm}$, and $P^{\pm}$ as a function of momentum and then present the differential cross sections, $\frac{s}{\beta}\frac{d\sigma}{dx}$, separated by particle species, where $x \equiv E_{Hadron}/E_{beam}$. The results will be compared with various models for particle production. The number of kaons will be shown to be too large to be accounted for by direct $s\bar{s}$ or $c\bar{c}$ or $b\bar{b}$ events. The ratio of up to strange quarks pulled from the vacuum will be determined using the LUND model.

The problem of measuring the particle fractions by dE/dx can be divided into two parts. The first is to obtain the raw number of particles of each type from the bands of separated particles of the different types shown in figure 6.1. The second is to correct the raw particle numbers for the effects of decays and nuclear interactions for the various particle types in order to obtain the final fractions. We will assume that the angular distributions of the different particle types is the same and that the probability of tracks overlapping, or tracks being too close to the beam direction to be detected, is the same for pions, kaons, and protons. According to the Monte Carlo, this assumption is correct. Since the TPC is very well segmented and covers a large amount of solid angle, it is no more sensitive to such effects than other detectors.

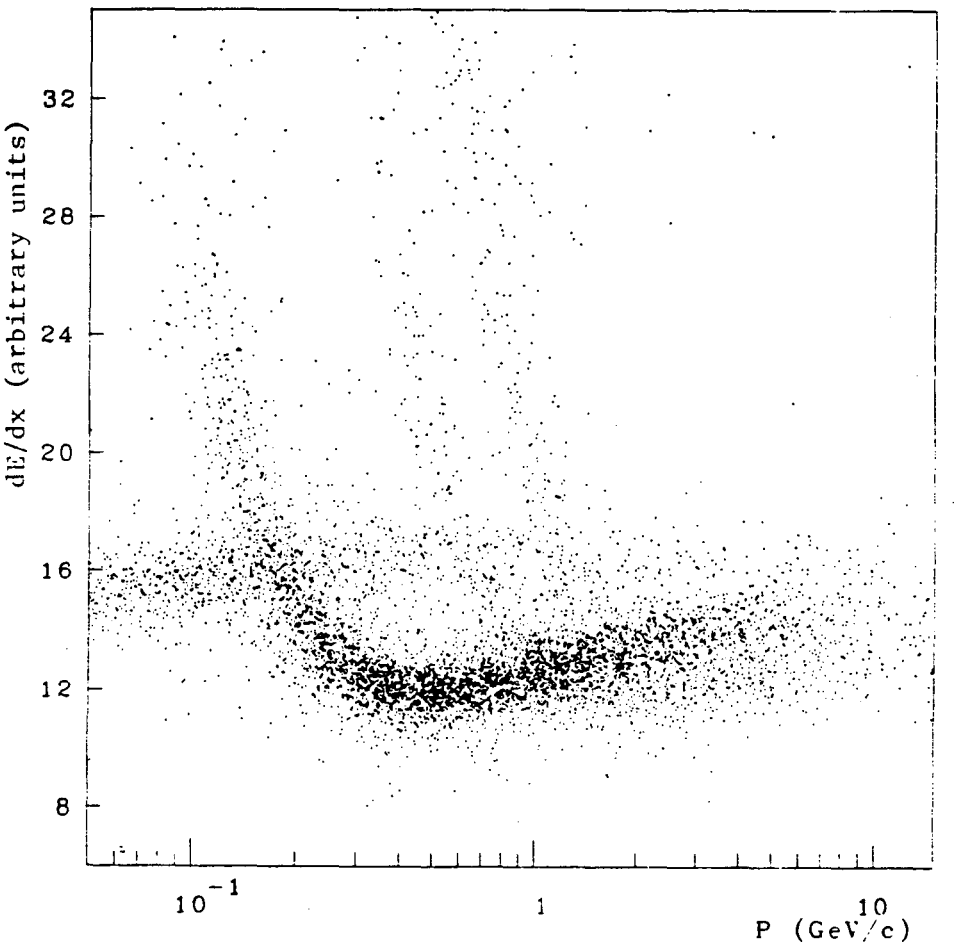

Figure 6.1. dE/dx *vs.* Momentum —Multihadron Events

6.1 Raw Particle Numbers

In calculating the raw particle numbers, we will need to consider three momentum regions. In the first, the low momentum region from 300 MeV/c to 1 GeV/c, the kaons and protons are still too slow to be minimum ionizing and their values of dE/dx are falling as $1/\beta^2$. In the second, the crossover region from 1 GeV/c to 2.7 GeV/c, the values of dE/dx for pions, kaons, and protons have converged and particle separation is impossible given our current dE/dx resolution. (Even with perfect dE/dx resolution, there are momenta at which the dE/dx values for two particle types are identical. At such momenta, particle separation by dE/dx may be possible by considering the detailed shape of the energy loss distributions [Talman 79]. Separation at such momenta is predicted to be difficult even theoretically, and will not be considered here.) In the third, the high momentum or relativistic rise region starting at 2.7 GeV/c, it is possible to separate pions from kaons and protons on a statistical basis.

6.1.1 Low Momentum Data

In the low momentum region from 300 MeV/c to 1 GeV/c, the main difficulty in obtaining the raw particle numbers comes in separating the kaons and protons from the electrons in the crossover regions. The large number of electrons visible in figure 6.1 is due to photon conversions in the material (about 0.2 radiation lengths) before the TPC. The main source of photons is π^0 decays. From the measurements of other experiments, there are about 5 π^0s per event [Wolf 81]. The number of electrons seen in the TPC is compatible with this number. Also, because of the large amount of material before the TPC, the data contains about two or three times as many protons as antiprotons due to nuclear interactions. Because e^+e^- annihilations are particle antiparticle symmetric by CP conservation, the number of protons and antiprotons should be equal. Since determining this large number of protons produced in nuclear interactions

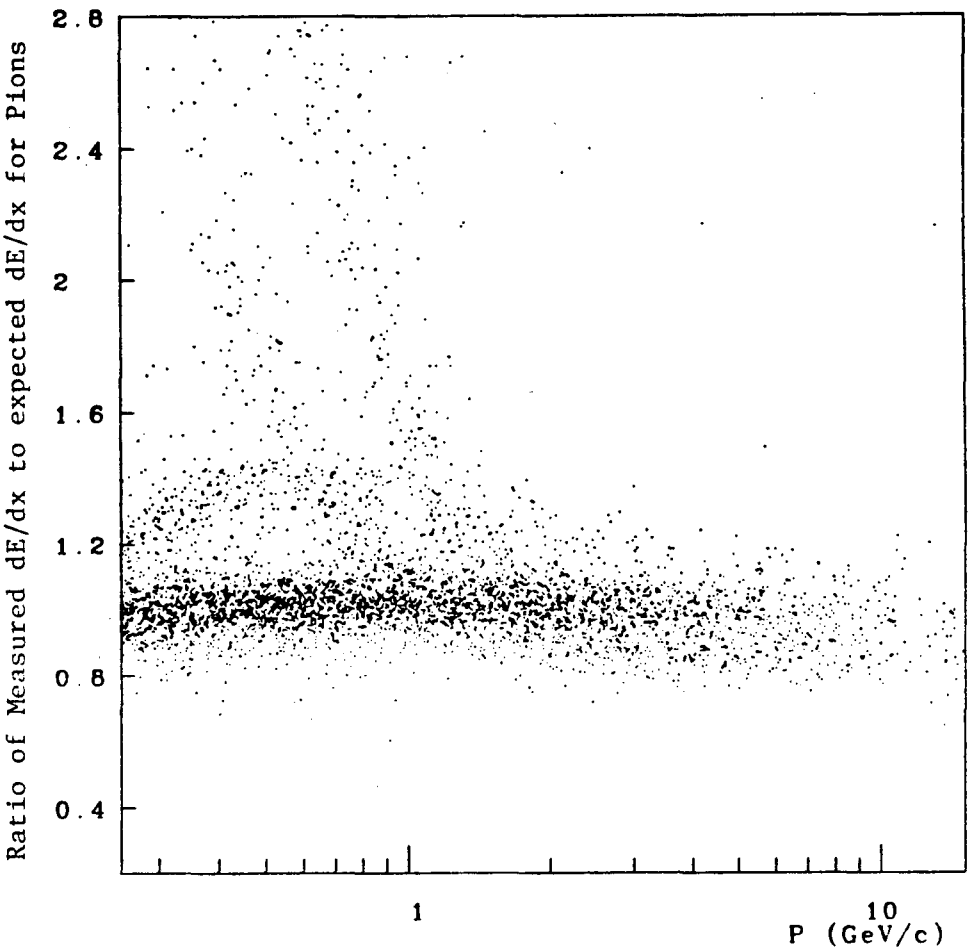

Figure 6.2

Ratio of measured dE/dx to expected dE/dx for pions *vs.* momentum

sufficiently accurately would be very difficult, we will use twice the antiproton fraction for the proton plus antiproton fraction.

To calculate the raw particle numbers in the low momentum region, we use a plot of the ratio of measured dE/dx to dE/dx, calculated for a pion at that momentum (See Fig. 6.2). The multihadron events were selected as described in the previous chapter. All tracks in the plot were required to have more than 80 good wires associated with them, to come from within ± 5 cm of the interaction point in xy and within ± 10 cm in z. The 80 wire cut ensures a good measurement of dE/dx. The vertex cuts ensure that the tracks are beam associated. As it will be needed extensively, we will use the symbol, A, to represent the ratio of measured dE/dx to dE/dx, calculated for a pion at the same momentum.

We divide the low momentum data into 7 momentum bins, each roughly 100 MeV/c wide and centered at 354, 452, 552, 674, 780, 862, and 952 MeV/c respectively. The number of pions in a given momentum interval is obtained from figure 6.2 where pions are taken to be those particles with $A < 1.6$. Figure 6.3 shows the projection on the A axis of figure 6.2 for the data in the 552 MeV/c momentum bin. The non-gaussian tails in the pion distribution are less than 2 %. The smallness of these tails enables us to separate the pions from kaons up to 862 MeV/c, close to the crossover region. For the momentum bins at 674 MeV/c and 780 MeV/c, those particles with $A > 1.10$ that are in the non-gaussian tail above the 2 % level are called kaons. The kaon contribution to the tails in these momentum bins is consistent with the Monte Carlo. Figure 6.4 shows the projection on the A axis of figure 6.2 for the data in the 862 MeV/c momentum bin. The increase in the non-gaussian tail above $A = 1.10$ is evident. In the 952 MeV/c momentum bin, the kaon and pion values for dE/dx are nearly equal, and the particles can no longer be separated.

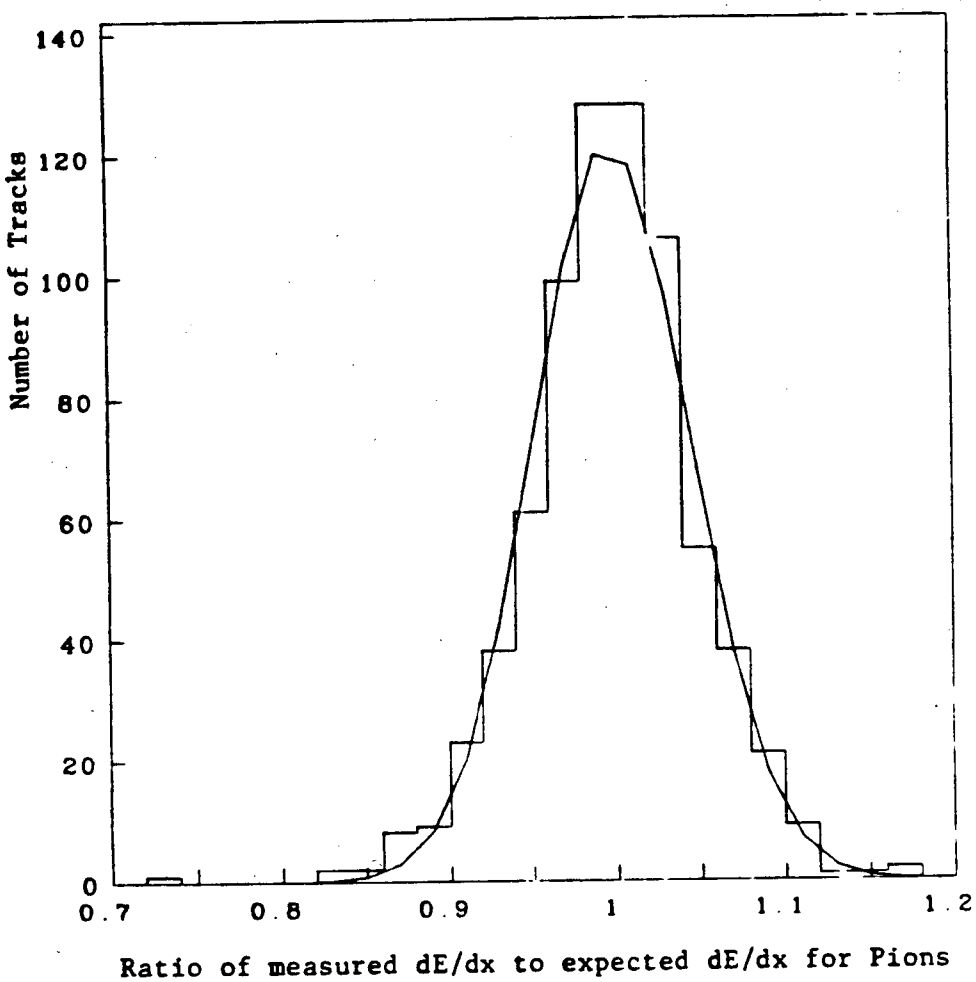

Figure 6.9

Ratio of measured dE/dx to expected dE/dx for pions— 552 MeV/c Momentum Bin

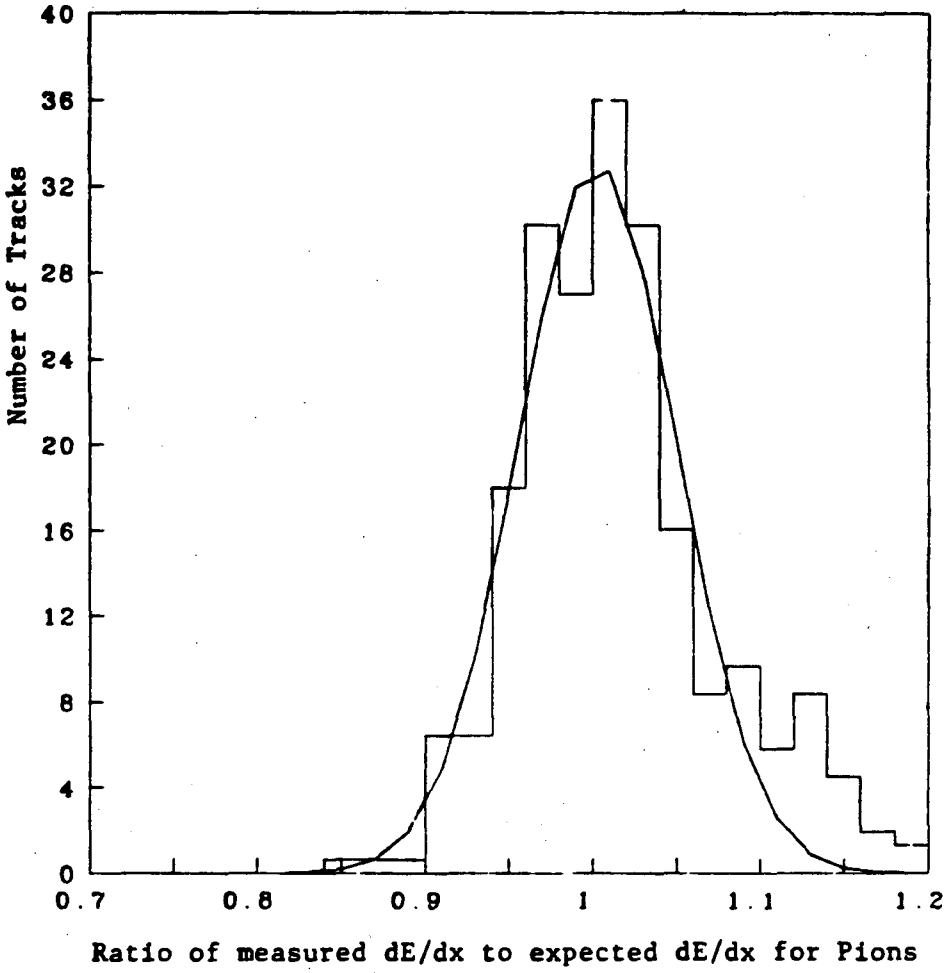

Figure 6.4

Ratio of measured dE/dx to expected dE/dx for pions —862 MeV/c Momentum Bin

	Ratio of Measured dE/dx to Expected dE/dx for Pions								
P (MeV/c)	1.5–1.6	1.6–1.7	1.7–1.8	1.8–2.0	2.0–2.2	2.2–2.5	2.5–2.8	2.8–2.9	> 2.9
301–333	$0_K\ 0_P$	$0_K\ 0_P$	$0_K\ 0_P$	$0_K\ 0_P$	$6_K\ 0_P$	$18_K\ 0_P$	$47_K\ 0_P$	$10_K\ 0_P$	$31_K\ 0_P$
333–368	$0_K\ 0_P$	$0_K\ 0_P$	$1_K\ 0_P$	$4_K\ 0_P$	$24_K\ 0_P$	$55_K\ 0_P$	$43_K\ 0_P$	$8_K\ 0_P$	$14_K\ 0_P$
368–407	$0_K\ 0_P$	$0_K\ 0_P$	$6_K\ 0_P$	$30_K\ 0_P$	$64_K\ 0_P$	$59_K\ 0_P$	$18_K\ 0_P$	$0_K\ 0_P$	$2_K\ 18_P$
407–449	$3_K\ 0_P$	$4_K\ 0_P$	$21_K\ 0_P$	$88_K\ 0_P$	$63_K\ 0_P$	$18_K\ 0_P$	$3_K\ 0_P$	$0_K\ 0_P$	$1_K\ 44_P$
449–497	$21_K\ 0_P$	$47_K\ 0_P$	$69_K\ 0_P$	$85_K\ 0_P$	$21_K\ 0_P$	$3_K\ 0_P$	$1_K\ 0_P$	$0_K\ 0_P$	$1_K\ 34_P$
497–549	$72_K\ 0_P$	$90_K\ 0_P$	$42_K\ 0_P$	$15_K\ 0_P$	$1_K\ 0_P$	$0_K\ 0_P$	$0_K\ 3_P$	$0_K\ 0_P$	$0_K\ 63_P$
549–607	$73_K\ 0_P$	$27_K\ 0_P$	$8_K\ 0_P$	$2_K\ 0_P$	$1_K\ 1_P$	$0_K\ 3_P$	$0_K\ 9_P$	$0_K\ 4_P$	$0_K\ 66_P$
607–670	$17_K\ 0_P$	$3_K\ 0_P$	$0_K\ 0_P$	$0_K\ 0_P$	$0_K\ 1_P$	$0_K\ 22_P$	$0_K\ 32_P$	$0_K\ 7_P$	$0_K\ 21_P$
670–741	$2_K\ 0_P$	$1_K\ 1_P$	$0_K\ 1_P$	$0_K\ 4_P$	$0_K\ 14_P$	$0_K\ 43_P$	$0_K\ 15_P$	$0_K\ 6_P$	$0_K\ 6_P$
741–819	$0_K\ 2_P$	$0_K\ 1_P$	$0_K\ 7_P$	$0_K\ 38_P$	$0_K\ 53_P$	$0_K\ 25_P$	$0_K\ 9_P$	$0_K\ 1_P$	$0_K\ 0_P$
819–905	$0_K\ 5_P$	$0_K\ 17_P$	$0_K\ 39_P$	$0_K\ 52_P$	$0_K\ 22_P$	$0_K\ 4_P$	$0_K\ 0_P$	$0_K\ 0_P$	$0_K\ 0_P$
905–1000	$0_K\ 41_P$	$0_K\ 35_P$	$0_K\ 22_P$	$0_K\ 21_P$	$0_K\ 0_P$	$0_K\ 0_P$	$0_K\ 0_P$	$0_K\ 0_P$	$0_K\ 1_P$

Table 6.1. Numbers of Kaons and Protons in the $1/\beta^2$ Region— Monte Carlo Data

	Ratio of Measured dE/dx to Expected dE/dx for Pions								
P (MeV/c)	1.5–1.6	1.6–1.7	1.7–1.8	1.8–2.0	2.0–2.2	2.2–2.5	2.5–2.8	2.8–2.9	> 2.9
301–333	$0_K\ 0_P$	$0_K\ 0_P$	$1_K\ 0_P$	$0_K\ 0_P$	$0_K\ 0_P$	$1_K\ 0_P$	$4_K\ 0_P$	$0_K\ 0_P$	$5_K\ 0_P$
333–368	$0_K\ 0_P$	$0_K\ 0_P$	$1_K\ 0_P$	$0_K\ 0_P$	$3_K\ 0_P$	$3_K\ 0_P$	$3_K\ 0_P$	$0_K\ 0_P$	$5_K\ 3_P$
368–407	$1_K\ 0_P$	$0_K\ 0_P$	$2_K\ 0_P$	$2_K\ 0_P$	$5_K\ 0_P$	$1_K\ 0_P$	$4_K\ 0_P$	$0_K\ 0_P$	$0_K\ 11_P$
407–449	$1_K\ 0_P$	$4_K\ 0_P$	$3_K\ 0_P$	$8_K\ 0_P$	$6_K\ 0_P$	$2_K\ 0_P$	$1_K\ 0_P$	$0_K\ 0_P$	$0_K\ 11_P$
449–497	$1_K\ 0_P$	$2_K\ 0_P$	$4_K\ 0_P$	$3_K\ 0_P$	$2_K\ 0_P$	$2_K\ 0_P$	$1_K\ 0_P$	$0_K\ 0_P$	$0_K\ 12_P$
497–549	$6_K\ 0_P$	$5_K\ 0_P$	$3_K\ 0_P$	$5_K\ 0_P$	$1_K\ 0_P$	$1_K\ 0_P$	$0_K\ 5_P$	$0_K\ 1_P$	$0_K\ 24_P$
549–607	$5_K\ 0_P$	$3_K\ 0_P$	$2_K\ 0_P$	$1_K\ 0_P$	$0_K\ 0_P$	$0_K\ 3_P$	$0_K\ 6_P$	$0_K\ 3_P$	$0_K\ 16_P$
607–670	$1_K\ 0_P$	$1_K\ 0_P$	$1_K\ 0_P$	$0_K\ 0_P$	$0_K\ 3_P$	$0_K\ 5_P$	$0_K\ 11_P$	$0_K\ 1_P$	$0_K\ 7_P$
670–741	$0_K\ 0_P$	$1_K\ 0_P$	$0_K\ 1_P$	$0_K\ 1_P$	$0_K\ 7_P$	$0_K\ 5_P$	$0_K\ 6_P$	$0_K\ 0_P$	$0_K\ 1_P$
741–819	$0_K\ 1_P$	$0_K\ 2_P$	$0_K\ 0_P$	$0_K\ 2_P$	$0_K\ 6_P$	$0_K\ 6_P$	$0_K\ 3_P$	$0_K\ 0_P$	$0_K\ 5_P$
819–905	$0_K\ 0_P$	$0_K\ 2_P$	$0_K\ 8_P$	$0_K\ 9_P$	$0_K\ 4_P$	$0_K\ 3_P$	$0_K\ 3_P$	$0_K\ 0_P$	$0_K\ 3_P$
905–1000	$0_K\ 9_P$	$0_K\ 4_P$	$0_K\ 1_P$	$0_K\ 3_P$	$0_K\ 3_P$	$0_K\ 3_P$	$0_K\ 1_P$	$0_K\ 0_P$	$0_K\ 1_P$

Table 6.2. Numbers of Kaons and Protons in the $1/\beta^2$ Region— Both Charges

	Ratio of Measured dE/dx to Expected dE/dx for Pions								
P (MeV/c)	1.5–1.6	1.6–1.7	1.7–1.8	1.8–2.0	2.0–2.2	2.2–2.5	2.5–2.8	2.8–2.9	> 2.9
301–333	$0_K\ 0_P$	$0_K\ 0_P$	$0_K\ 0_P$	$0_K\ 0_P$	$0_K\ 0_P$	$1_K\ 0_P$	$3_K\ 0_P$	$0_K\ 0_P$	$1_K\ 0_P$
333–368	$0_K\ 0_P$	$0_K\ 0_P$	$1_K\ 0_P$	$0_K\ 0_P$	$1_K\ 0_P$	$1_K\ 0_P$	$2_K\ 0_P$	$0_K\ 0_P$	$3_K\ 0_P$
368–407	$0_K\ 0_P$	$0_K\ 0_P$	$1_K\ 0_P$	$0_K\ 0_P$	$2_K\ 0_P$	$0_K\ 0_P$	$1_K\ 0_P$	$0_K\ 0_P$	$0_K\ 1_P$
407–449	$1_K\ 0_P$	$3_K\ 0_P$	$1_K\ 0_P$	$3_K\ 0_P$	$4_K\ 0_P$	$0_K\ 0_P$	$0_K\ 0_P$	$0_K\ 0_P$	$0_K\ 2_P$
449–497	$0_K\ 0_P$	$1_K\ 0_P$	$3_K\ 0_P$	$0_K\ 0_P$	$1_K\ 0_P$	$0_K\ 0_P$	$0_K\ 0_P$	$0_K\ 0_P$	$0_K\ 2_P$
497–549	$4_K\ 0_P$	$2_K\ 0_P$	$1_K\ 0_P$	$2_K\ 0_P$	$0_K\ 0_P$	$0_K\ 0_P$	$0_K\ 0_P$	$0_K\ 0_P$	$0_K\ 3_P$
549–607	$1_K\ 0_P$	$1_K\ 0_P$	$1_K\ 0_P$	$0_K\ 0_P$	$0_K\ 0_P$	$0_K\ 0_P$	$0_K\ 2_P$	$0_K\ 0_P$	$0_K\ 1_P$
607–670	$0_K\ 0_P$	$1_K\ 0_P$	$0_K\ 0_P$	$0_K\ 0_P$	$0_K\ 0_P$	$0_K\ 1_P$	$0_K\ 2_P$	$0_K\ 0_P$	$0_K\ 0_P$
670–741	$0_K\ 0_P$	$0_K\ 0_P$	$0_K\ 1_P$	$0_K\ 0_P$	$0_K\ 0_P$	$0_K\ 0_P$	$0_K\ 0_P$	$0_K\ 0_P$	$0_K\ 0_P$
741–819	$0_K\ 1_P$	$0_K\ 0_P$	$0_K\ 0_P$	$0_K\ 0_P$	$0_K\ 1_P$	$0_K\ 2_P$	$0_K\ 1_P$	$0_K\ 0_P$	$0_K\ 1_P$
819–905	$0_K\ 0_P$	$0_K\ 1_P$	$0_K\ 1_P$	$0_K\ 0_P$	$0_K\ 0_P$	$0_K\ 0_P$	$0_K\ 0_P$	$0_K\ 0_P$	$0_K\ 1_P$
905–1000	$0_K\ 4_P$	$0_K\ 1_P$	$0_K\ 1_P$	$0_K\ 0_P$	$0_K\ 0_P$	$0_K\ 1_P$	$0_K\ 0_P$	$0_K\ 0_P$	$0_K\ 0_P$

Table 6.3. Numbers of Kaons and Protons in the $1/\beta^2$ Region— Negative Charges Only

The number of protons and kaons in the region in A above the electron band, A > 1.50, in a given momentum bin, is determined by dividing the plot of A *vs.* momentum into small enough areas so that only particles of one type are in any given area. The binning was obtained by eye from figure 6.2 and checked using the Monte Carlo. Table 6.1 shows the distribution of kaons and protons in the bins chosen to determine the number of kaons and protons for 11,000 Monte Carlo events. As can be seen from the table, particles of only one type dominate each of the bins. Tables 6.2 and 6.3 show the same distribution for the real data, for both charges combined and for negative charged particles only, respectively. From the tables, the excess of protons due to nuclear interactions, when compared with antiprotons, is clear.

We use two different statistical methods to separate the electrons and kaons in the overlap region. In the first method, we examine the histogram of the number of particles in the overlap region, 1.2 < A < 1.5, as a function of momentum. We fit the electron background to determine the number of particles in the kaon and proton peaks (See Fig. 6.5). In the second method, we plot the number of kaons in each slice in A, integrated over the whole momentum range, and then fit a smooth curve through the points to determine the number of kaons in the overlap region. Figure 6.6 shows the plot of the number of kaons as a function of A used in this method. Both of these methods were checked with Monte Carlo distributions. The numbers of kaons obtained with the two methods are equal within errors.

The number of antiprotons is too small for either of these statistical procedures to be used. We thus only identify antiprotons below 1 GeV/c where their dE/dx is greater than that of electrons. The raw number of particles in each momentum bin is given in table 6.4. The kaon numbers are the average of the numbers from the two methods in the electron overlap region. The errors include both statistical and systematic effects. The systematic errors are due to uncertainties in the electron-kaon separation in the overlap region and to uncertainties in the tails of the pion distribution affecting the pion-kaon separation in the two highest momentum

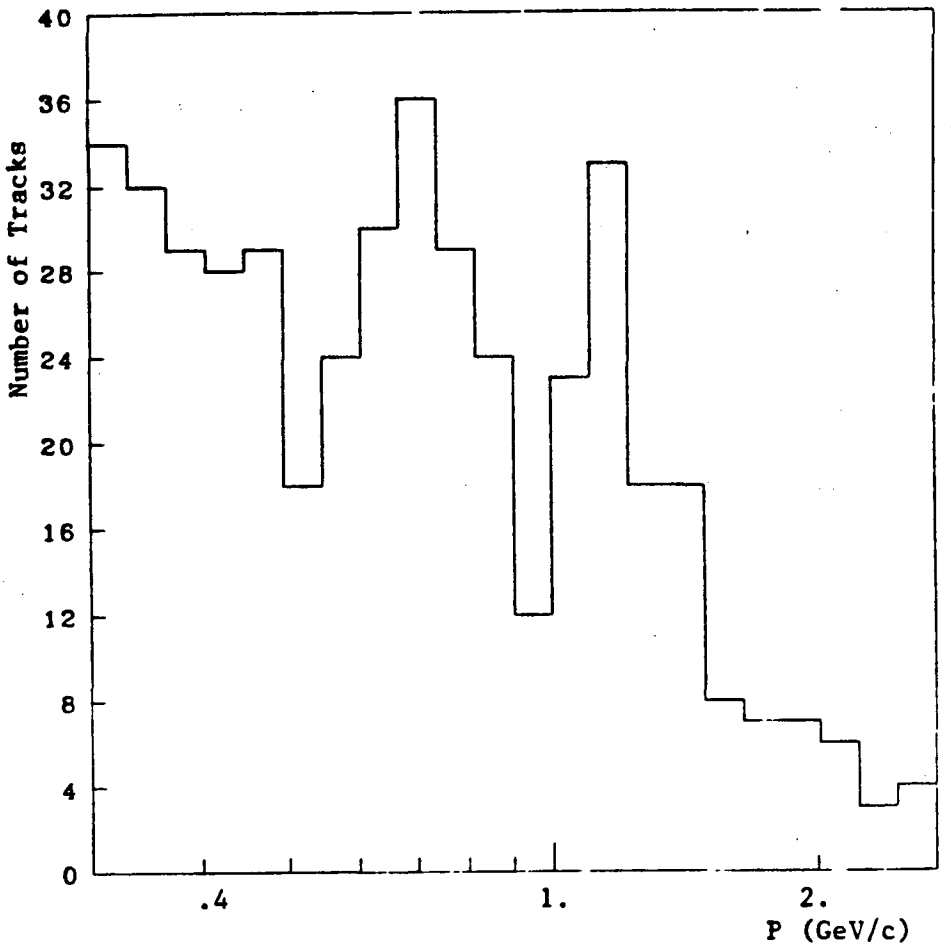

Figure 6.5

Number of Particles *vs.* Momentum— Electron Overlap region

The peak in the number of tracks at 700 MeV/c is due to kaons.

The peak in the number of tracks at 1.2 GeV/c is due to protons.

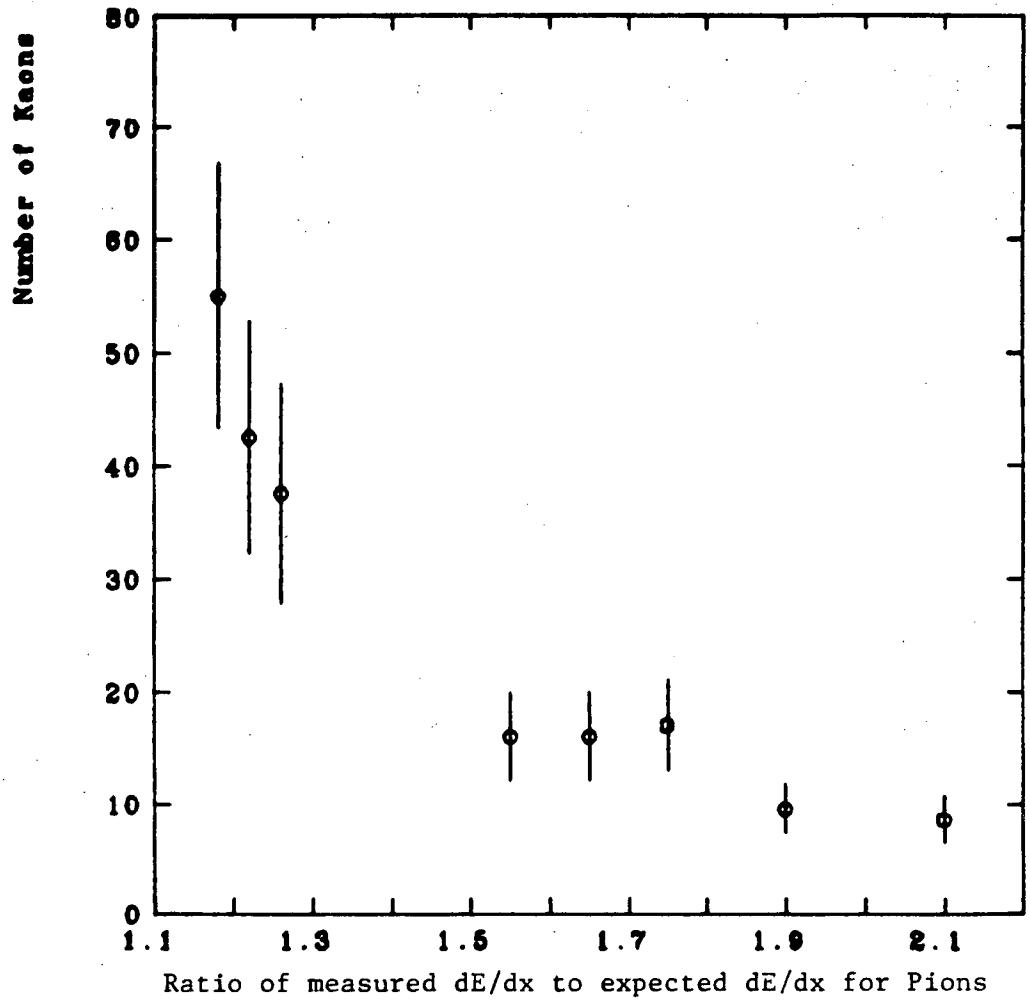

Figure 6.6

Number of Kaons *vs.* the Ratio of measured dE/dx to expected dE/dx for Pions

bins. The number listed in the pion column in the 952 MeV/c bin is the number of pions plus kaons, since, although protons can be identified in that momentum range, pions and kaons cannot be separated.

P (MeV/c)	$\pi^{\pm}$	$K^{\pm}$	$\overline{P}$
354	977 ± 31	41 ± 9	1 ± 1
452	660 ± 26	40 ± 8	4 ± 2
552	731 ± 27	47 ± 13	6 ± 2
674	710 ± 27	52 ± 12	4 ± 2
780	330 ± 18	36 ± 8	5 ± 2
862	290 ± 21	50 ± 14	3 ± 2
952	323 ± 18	-	7 ± 3

Table 6.4. Raw Particle Numbers—Low Momentum Data

6.1.2 High Momentum Data

We divide the high momentum data into three momentum bins: 2.7 GeV/c < P < 3.7 GeV/c, 3.7 GeV/c < P < 5.0 GeV/c, and 5.0 GeV/c < P < 7.4 GeV/c. The low momentum limit is due to the overlap region in dE/dx in which the particle types cannot be separated. The high momentum limit is necessary because of poor momentum resolution which causes particle types to become confused again above 7.5 GeV/c.

We determine the number of pions in the high momentum data by fitting a sum of gaussians to the distribution of the number of particles as a function of the ratio of measured dE/dx to dE/dx expected for a pion in the chosen momentum bin. We use the ratio because the momentum bins are wide enough that the expected values of dE/dx for the various particle types change appreciably within the bins. The ratios, however, are predicted to remain constant. The momentum bins are wide to ensure enough tracks in each bin. Figure 6.7 shows such a distribution for particles from 2.7 GeV/c to 4.0 GeV/c. The main pion peak and a secondary peak or shoulder due to kaons and protons are clearly visible. The dashed line on the plot is a

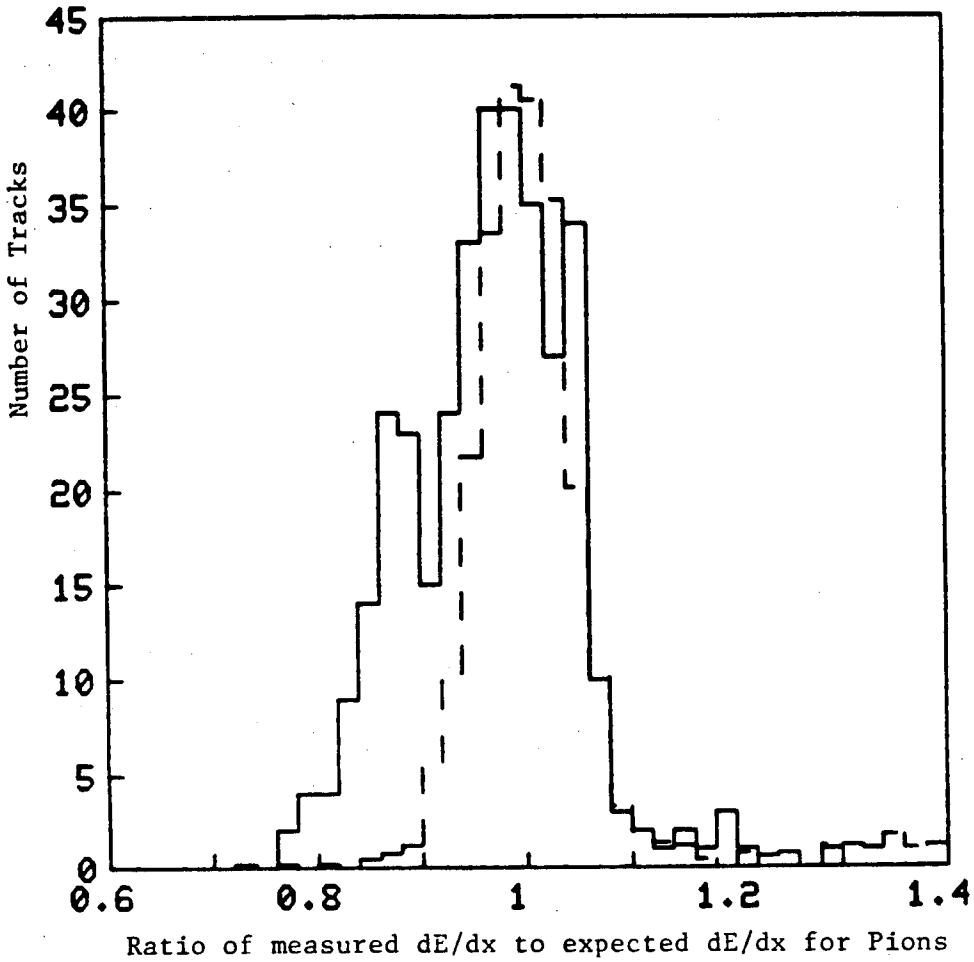

Figure 6.7

Ratio of Measured dE/dx to Expected dE/dx for Pions.

Solid Line: All tracks with 2.7 GeV/c < P < 4.0 GeV/c.

Dashed Line: All tracks with 450 MeV/c < P < 740 MeV/c.

superposition of the data from minimum ionizing pions. In order to increase the effective dE/dx resolution, all tracks used in the high momentum data are required to have a minimum of 120 good wires associated with them. Unfortunately, kaons and protons are not visibly separated in figure 6.7. This is as expected, since the calculated kaon–proton separation is only 1.3σ, and the amount of data is not sufficient for the broadening of the secondary peak due to the presence of two particle types to be noticeable. We have typically fitted the distributions to the sum of two gaussians, keeping the widths of the gaussians fixed. The raw pion and kaon + proton numbers from the fits are insensitive to changes in the widths of the gaussians within the limits set by the measured resolutions for Bhabha electrons and pions at minimum, including the effects of increased widths due to smearing caused by the finite momentum resolution. The positions of the pion and kaon + proton peaks agree with the expected positions determined from the Monte Carlo. The chi-squareds obtained from fitting three gaussians are the same as those obtained from fitting two gaussians. The raw pion and kaon + proton numbers obtained from the two methods agree.

P (GeV/c)	Pions	Kaons + Protons
3.13	185 ± 16	79 ± 12
4.23	96 ± 12	53 ± 12
5.92	66 ± 10	50 ± 9

Table 6.5. Raw Particle Numbers—High Momentum Data

In these high momentum bins, the numbers of positively and negatively charged particles are equal within errors. The number of protons produced at high momentum by nuclear interactions is expected to be small both because of kinematics and because there are many fewer high momentum particles than low momentum particles. In table 6.5, we therefore list the raw number of particles for both charges combined. The momentum values given in table 6.7 are the mean momenta of the particles in the three bins.

6.2 Particle Fractions

6.2.1 Acceptance Corrections Dependent on Particle Species

In order to calculate the particle fractions, we must correct the raw particle numbers for those acceptance effects which are different for the different particle types. These effects are: pion and kaon decay, nuclear interactions which preferentially absorb antiprotons, positive and negative kaons while producing pions, and differing energy loss for the different particle types in the material before the TPC. This energy loss causes very low momentum particles to stop before they reach the TPC.

We correct for these effects by examining the acceptance for single tracks using the PEP-4 GLOBAL Monte Carlo. The GLOBAL Monte Carlo includes an extremely sophisticated model of PEP-4. Its output is in the form of simulated TPC raw data which can then be analyzed with the same programs used to analyze the real data. It includes the effects of energy loss, bremstrahlung, pair production, and delta ray production in the material before the TPC as well as in the TPC gas itself. Nuclear interactions are simulated using the measured absorption cross sections for the various particle types. Reaction products are generated using a phase space production model. All reaction products, delta rays, ..., are tracked until they either lose all their energy or leave the PEP-4 volume. The TPC raw data is simulated on a wire by wire, CCD bucket by CCD bucket level, including such effects as ionization fluctuations and diffusion in the TPC gas.

Such a detailed Monte Carlo is ideal for studying detector acceptance. When the simulated raw data output of the GLOBAL Monte Carlo is run through the data analysis programs, complicated effects, such as the fraction of kaon decays in the TPC gas in which the pattern recognition program successfully finds two tracks, are accounted for automatically. The

one drawback to the GLOBAL Monte Carlo is that it is very slow. (A single multihadron event takes about 3 minutes of CPU time to produce in the computer used for the PEP-4 analysis.) For this reason, we rely on the GLOBAL Monte Carlo to determine the acceptance for single tracks, and then use the TPCLUND Monte Carlo to correct for the effects of track overlap in the true multitrack environment, as well as to calculate event acceptance.

The momentum given in all previous graphs and figures is the particle's momentum in the TPC, because this momentum determines the particle's measured energy loss by dE/dx. To determine the vertex momentum, we correct for energy loss in the material before the TPC using the average difference between the particle's momentum at the vertex and its measured momentum in the TPC, as given by the Monte Carlo. (For example, minimum ionizing pions lose $\approx$ 17 MeV/c from the vertex to the TPC. A 552 MeV/c kaon at the vertex loses $\approx$ 30 MeV/c before reaching the TPC, while a 552 MeV/c proton loses $\approx$ 75 MeV/c before reaching the TPC.)

In figures 6.7, 6.8, and 6.9, we show the acceptance for pions, kaons, and antiprotons as a function of vertex momentum. The acceptances were calculated by generating single tracks at a fixed angle with respect to the beam direction ($\theta = 60°$) and at random azimuths with GLOBAL. (As defined previously, the angle, θ, is given by $cos\theta = z/\sqrt{x^2+y^2+z^2}$ and the azimuthal angle, ϕ, is given by $\sin\phi = y/\sqrt{x^2+y^2}$.) Because both GLOBAL and TPCLUND simulate the effects of sector boundaries, the acceptances in figures 6.7–6.9 were normalized to the muon acceptance as obtained from GLOBAL. This was done so that when corrections to the acceptance for geometrical effects, track overlap, sector boundaries,..., are applied, the sector boundaries are not counted twice. The single track muon acceptance obtained from GLOBAL for tracks with more than 80 good wires was constant and equal to $94.3 \pm .6$ %, independent of momentum for P $\geq$ 350 MeV/c. This value is consistent with that obtained from TPCLUND. Nuclear interactions and decays of charged pions and kaons are not included in TPCLUND,

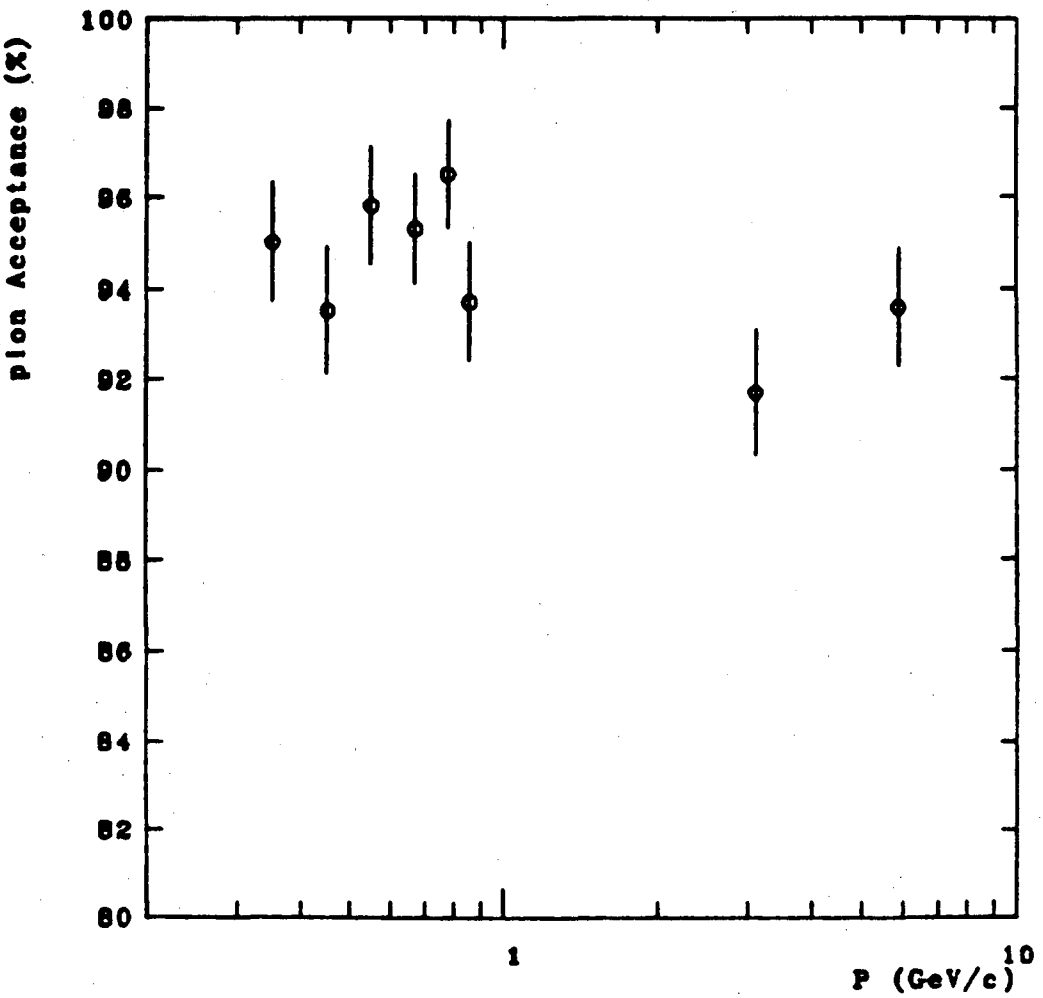

Figure 6.8. Pion Acceptance *vs.* Vertex Momentum

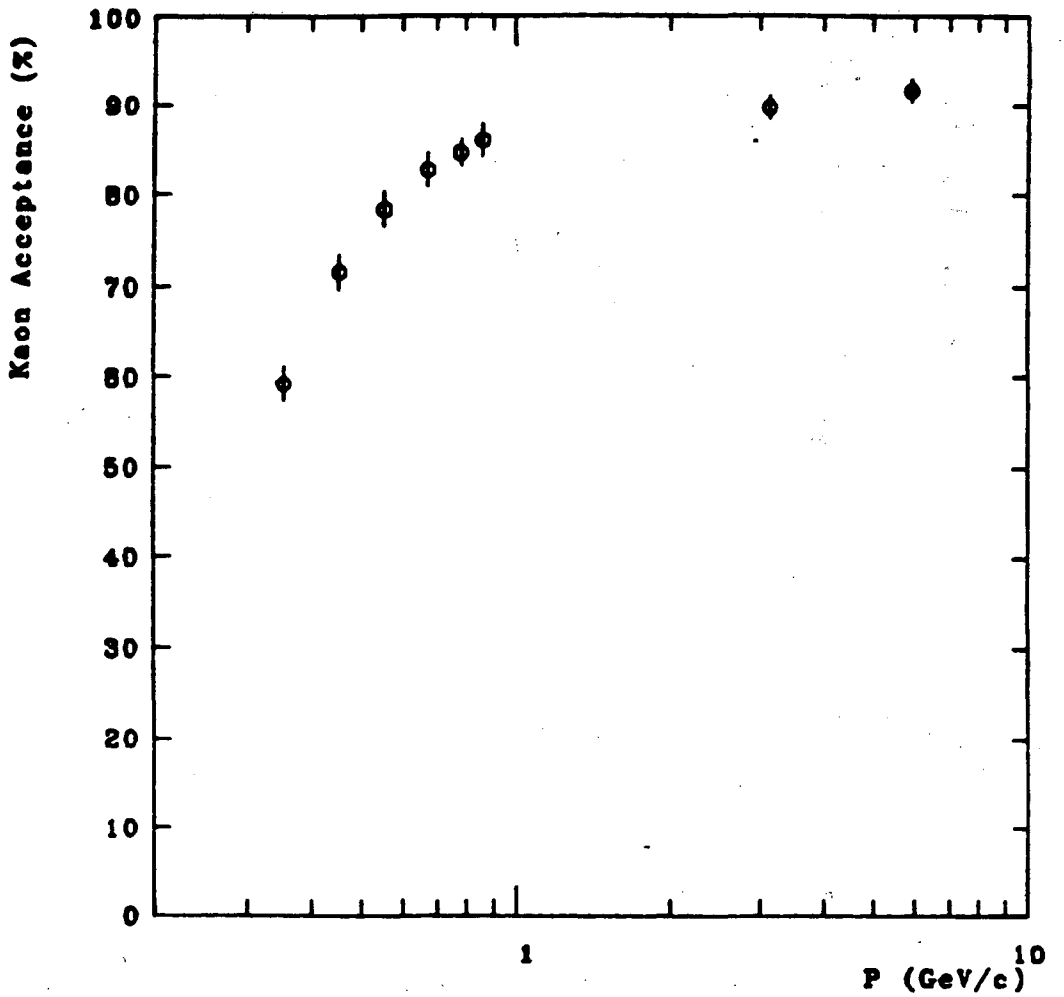

Figure 6.9. Kaon Acceptance *vs.* Vertex Momentum

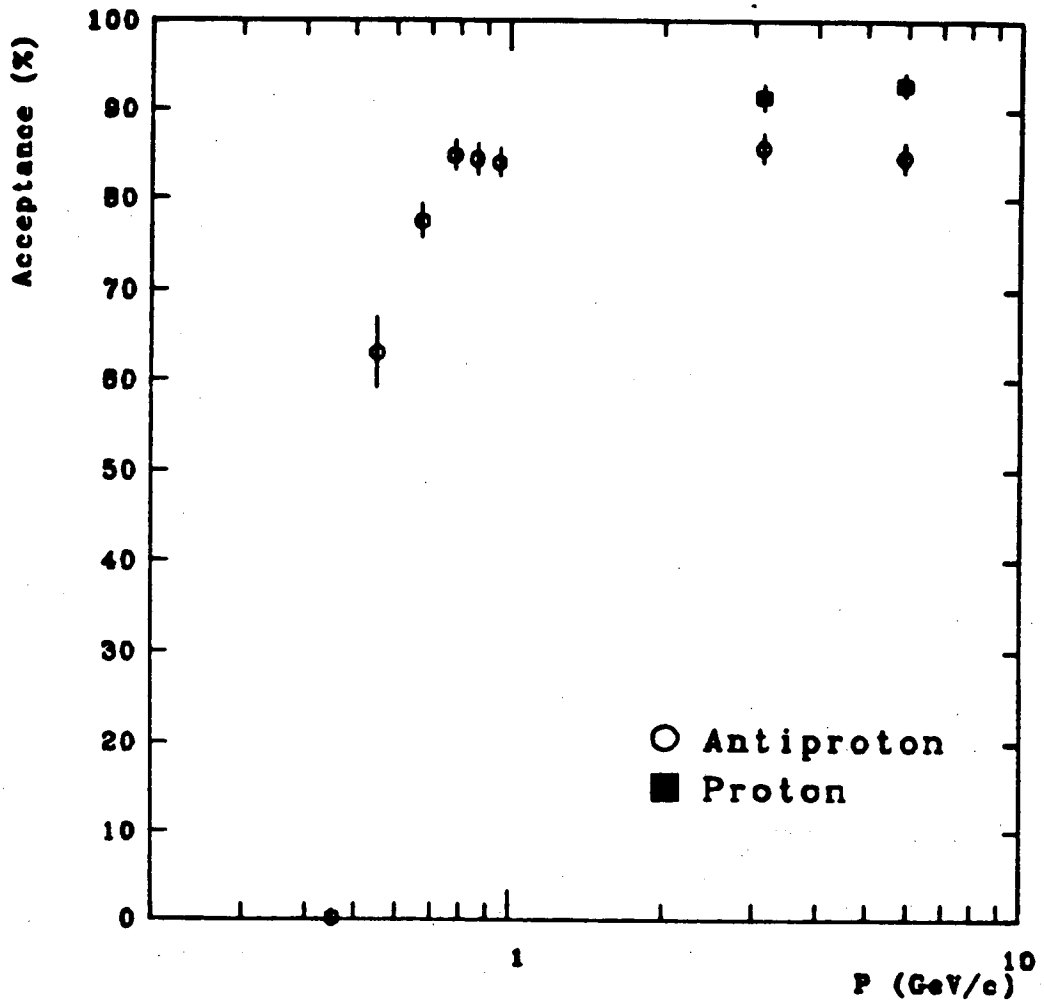

Figure 6.10. Antiproton Acceptance *vs.* Vertex Momentum

where, therefore, charged hadrons are treated identically to muons except for different energy loss due to different masses. The number of pions produced by interactions and the number of muons produced by decays (the two are indistinguishable using dE/dx) were obtained from the same Global Monte Carlo events used in determining the acceptances. These numbers were small compared with the statistical error on the number of pions in each bin in tables 6.4 and 6.5. The pion acceptance is above 91% for all data points (see Fig. 6.7) and is relatively flat. We assign a systematic error of 3% to the pion single track acceptance at all momenta, where the 3% includes the uncertainty in the corrections for pions produced in interactions before the TPC as well. The number of pions is also corrected for direct muons (from charm and bottom decays) based on the results from the TPCLUND Monte Carlo. This correction is small compared with the statistical error on the number of pions in any given bin. The Monte Carlo results agree with our measurements of direct muons, which can only be made above 2 GeV/c where the muon chambers are efficient .

We assign the kaon and antiproton acceptances systematic errors ranging from 15% in the lowest momentum bins, where the acceptance is changing rapidly, to 4% in the higher momentum bins, where the acceptance is relatively constant. In the high momentum region ($P > 2$ GeV/c), we use the average of the $K^{\pm}$ and $P^{\pm}$ acceptances for the combined kaon and proton acceptance. We assign the acceptance an error of 4%. Above 2 GeV/c, the proton and antiproton acceptances differ by a maximum of 8%. The average of the proton and antiproton acceptances differs from the kaon acceptances by less than 3%.

This method of making the acceptance corrections by first using the GLOBAL Monte Carlo to correct for decays and nuclear interactions, making the different particle types equivalent, and then using the TPCLUND Monte Carlo to make all other acceptance corrections, is certainly not ideal. It does, however, provide for realistic corrections within the limits imposed by computer time, and is sufficiently accurate for the present data.

P (GeV/c)	$\pi^{\pm}$	$\pi^{\pm} + K^{\pm}$	$K^{\pm}$	$2\overline{P}$	$K^{\pm} + P^{\pm}$
0.354	1004 ± 44	-	52 ± 19	-	-
0.452	704 ± 34	-	64 ± 13	-	-
0.552	766 ± 36	-	64 ± 18	22 ± 9	-
0.674	759 ± 37	-	64 ± 15	18 ± 7	-
0.780	353 ± 21	-	40 ± 10	12 ± 5	-
0.862	313 ± 23	-	57 ± 16	10 ± 5	-
0.952	-	342 ± 30	-	16 ± 6	-
3.13	193 ± 13	-	-	-	89 ± 14
4.23	97 ± 13	-	-	-	59 ± 11
5.92	67 ± 10	-	-	-	55 ± 10

Table 6.6. Particle Numbers Corrected for Decays and Nuclear Interactions

6.2.2 Backgrounds

We estimated in chapter 5 that there are 3.2% $\tau\overline{\tau}$ events, 2.0% two photon events, 2.8% cosmic ray junk events, and less than 1% beam gas events in our multihadron sample. The reason that the cosmic ray junk events pass our multihadron selection cuts, which require 5 tracks, is that they contain noise tracks due to oscillations in the electronics that appear in coincidence with the cosmic rays. Noise tracks are normally rejected, because no wires can be associated with them. For the events that pass the cuts, the noise tracks and the cosmic ray tracks are in the same sectors and within ± 3 cm in z. The wire hits from the cosmic ray tracks are then labelled ambiguous, since they could be assigned to either the (real) cosmic ray tracks or the (fake) noise tracks. Ambiguous wires are not used in the dE/dx determination, and tracks from these events are removed from our sample by the 80 wire and 120 wire requirements. The remaining background consists of $\approx$ 6% of the events. Since these events tend to have low multiplicities, and since the average charged multiplicity is $\approx$ 12, we estimate the number of background tracks to be $\approx$ 3%.

The corrected particle numbers are given in table 6.6. The corresponding particle

P (GeV/c)	Fr($\pi^{\pm}$)	Fr($K^{\pm}$)	Fr($2\bar{P}$)	Fr($K^{\pm}+P^{\pm}$)
0.354	$.94 \pm .02$	$.05 \pm .02$	-	-
0.452	$.91 \pm .02$	$.07 \pm .02$	-	-
0.552	$.90 \pm .02$	$.07 \pm .02$	$.026 \pm .011$	-
0.674	$.90 \pm .02$	$.08 \pm .02$	$.021 \pm .008$	-
0.780	$.87 \pm .03$	$.10 \pm .02$	$.029 \pm .013$	-
0.862	$.82 \pm .04$	$.15 \pm .04$	$.026 \pm .013$	-
0.952	-	-	$.045 \pm .017$	-
3.13	$.68 \pm .04$	-	-	$.32 \pm .04$
4.23	$.62 \pm .05$	-	-	$.38 \pm .05$
5.92	$.55 \pm .06$	-	-	$.45 \pm .06$

Table 6.7. Particle Fractions

fractions are given in table 6.7 and are plotted in figure 6.11. In the 354 MeV/c momentum bin and the 452 MeV/c momentum bin, we have assumed that twice the antiproton fraction equals $1 \pm 1\%$ in order to calculate the pion and kaon fractions. Our antiproton acceptance in those momentum bins is essentially zero, since the antiprotons lose too much energy to reach the TPC. The errors include both statistical and systematic uncertainties added in quadrature. For both kaons and antiprotons, the statistical errors dominate. The pion fraction decreases from above 90% at low momentum to $\approx$55% at 6 GeV/c.

Results on the particle fractions obtained at similar center of mass energies from the TASS0 and DELCO experiments made using time-of-flight counters and Cerenkov detectors to identify particles, are given in figures 6.11 and 6.12. Our results are in general agreement with these other experiments, although our pion fractions are larger than TASSO's and our kaon fractions smaller. Our results were obtained using a different technique (dE/dx) than the other experiments, and, therefore, provide an independent measurement of the particle fractions with different systematic errors.

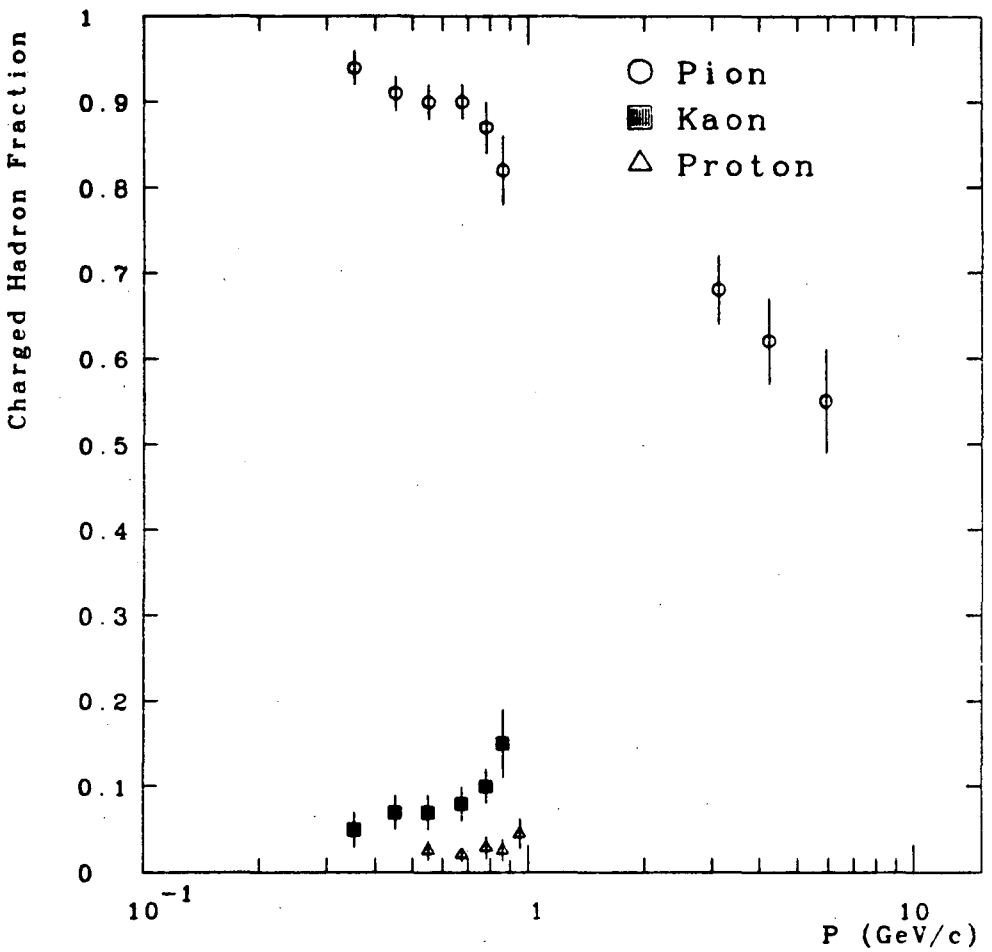

Figure 6.11. Charged Particle Fractions *vs.* Momentum— $\sqrt{s} = 29$ GeV.

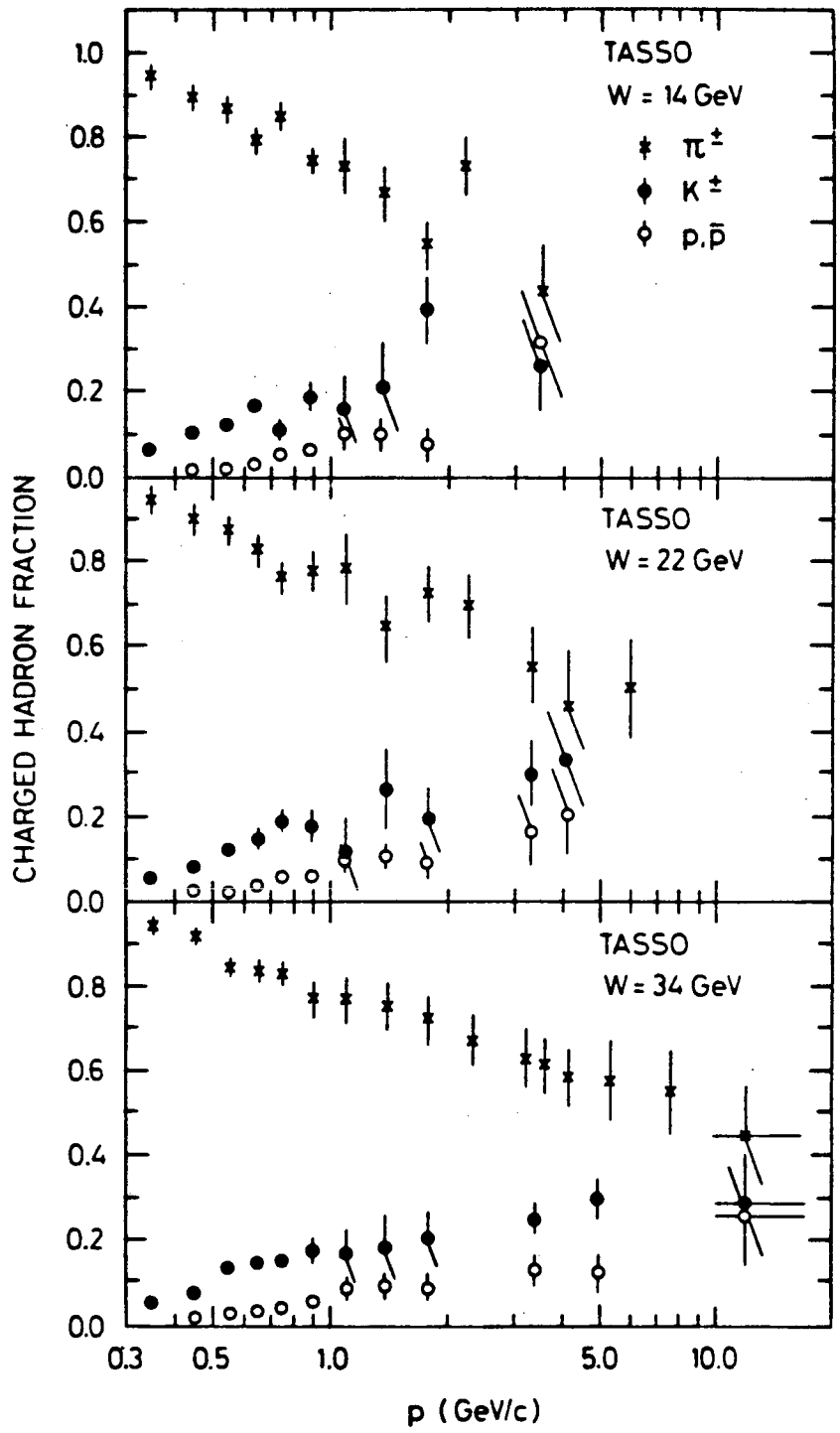

Figure 6.12

Charged Particle Fractions *vs.* Momentum

$\sqrt{s} = 34$ GeV TASSO Experiment [Althoff 82]

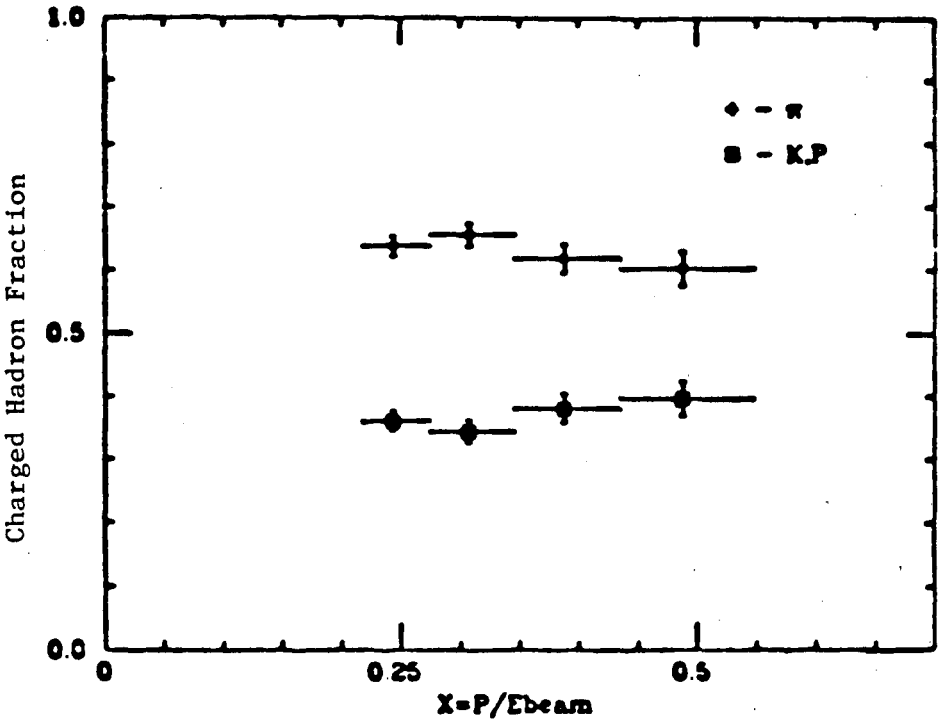

Figure 6.19

Charged Particle Fractions *vs.* Momentum

$\sqrt{s} = 29$ GeV DELCO Experiment [Atwood 82]

6.3 Differential Cross Sections

To calculate the differential cross section, $\frac{1}{\beta}\frac{d\sigma}{dx}$, for the different particle types, it is first necessary to correct the particle numbers given in table 6.6 for geometrical acceptance losses caused by track overlap, sector boundaries, and the 80 and 120 good wire cuts. The geometrical acceptance as determined from the TPCLUND Monte Carlo is ($\approx 70 \pm 6$)% for particles with momenta below 1 GeV/c and is ($\approx 32 \pm 4$)% for particles above 1 GeV/c. To conform with the cuts made on the data, 80 wires were required on tracks in the momentum bins below 1 GeV/c and 120 wires on the tracks in the momentum bins above 1 GeV/c. This is the cause of the large decrease in acceptance above 1 GeV/c. For a fixed wire cut, the acceptance decreases slightly with increasing momentum, because high momentum tracks tend to stay closer to the center of a jet and are more affected by track overlap. We assign the systematic errors to these acceptances by varying the particle production model and estimating the uncertainties in assigning the correct number of wires to each track.

The particle numbers are corrected for the loss of tracks due to pattern recognition inefficiencies. The pattern recognition efficiency, as obtained from scanning the events, is (95 ± 5)%.

Since only those events with 5 or more charged tracks were accepted in this analysis, there is a bias in the momentum distributions because low charged multiplicity events have been removed from the sample. These low multiplicity events tend to have more high momentum tracks and fewer low momentum tracks. We corrected for this effect by using the LUND Monte Carlo to study the effects of the event selection cuts. The number of particles in any momentum bin was not changed by more than 3% in making this correction.

We studied the effects of momentum resolution biases on the high momentum data ($P > 2$ GeV/c) using the Monte Carlo. The effects of momentum smearing on the number of

particles in each bin were small except in the highest momentum bin. An additional systematic error of 10% was added to the error on the data in this bin.

The number of events used in measuring the particle fractions and differential cross sections is not the same as that used for the total cross section measurements, since we have added events from data taken when the poletip calorimeters were off in order to increase statistics. For the luminosity in the determination of the total cross section, we then use the total number of events, 1433, divided by the measured total cross section, $\sigma = .38$ nb.

$x_\pi = E_\pi/E_{Beam}$	$s/\beta\ d\sigma/dx_\pi$ μbarn GeV^2	$x_K = E_K/E_{Beam}$	$s/\beta\ d\sigma/dx_K$ μbarn GeV^2	$x_P = E_P/E_{Beam}$	$s/\beta\ d\sigma/dx_P$ μbarn GeV^2
.023—.030	49.2 ± 5.3	.040—.044	6.5 ± 2.5	.073—.077	3.7 ± 1.5
.030—.036	39.3 ± 4.3	.044—.048	7.2 ± 1.6	.077—.082	1.8 ± 0.7
.036—.043	35.0 ± 3.9	.048—.054	4.9 ± 1.4	.082—.086	1.8 ± 0.9
.043—.052	28.7 ± 3.2	.054—.061	3.6 ± 0.9	.086—.090	1.2 ± 0.6
.052—.057	23.0 ± 2.7	.061—.066	3.5 ± 0.9	.090—.095	1.6 ± 0.6
.057—.063	18.7 ± 2.4	.066—.071	4.4 ± 1.2	-	-
.19—.25	2.11 ± 0.34	-	-	-	-
.25—.34	0.72 ± 0.13	-	-	-	-
.34—.51	0.37 ± 0.09	-	-	-	-

Table 6.8. Differential Cross Sections at $\sqrt{s} = 29$ GeV.

The differential cross sections, $\frac{s}{\beta}\frac{d\sigma}{dx}$, for the different particle types are shown in figure 6.14. The cross sections are also listed in table 6.8. The errors listed in table 6.14 include both the statistical and systematic uncertainties added in quadrature. The errors do not include the 10% uncertainty in the overall normalization due to the uncertainty in the total cross section. Plots of the scaled differential cross sections, $\frac{1}{\sigma\beta}\frac{d\sigma}{dx}$, for pions, kaons, and protons are given in figures 6.15, 6.16, and 6.17 for both our results and the results of the TASSO experiment [Althoff 82]. When we divide the differential cross sections by the total cross section, σ, differences in the measurements of the total cross section between the two experiments cancel. As can be seen from the plots, our pion data are in good agreement with the results from TASSO, but we measure

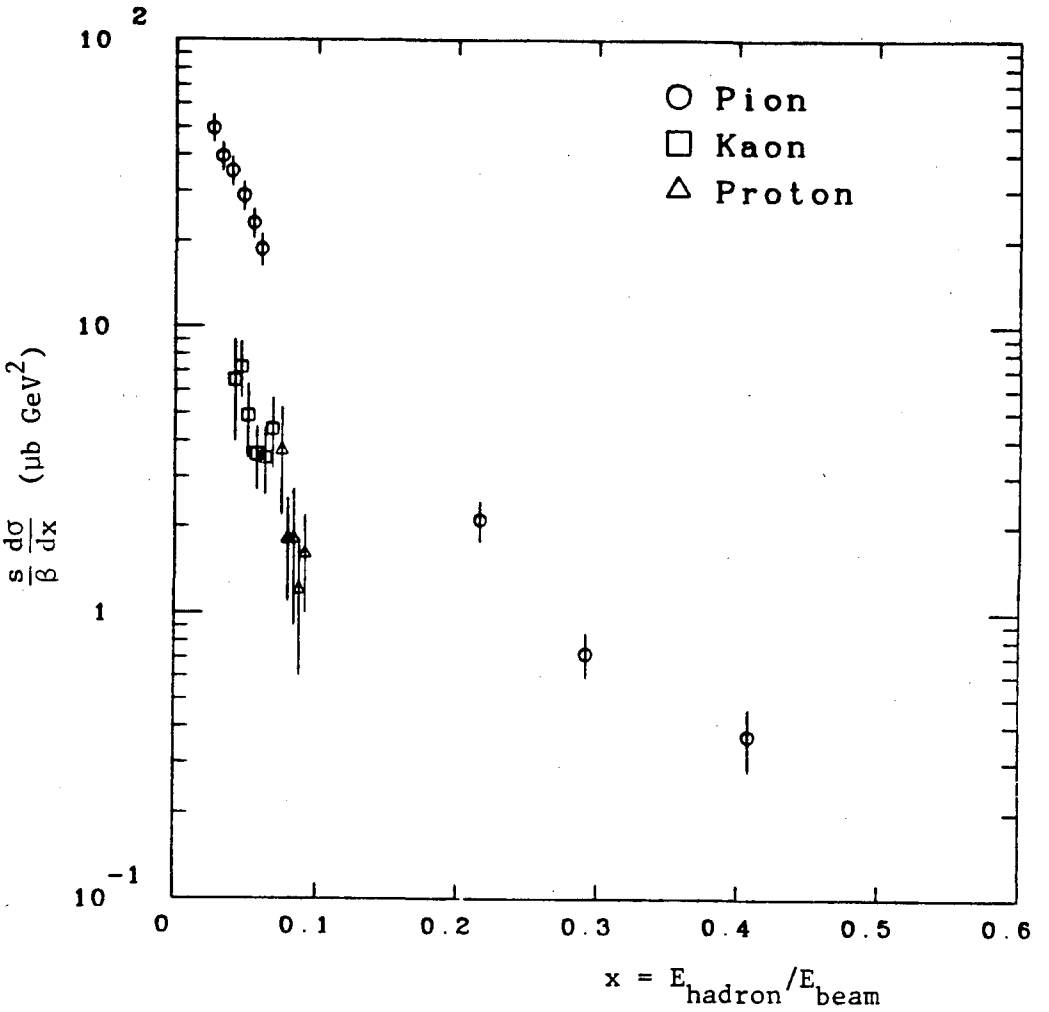

Figure 6.14

Differential Cross Section ($s/\beta\ d\sigma/dx$) *vs.* x at $\sqrt{s} = 29$ GeV for pions, kaons, and protons. Twice the antiproton cross section is used for the proton plus antiproton cross section.

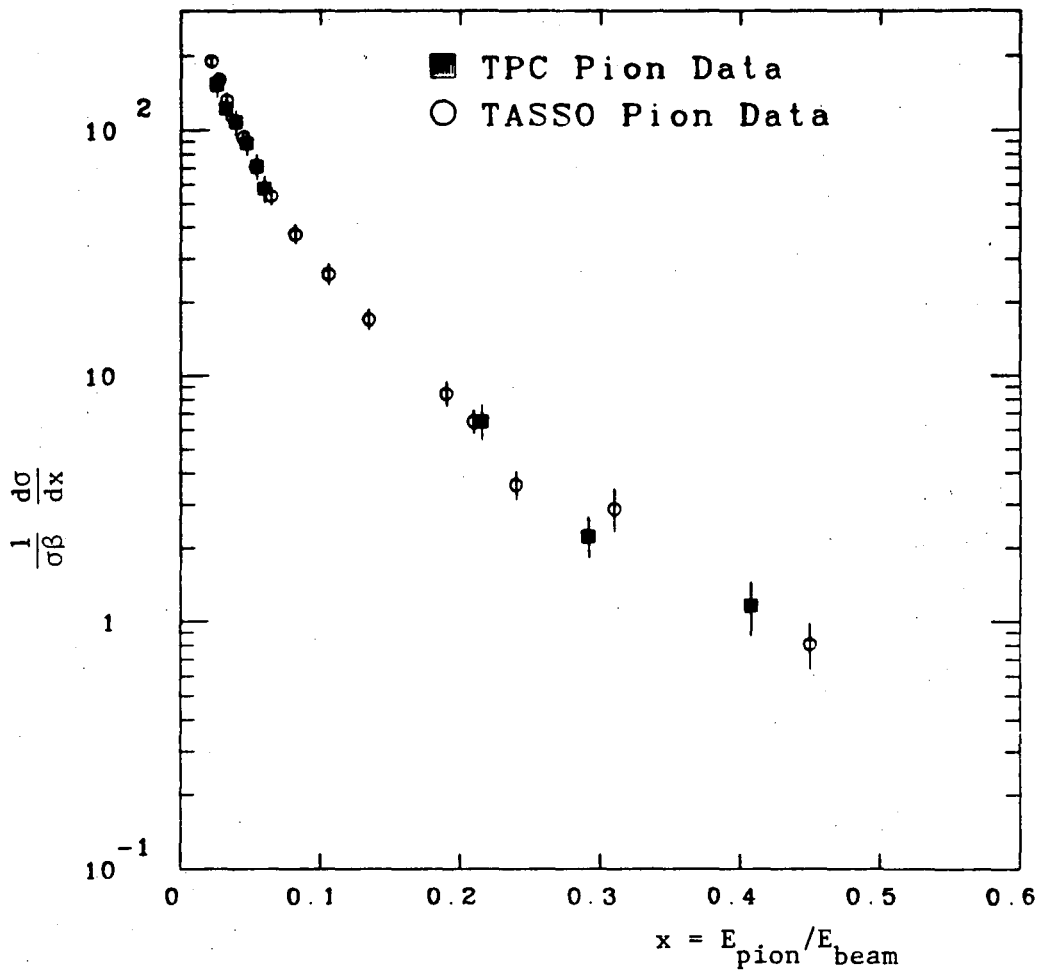

Figure 6.15

Scaled Cross Section ($1/\sigma\beta$ dσ/dx) *vs.* x

for Pions—This Experiment and TASSO Experiment

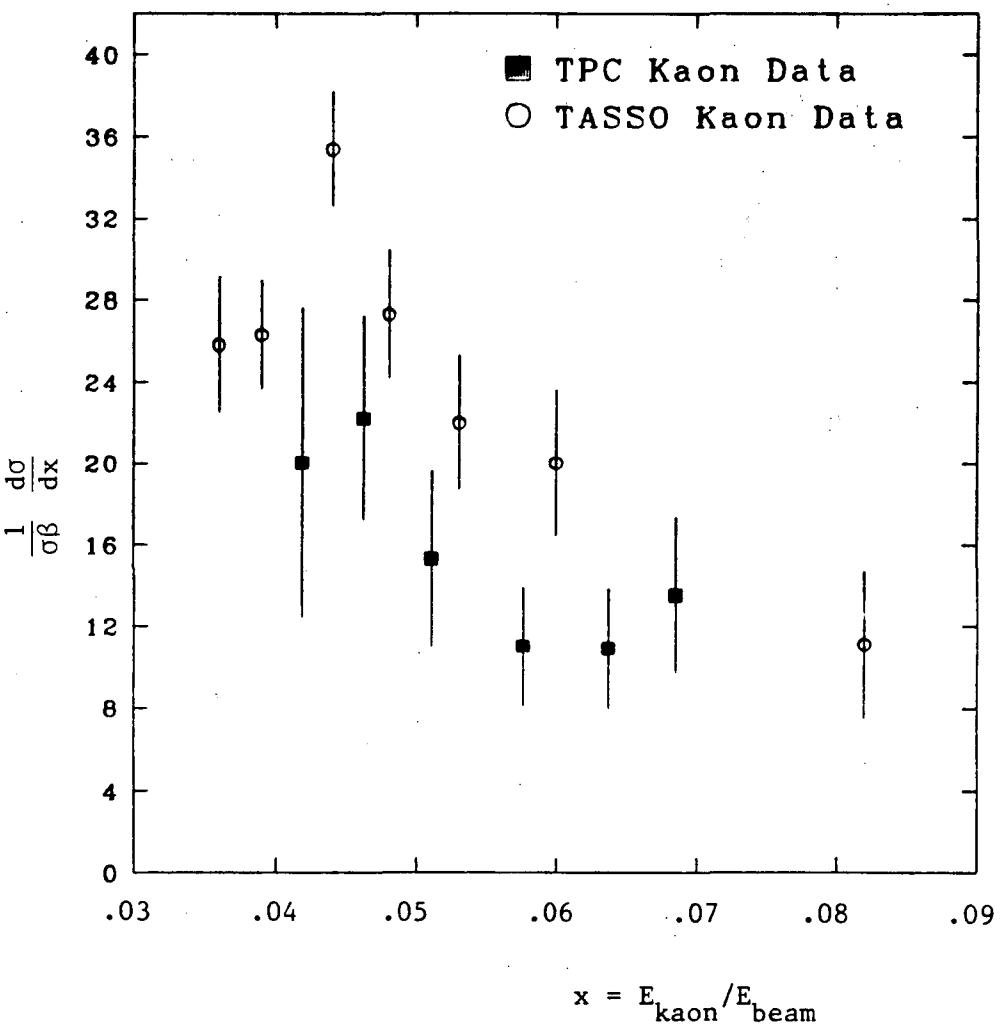

Figure 6.16

Scaled Cross Section ($1/\sigma\beta\ d\sigma/dx$) *vs.* x

for Kaons—This Experiment and TASSO Experiment

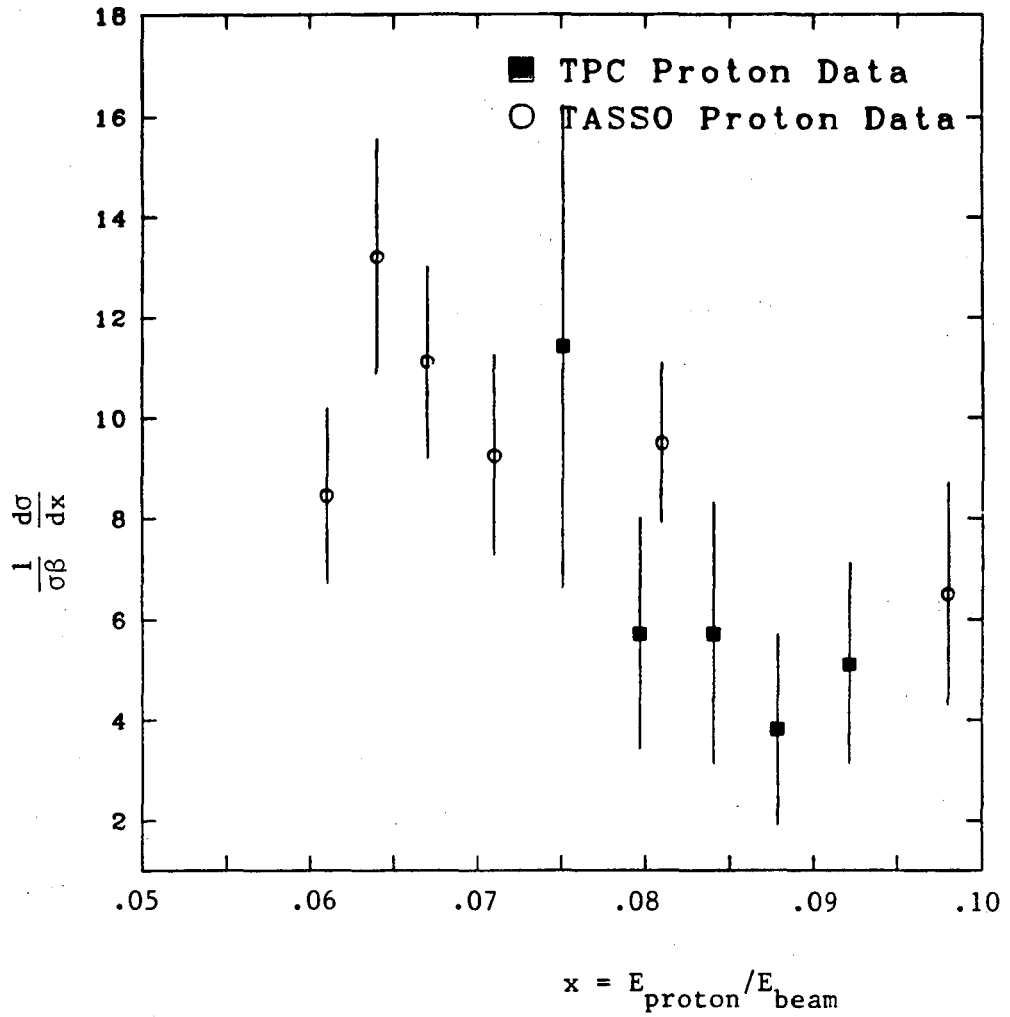

Figure 6.17

Scaled Cross Section ($1/\sigma\beta\ d\sigma/dx$) *vs.* x

for Protons—This Experiment and TASSO Experiment

significantly fewer kaons and protons. Our results, when scaled by the given fractions, are in reasonable agreement with those of other experiments where the differential cross section, $\frac{1}{\beta}\frac{d\sigma}{dx}$, has been measured for all particles combined. (See, for example, Patrick 82.)

6.4 Interpretation

We will use the measured cross sections and particle fractions to study the process of hadronization within the quark parton model. We will first discuss the kaon results and their implications for strange quark production, and then the (anti)proton results and models of baryon production.

6.4.1 Strange Particle Production

In the quark parton model, the e^+e^- pair first annihilate into a virtual photon. The virtual photon then produces a quark and an antiquark which dress themselves into hadrons by pulling $q\bar{q}$ pairs out of the vacuum. In order to account for the observed number of kaons, we begin with those kaons produced directly from primary $s\bar{s}$ quarks. Of our 1433 events, we expect $\frac{1}{3}/\frac{11}{3} = \frac{1}{11}$ of them to be $e^+e^- \rightarrow s\bar{s}$ events. Each $s\bar{s}$ event has two strange quarks. Assuming the number of charged and neutral kaons to be equal, we expect 1 K^+ or K^- per $s\bar{s}$ event for a total of 1433/11 = 130 charged kaons over all momenta. In the momentum interval from 300 MeV/c to 900 MeV/c, we observed more than 300 kaons. The number of kaons from $e^+e^- \rightarrow s\bar{s}$ events is,therefore, clearly too small to account for all those seen in the data.

The next possible source of kaons is charm and bottom decays in $c\bar{c}$ and $b\bar{b}$ events. Since not all of the charm meson branching fractions and almost none of the bottom meson branching fractions have been measured, estimates of the number of $K^{\pm}$ from charm and bottom decays depend on the particular model used for the decays. We will compare our data with the

predictions of the LUND particle generator. The LUND branching fractions for those particles ($D^{\pm}$,D^0) whose branching ratios have been measured either agree with the experimental data or predict more $K^{\pm}$ than have been observed. The LUND Monte Carlo prediction for the scaled differential cross section, $\frac{1}{\sigma\beta}\frac{d\sigma}{dx}$, for kaons with the probability of pulling $s\bar{s}$ pairs from the vacuum set to 0 is shown in figure 6.18 along with our data. The theoretical prediction for the kaon fraction clearly lies below our data points, and a significant fraction of the observed kaons must be due to production of $s\bar{s}$ pairs from the vacuum during the hadronization process, despite the larger mass of the strange quark relative to the up and down quarks.

In the LUND model (and in most other hadronization models) there is a parameter which gives the probability for an $s\bar{s}$ quark antiquark pair to be pulled from the vacuum relative to a light quark antiquark ($u\bar{u}$ or $d\bar{d}$) pair. The determination of this parameter is complicated by the existence of other parameters which also affect the observed kaon fraction and cross section. The most important of these parameters are the probabilty for a produced meson to be a vector or scaler particle and the parameter c, which controls the shape of the fragmentation function, D(z). In the LUND model, $D(z) = (1+c)(1-z)^c$, and the standard values for c and P(V), the probability of a produced meson being a vector particle, are both 0.5 [Sjostrand 82]. The value of the total charged multiplicity depends on both P(V) and c, and our measurement of this quantitity, therefore, can only determine allowed ranges of P(V) and c.

The best way to determine these model parameters would be to measure the cross section for the production of a vector meson (eg. ρ, K^*, ϕ) and use that value along with the π and K cross sections as a function of x, and the total charged multiplicity to determine P(V), the shape of the fragmentation function, and the probability of producing an $s\bar{s}$ pair from the vacuum, simultaneously. Since we have not measured a vector meson cross section, or $\frac{s}{\beta}\frac{d\sigma}{dx}$ for kaons at high x, we are not able to do this. Instead, we note that the standard values of 0.5 for P(V) and c, set by the LUND group, give a result for the charged multiplicity that agrees

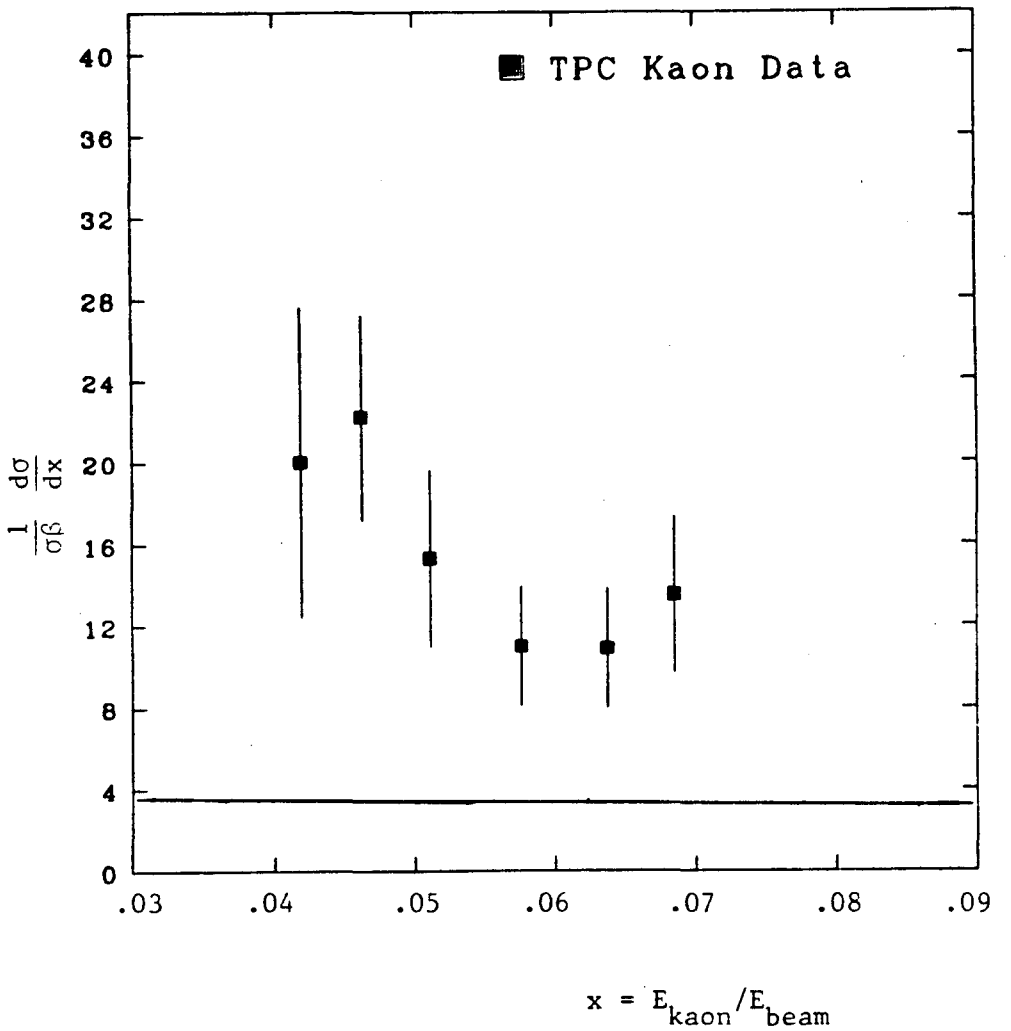

Figure 6.18

Scaled Differential Cross Section $(1/\sigma\beta\ d\sigma/dx)$ *vs.* x

Kaon Data

The curve is the prediction of the LUND Monte Carlo

with the probability of producing $s\bar{s}$ pairs from

the vacuum set to 0. The data points are from this experiment.

with the value measured by this experiment, 12.0, and that the value for P(V) agrees with a recent experimental determination of that parameter based on a measurement of ρ production [Brandelik 82b]. Assuming these standard values to be correct, we find that the ratio of the probability of $s\bar{s}$ quark antiquark production from the sea relative to that for $u\bar{u}$ production is given by:

$$\frac{\text{Prob}(s\bar{s})}{\text{Prob}(u\bar{u})} = .26 \pm .10. \tag{6.1}$$

The error includes both the statistical and systematic uncertainties. The systematic error was estimated by varying P(V) within the limits on that quantity set by the TASSO experiment, while at the same time varying c to keep the multiplicity constant. The systematic error also includes an estimate of the effect of the uncertainties in the bottom and charm branching ratios into kaons.

This value for the relative probability of strange quark production is model dependent, but it serves to indicate the size of the $s\bar{s}$ contribution from the sea during hadronization. It is in agreement with measurements of the same parameter by the JADE experiment and by the TASSO experiment. The JADE experiment [Komamiya 82] uses K^0s and the LUND Monte Carlo and finds $\text{Prob}(s\bar{s})/\text{Prob}(u\bar{u}) = .33 \pm .12$. The TASSO experiment uses a different model for hadronization based on a model of Feynmann and Field [Field 78] implemented by Hoyer and Ali [Hoyer 79, Ali 80]. TASSO [Wolf 83] finds $\text{Prob}(s\bar{s})/\text{Prob}(u\bar{u}) = 0.3 \pm 0.1$.

6.4.2 Baryon Production

Since baryons are heavy ($\approx$1 GEV/c^2) and are made of three quarks instead of simple $q\bar{q}$ pairs like mesons, we would naively expect fewer baryons to be produced than have been observed in e^+e^- annihilations at PEP energies. There are now a large number of models designed to account for the observed large amount of baryon production [Andersson 81, Hofmann 81, Meyer

81, Ranft 80, Ilgenfritz 78]. Most of these are based on the introduction of diquarks, qq and $\overline{qq}$ states which can be pulled from the vacuum in pairs. These qq and $\overline{qq}$ states then join with one member of a $q\overline{q}$ pair to form a baryon. Diquarks cannot be pointlike objects, since they would then contribute to a large increase in $R = \sigma(e^+e^- \rightarrow \text{hadrons})/\sigma(e^+e^- \rightarrow \mu^+\mu^-)$ which has not been observed. As described in chapter 2, one conceptually different approach uses only $q\overline{q}$ pairs from the vacuum and relies on the quark alignment in the color field to produce baryons [Casher 79].

Any of these models can be successfully tuned to fit our data on antiproton production. In terms of the diquark model, a good fit to our data is obtained with the value of the probability of diquark production relative to $q\overline{q}$ production, Prob($qq\ \overline{qq}$)/Prob($q\overline{q}$), equal to $\approx .07$ (see Fig. 6.19). Again, this statement is model dependent, but serves to indicate the relative order of magnitude for diquark production.

A more severe test of baryon production models should include the study of lambda cross sections as well as proton cross sections, so that details such as strangeness suppression in both baryon and meson formation can be examined. Additional information would be obtained by looking for baryon antibaryon correlations. For example, in the diquark model, the baryon and the antibaryon should normally be in the same jet.

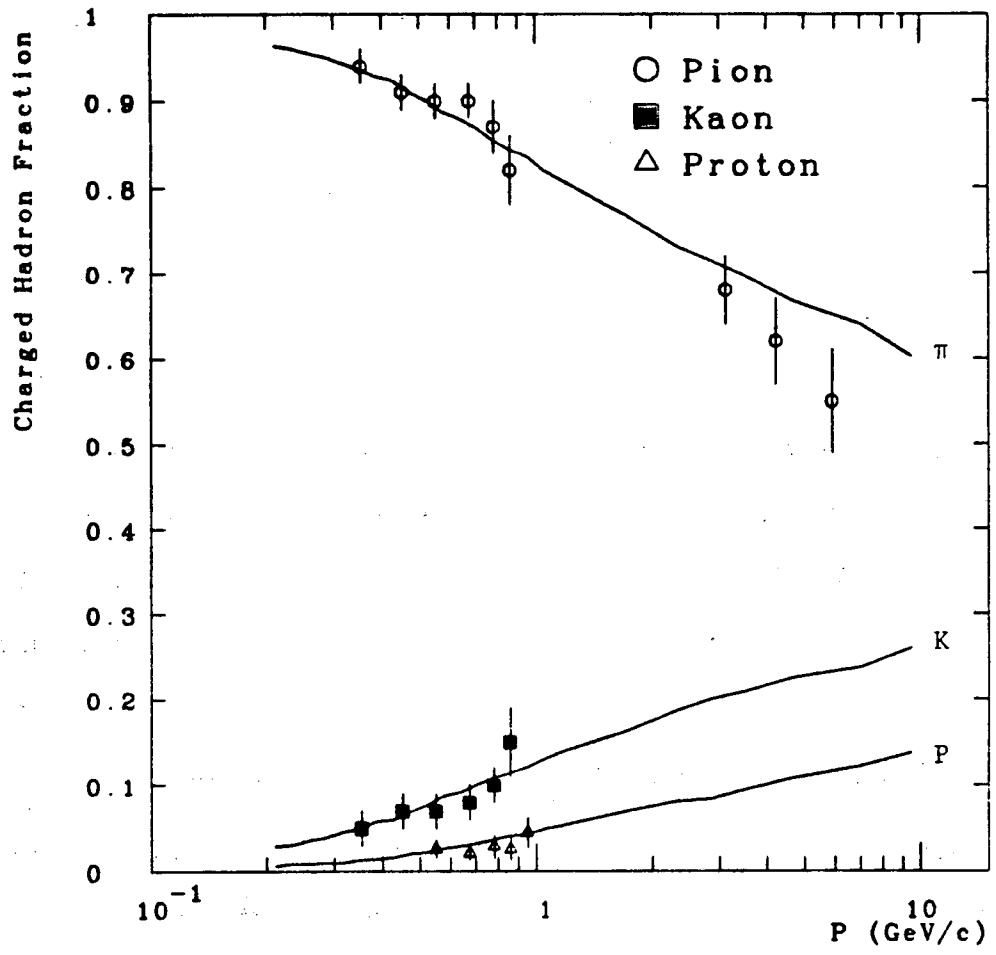

Figure 6.19

Pion, Kaon and Proton Particle Fractions—

The solid lines are the predictions of the LUND model with:

Prob($s\bar{s}$)/Prob($u\bar{u}$) = .30 and

the ratio of diquark production relative to $q\bar{q}$ production = .07

Chapter 7

Conclusion

We have measured the particle fractions and particle separated differential cross sections in e^+e^- annihilations using a new technique, particle identification by measurement of ionization energy loss (dE/dx). The pion fraction decreases from above 90% at 500 MeV/c to $\approx$ 55% at 6 GeV/c. We have also measured R, the ratio of the total hadronic cross section to the mu pair cross section. Our value for R is 3.7 with an uncertainty of 10%. This value is in agreement with the results of other experiments and with the predictions of the quark-parton model.

Given the relative simplicity of the initial state, e^+e^- collisions are an ideal tool for studying hadronization, the process by which quarks dress themselves into hadrons. We have shown that our results for kaon production can only be explained in terms of a large number of kaons having been produced by strange quarks pulled from the vacuum. Our results for baryon production are consistent with a variety of models, many of which are based on diquark production.

Further study of the hadronization process using the PEP-4 (Time Projection Chamber) detector awaits results on charged particle correlations, particularly strangeness and baryon correlations, neutral kaon and pion production, and strange baryon production. Study of all these processes, combined with those of other experiments at differing energies, should soon provide further insight into the hadronization process.

Appendix A—Electron Capture

Considerable care must be devoted to maintaining high purity gas in the TPC to prevent unacceptable amounts of capture of the drifting ionization electrons. Since we wish to measure the ionization with an accuracy of 2% or 3%, electron losses of more than 1% must be measured and corrected. Even if corrected, electron capture results in decreased statistical accuracy, since fewer electrons reach the sense wires than would without capture. In the extreme limit, so many electrons are lost that the signal falls below the electronic thresholds, and the ionization is not detected at all. Electron capture also leads to a decrease in the effective dynamic range of the signal processing system, since tracks close to the midplane suffer more capture than those close to the wires. As an example of the requirements on gas purity, we note that at 10 atmospheres of 80% argon 20% methane gas, 0.15 parts per million (ppm) of oxygen results in a 1% loss of electrons in a 1 meter drift for a drift field of 0.2 volts/cm torr [Hadley 78].

Extensive studies of electron capture and of the outgassing of electronegative impurities by different materials were conducted by the TPC experimental group. The studies were done to aid in the design of the TPC and *not* to study electron capture in general. All measurements were made, therefore, at 10 atmospheres, which was the expected TPC operating pressure.

For oxygen contamination in argon methane gas, electron capture was shown to be in quantitative agreement with a model in which electron capture proceeds through a two step, three

body process. First, the electron and the O_2 molecule collide to form an excited O_2^- ion, and second, this ion is then de-excited to the stable ground state by collision with a third molecule. For argon–methane gas, methane was shown to be the most important catalyst for the second step. For details of the experiments and the results, see Hadley 78.

In order to construct the TPC from those materials least likely to contaminate the gas, the outgassing properties of a large (> 100) number of substances commonly used in proportional chamber construction were studied. Since the purpose of the testing was to help build the TPC, all testing was done at 10 atmospheres in 80% argon 20% methane gas. For details of the experiments and a long list of the electronegative outgassing properties of various materials that we tested, see Brown 79.

References

Aihara 83a H. Aihara et al.,IEEE Trans. Nucl. Sci., *NS30*, 153 (1983).

Aihara 83b H. Aihara et al.,IEEE Trans. Nucl. Sci., *NS30*, 117 (1983).

Aihara 83c H. Aihara et al.,IEEE Trans. Nucl. Sci., *NS30*, 67 (1983).

Aihara 83d H. Aihara et al.,IEEE Trans. Nucl. Sci., *NS30*, 162 (1983).

Aihara 83e H. Aihara et al.,IEEE Trans. Nucl. Sci., *NS30*, 76 (1983).

Aihara 83f H. Aihara et al.,IEEE Trans. Nucl. Sci., *NS30*, 63 (1983).

Ali 80 A. Ali et al., Phys. Lett. *93B*, 155 (1980).

Althoff 82 M. Althoff et al., DESY–82–70 (1982).

Andersson 78 B. Andersson, G. Gustafson, and C. Peterson, Nucl. Phys. *B135*, 273 (1978).

Andersson 79 B. Andersson, G. Gustafson, and C.Peterson, Z. Physik *C1*, 105 (1979).

Andersson 80 B. Andersson, G. Gustafson, and T. Sjostrand, Z. Physik *C6*, 235 (1980).

Andersson 81 B. Andersson, G. Gustafson, and T. Sjostrand, LU–TP–81–3 (1981).

Appelquist 75 T. Appelquist and H.D. Politzer, Phys. Rev. *D12*, 1404 (1975).

Appelquist 78 T. Appelquist, R.M. Barnett, and K. Lane, Ann. Rev. Nucl. Part. Sci. 28. 387 (1978).

Atwood 82 W.B. Atwood et al., SLAC-PUB-2981 (1982).

Aubert 74 J.J. Aubert et al., Phys. Rev. Lett. 33, 1404 (1974).

Augustin 74 J.E. Augustin et al., Phys. Rev. Lett. 33, 1406 (1974).

Barber 79 D.P. Barber et al.,Phys. Rev. Lett. 43, 830 (1979).

Bartel 79 W. Bartel et al., Phys. Lett. 91*B*, 142 (1979).

Behrends 83 S. Behrends et al., Phys. Rev. Lett. 50, 881 (1983).

Berends 81 F.A. Berends and R. Kleiss, Nucl. Phys. *B*178, 141 (1981).

Berger 79 C. Berger et al., Phys. Lett. 86*B*, 418 (1979).

Berger 81 C. Berger et al., DESY-81-81 (1981).

Boehm 82 A. Boehm, Proceedings of the 1982 SLAC Summer Study, to be published.

Brandelik 79 R. Brandelik et al., Phys. Lett. 86*B*, 243 (1979).

Brandelik 81 R. Brandelik et al., Phys. Lett. 100*B*, 357 (1981).

Brandelik 82a R. Brandelik et al., DESY-82-13 (1982).

Brandelik 82b R. Brandelik et al., DESY-82-46 (1982).

Brown 79 F. Brown et al., TPC-LBL-79-8 (1979).

Casher 79 A. Casher, H. Neuberger, and S. Nussinov, Phys. Rev. *D*20, 179 (1979).

Casher 80 A. Casher, H. Neuberger, and S. Nussinov, Phys. Rev. *D*21, 1966 (1980).

Celmaster 79 W. Celmaster and R.J. Gonsalves, Phys. Rev. Lett. 44, 1404 (1979).

Chetyrkin 79 V.G. Chetyrkin et al., Phys. Lett. 85*B*, 277 (1979).

Dahl 79 O. Dahl, TPC-LBL-79-21 (1979).

Dine 79 M. Dine and J. Sapirstein, Phys. Rev. Lett. 43, 668 (1979).

Ellis 76 J. Ellis, M.K. Gaillard, and G.G. Ross, Nucl. Phys. *B*111, 253 (1976).

Fancher 79 D. Fancher et al., Nucl. Instr. Meth. 161, 383 (1979).

Felst 81 R. Felst, Proc. Int. Symposium on Lepton and Photon Interactions at high Energies, Bonn 1981.

Field 78 R.D. Field and R.P. Feynmann, Nucl. Phys. *B*136, 1 (1978).

Furmanski 79 W. Furmanski, R. Petronzio, and S. Pokorski, Nucl. Phys. *B*155, 253 (1979).

Galtieri 82 L.G.Galtieri, SLAC–PUB–250 (1982).

Goldhaber 76 G. Goldhaber et al., Phys. Rev. Lett. 37, 255 (1976).

Hadley 78 N.J.Hadley, TPC–LBL–78–42 (1978).

Hadley 82 N.J.Hadley, TPC–LBL–82–60 (1982).

Hanson 75 G.G. Hanson et al., Phys. Rev. Lett. 35, 1609 (1975).

Hargrove 82 C.K.Hargrove, SLAC–PUB–250 (1982).

Hilke 78 H.J.Hilke, TPC–LBL–78–50 (1978).

Hofmann 81 W. Hofmann, Z. Physik, *C*10, 351 (1981).

Hofmann 83 W. Hofmann, Private Communication (1983).

Hoyer 79 P. Hoyer et al., Nucl. Phys. *B*161, 349 (1979).

Ilgenfritz 78 E.M.Ilgenfritz, J.Kripfganz, and A.Schiller, Acta Phys. Pol. *B*9, 881 (1978).

Jackson 75 J.D. Jackson and D.L. Scharre, Nucl. Instr. Meth. 128, 13 (1975).

Jersak 81 J. Jersak et al., Phys. Lett. 98*B*, 363 (1981).

Komamiya 82 S. Komamiya, Tokyo U. UTLICEPP–82–01 (1982).

Landau 44 L. Landau, J. Phys. USSR 8, 201 (1944).

Lynch 81 G.R. Lynch, TPC-LBL-81-6 (1981).

Lynch 82 G.R. Lynch and N.J. Hadley, SLAC-PUB-250 (1982).

Madaras 83 R. Madaras, Private Communication (1983).

Marx 82 J.N. Marx et al., TPC-SLC-82-2 (1982).

Meyer 81 T. Meyer, Z. Physik *C12*, 77 (1981).

Nelson 83 M.E. Nelson et al., SLAC-PUB-3059 (1983).

Patrick 82 J.F. Patrick et al., Phys. Rev. Lett. 49, 1232 (1982).

Polyakov 75 A.M. Polyakov, Proc. 7^{th} Int. Symposium on Lepton and Photon Interactions at High Energies, Stanford 1975.

Ranft 80 J. Ranft and S. Ritter, Acta. Phys. Pol. *B11*, 259 (1980).

Ronan 82 M. Ronan, J. Maillaud, and T. McGathen, IEEE Trans. Nucl. Sci. *NS29* , 427 (1982).

Salam 68 A. Salam, in *ElementaryParticlePhysics*, edited by N. Svartholm, (Almquist and Wiksell, Stockholm, 1968) p. 367.

Sjostrand 82 T. Sjostrand, LU-TP-82-3 and LU-TP-82-7 (1982).

Sternheimer 71 R.M. Sternheimer and R.F. Peierls, Phys. Rev. *B3*, 3681 (1971).

Talman 79 R. Talman, Nucl. Instr. Meth. 159, 189 (1979).

Walenta 81 A.H. Walenta, Physica Scripta 23, 354 (1981).

Weinberg 67 S. Weinberg, Phys. Rev. Lett. 19, 1264 (1967).

Wiik 80 B.H. Wiik, DESY-80-124 (1980).

Wolf 81 G. Wolf, DESY-81-86 (1981).

Wolf 82 G. Wolf, DESY–82–77 (1982).

Wolf 83 G. Wolf, Private Communication (1983).

Yelton 82 Y.M. Yelton et al., SLAC–PUB–2926 (1982).

TECHNICAL INFORMATION DEPARTMENT
LAWRENCE BERKELEY LABORATORY
UNIVERSITY OF CALIFORNIA
BERKELEY, CALIFORNIA 94720